Investigating the Speed of Sound of the Medium Formed by Heavy-Ion Collisions at the LHC

by
Negin Alizadehvandchali

A dissertation submitted to the Department of Physics,
College of Natural Sciences and Mathematics
in partial fulfillment of the requirements for the degree of

Doctor of Philosophy
in Physics

Committee Chair: Anthony R. Timmins
Committee Member: Amin Alipour
Committee Member: Daniel Cherdack
Committee Member: Greg Morrison
Committee Member: Claudia Ratti

University of Houston
May 2023

DEDICATION/EPIGRAPH

To my beloved parents, whose kindness is known to all who have met them. To my intelligent and charming little sister, from whom I have learned so much, even though I'm the eldest. And finally, to our first dog, Lexi, for whom I will forever be grateful for the love and joy she brought to our family.

ACKNOWLEDGMENTS

Completing a Ph.D. dissertation is a journey that is not accomplished alone but with the support and encouragement of many individuals. I am deeply grateful to everyone who contributed to the successful completion of my dissertation. First and foremost, I would like to express my heartfelt gratitude to my advisor, Anthony R. Timmins, for his guidance, support, and invaluable advice throughout my Ph.D. studies. Without his expertise, encouragement, and unwavering commitment, this dissertation would not have been possible. I would like to convey my genuine thanks to Rene Bellwied for his insightful comments in every group meeting. His patience and enthusiasm have been a constant source of inspiration for all of us. I would like to express my sincere gratitude to my committee members, Amin Alipour, Daniel Cherdack, Greg Morrison, and Claudia Ratti, for their insightful feedback and suggestions, which helped shape and improve this work. I would also like to thank my friends, all the great people I've met during my Ph.D., and our group study members, Jonathan, Carlos, and Osas during the first two years of this journey. A special thank you goes out to all my Persian friends in Houston for their kindness and warmth, and for bringing a piece of home to me. Furthermore, I want to express my heartfelt appreciation to my family who has supported me every step of the way on this long and challenging journey. Your unwavering love, encouragement, and belief in me have been the bedrock of my success. I could not have reached this milestone without your constant support and sacrifice.

Thank you all for being my constant pillars of strength and inspiration.

ABSTRACT

The Quark-Gluon Plasma (QGP) is a phase of matter that is believed to be created shortly after the Big Bang, an extremely hot and dense matter where quarks and gluons become deconfined from their typical hadronic states. A Large Ion Collider Experiment (ALICE) at the Large Hadron Collider (LHC) and the experiments at the Relativistic Heavy Ion Collider (RHIC) have obtained experimental evidence of QGP formation generated through relativistic heavy ion collisions with ultra-relativistic energies. They have provided a tool to study the phase transition from hadronic matter to this deconfined phase of quarks and gluons. This dissertation results from studies at the Large Hadron Collider in Geneva, Switzerland, in which nuclei collide to study matter under the most extreme conditions on earth. It's been a big open challenge to obtain an experimental determination of the temperature reached in a heavy-ion collision and also the determination of other thermodynamic quantities, such as the entropy, which gives access to the number of degrees of freedom. Recent endeavors in determining the temperature of the medium formed in heavy-ion collisions made it possible to empirically measure other thermodynamic quantities, such as the speed of sound. The speed of sound is a fundamental property of any material. It is directly related to the thermodynamic properties of the QGP and the hot hadronic matter produced by the QGP after the phase transition. It also plays a fundamental role in exploring the equation of state (EOS). This dissertation uses the data from heavy-ion collisions from the ALICE detector, in Pb-Pb collisions at $\sqrt{s_{NN}} = 5.02$ TeV and Xe-Xe collisions at $\sqrt{s_{NN}} = 5.44$ TeV. Two methods were explored to extract the speed of sound experimentally in ultra-central collisions. i.e., the two nuclei collide head-on. The values obtained are consistent with predictions from Lattice QCD at temperatures of around $T = 150$ MeV.

TABLE OF CONTENTS

LIST OF TABLES

LIST OF FIGURES

1 Introduction

The Quark Gluon Plasma (QGP) is a state of matter in which the quarks and gluons, which are the elementary particles and building blocks of matter, become deconfined. The temperatures required for this transition are approximately 4 trillion kelvin. It is believed that the universe existed in such a state shortly after the big bang. But what exactly happens to strongly interacting matter in the limit of high temperatures and densities like those of the quark-gluon plasma? This question has fascinated physicists ever since the discovery of the strong force and the multiple hadron production it leads to. The next chapters are based on some of the properties of QGP that are understood either by theoretical or experimental studies.

The standard model (SM), quantum chromodynamics (QCD), lattice quantum chromodynamics (LQCD), and multiplicity sensitivity to initial states will be reviewed in this chapter. In section 1.1, the standard model will be discussed, which is a theory that can address many questions regarding subatomic scales that physicists could not address before. It can describe the interactions between elementary particles. All ordinary matter in today's universe is made up of atoms. Each atom contains a nucleus composed of protons and neutrons surrounded by a cloud of electrons. Protons and neutrons are, in turn, made of quarks bound together by other particles called gluons. Subsequently, quantum chromodynamics (QCD) will be explained in section 1.2. It is the most successful theory of strong interactions between elementary particles. Quarks interact via the strong nuclear force, and the strong force is mediated by gluons. In section 1.3, Lattice QCD will be addressed, which is a well-established non-perturbative approach to solving the quantum chromodynamics (QCD) theory of quarks and gluons. In section 1.4, the QGP and its properties will be explained in detail. In the end, in section 1.5 the equation of state in QGP will be explained, followed by the predictions of LQCD for the speed of sound.

1.1 The Standard Model

Generally, the interactions between elementary particles can be described by four forces: Gravitational, Electromagnetic, Weak, and Strong [1]. The last three belong to a relativistic quantum field theory which is called the Standard Model (SM). The standard model is the best theory of elementary particles so far, and it aims at describing all the phenomena of particle physics except those due to gravity. It elaborates on the properties and interactions of fundamental particles, which are now defined as being point-like, without internal structure or excited states.

	1^{st} Generation		**2^{nd} Generation**		**3^{rd} Generation**	
Quarks	**up (u)**	**down (d)**	**strange (s)**	**charm (c)**	**bottom (b)**	**top (t)**
Mass (GeV/c^2)	0.0018−0.003	0.0045−0.0053	0.09−0.1	1.275±0.025	4.18±0.03	173.21±0.51±0.71
Charge (e)	$+2/3$	$-1/3$	$-1/3$	$+2/3$	$-1/3$	$+2/3$
Weak Isospin	$+1/2$	$-1/2$	$-1/2$	$+1/2$	$-1/2$	$+1/2$
I_3	$+1/2$	$-1/2$	0	0	0	0
S	0	0	-1	0	0	0
C	0	0	0	+1	0	0
B	0	0	0	0	-1	0
T	0	0	0	0	0	+1
Leptons	**electron (e) electron neutrino (ν_e)**		**muon (μ) muon neutrino (ν_μ)**		**tau (τ) tau neutrino (ν_τ)**	

Figure 1: The fundamental characteristics of quarks including their mass, electrical charge, weak isospin, the third element of the isospin (I_3), as well as strangeness (S), charm (C), bottom (B), and top (T) properties [3].

An elementary particle can be characterized by its mass, electric charge, and spin. There are seventeen known elementary particles in the standard model, as one can see in Figure 2. These particles are either the building blocks of matter, called fermions or the mediators of interactions, called bosons. There are twelve named fermions with spin half and five named bosons, which include four gauge bosons with non-zero integer spin (the force carriers) and one Higgs boson with spin zero. There are three generations of fermions, and the mass of each generation is different. Each generation contains two quarks and two leptons. So there are also six types of quarks, shown in Figure 1 and six types of leptons (electron, muon, tau, and their corresponding neutrinos) [2]. In this context, spin is an angular momentum possessed by all particles in quantum theory, even

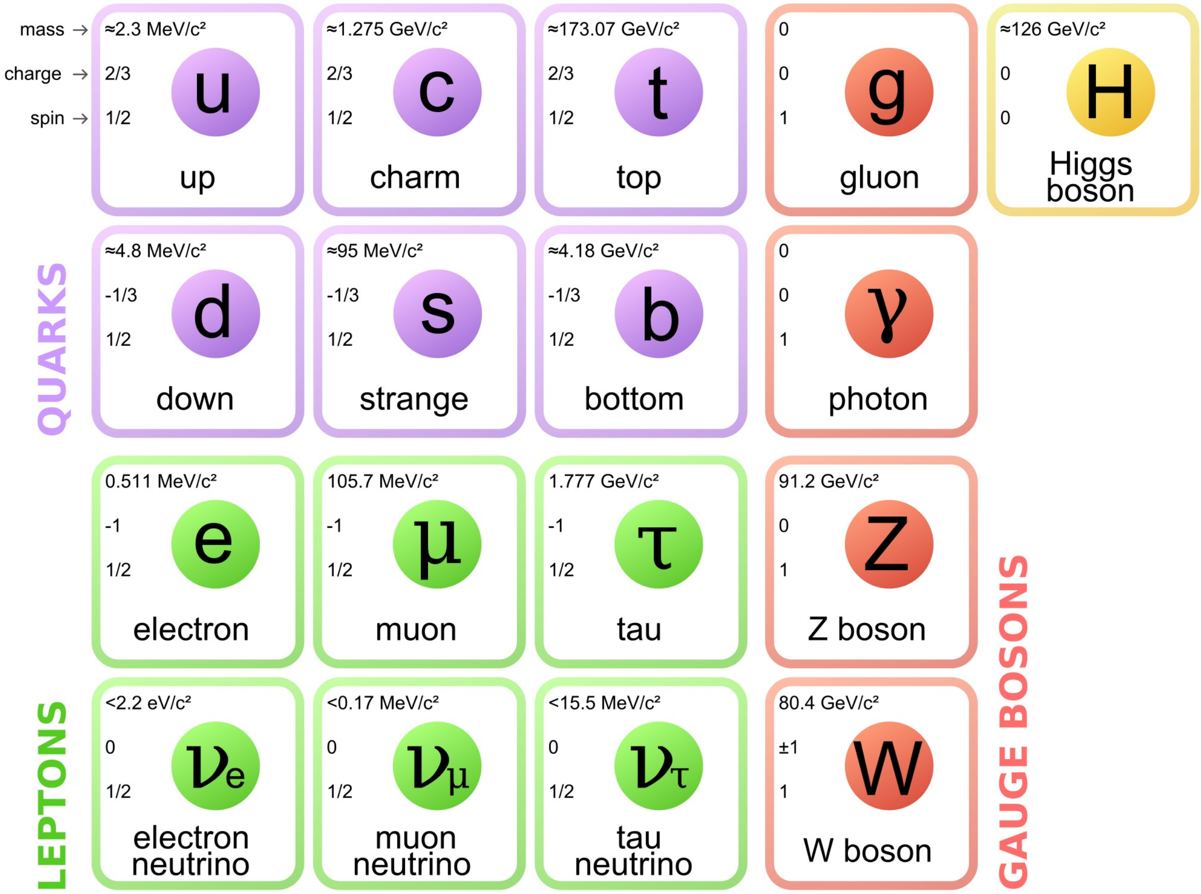

Figure 2: Schematic view of the elementary particles in the Standard Model [4].

when they are at rest. Spin has no classical analog and is different from the use of the same word in classical physics, where it usually refers to angular momentum about its own axis. In classical physics, electromagnetic interaction is propagated by electromagnetic waves, which are continuously emitted and absorbed. While this is accurate for large distances, at short distances, one needs to consider the quantum nature of the interaction. In quantum theory, the interaction is transmitted by the exchange of photons, which are members of the family of fundamental spin-1 bosons of the standard model. Photons are referred to as the gauge bosons, or 'force carriers', of the electromagnetic interaction. The exchange of spin-1 gauge bosons also mediates the weak and strong interactions. For the weak interaction, these are the W^+, W^-, Z^0 bosons (superscripts just show the electric charges) with masses about 80–90 times the mass of the proton. For strong interaction, the force carriers are called gluons. There are eight gluons, all of which have zero mass and are electrically neutral.

Hadrons refer to the composite particles formed by quarks, with nucleons being one example. However, there exist several hundred other types of hadrons, excluding nuclei, most of which are not stable and decay due to one of three interactions. A large number of hadrons led to the development of a simplified theory known as the quark model in the 1960s to explain their existence. The pion is a commonly unstable hadron, with three electrical charge states denoted as $\left(\pi^+, \pi^0, \pi^-\right)$. Hadrons are significant as free quarks are not observed in nature, and thus their properties are inferred from the study of hadrons. This is analogous to deducing the properties of nucleons by exclusively examining nuclei. While nucleons are bound states of quarks and nuclei are bound states of nucleons, the standard model should, in theory, explain the properties of nuclei from those of quarks and their interactions. However, this is not currently possible due to limitations in calculation techniques, resulting in nuclear and particle physics being treated as almost separate subjects. Nevertheless, both fields are related, and introductory approaches benefit from presenting them together.

The strong force in the standard model can be described by Quantum Chromodynamics, which will be addressed in the next section.

1.2 Quantum Chromodynamics (QCD)

The mathematical model used to describe the interaction between colored charges (quarks) through the exchange of gluons is known as Quantum Chromodynamics (QCD) [31]. It is the most successful theory that describes the strong interaction between quarks and gluons. The strong interaction is responsible for the existence of atomic nuclei, so about 95 percent of the visible mass of the Universe. The color charge, unlike the electric one, can have three values called red, green, and blue conventionally. Each quark can have one color charge, while gluons can have two, a color and an anti-color charge. This fact is related to the most unique feature of QCD compared to other fundamental forces; it is called $anti-screening$ and states that gluons can self-interact, which will be explained later.

Quarks come in three different colors: red, green, and blue, and anti-quarks come in three corresponding anti-color charges: anti-red, anti-green, and anti-blue. The combination of quarks can result in color-neutral particles. For instance, a combination of red, blue, and green quarks can be color-neutral charges, just as a combination of anti-red, anti-blue, and anti-green quarks can be color neutral for anti-charges. Similarly, the combination of opposite charges, such as green and anti-green quarks, can also be color neutral. These combinations can form hadrons, which can be either baryons with three quarks or anti-baryons with three anti-quarks, or mesons with a quark and an anti-quark.

1.2.1 Screening and Anti-Screening in QCD

In the context of quantum field theory, the interactions among particles are determined by the combined effects of all conceivable processes that can take place. To be specific, when considering the interaction between two quarks in a vacuum, even with the basic exchange of a single gluon taken into account, it is necessary to take into account additional processes where the exchanged gluon can interact with short-lived particles. A possible scenario is that the exchanged gluon generates a pair of a quark and an anti-quark (see Figure 3). Screening is the term used to describe the reduction in interaction strength between a pair of oppositely charged quarks due to the masking of their charges. This effect is referred to as screening because it decreases the effective charge of the quarks. Within the framework of QCD, it is possible for other processes to occur in which a pair of gluons is created (see Figure 4). These gluons have an attractive force on each other, resulting in an increase in interaction strength between quarks. This particular mechanism is referred to as anti-screening, and it is considered the primary mechanism within QCD.

1.2.2 Coupling Constant in QCD

According to the uncertainty principle, the strength of the processes in QCD relies on the momentum exchanged Q^2 between two quarks, which is in inverse proportion to the spatial distance where the interaction occurs. Therefore, the total interaction strength between two quarks, which

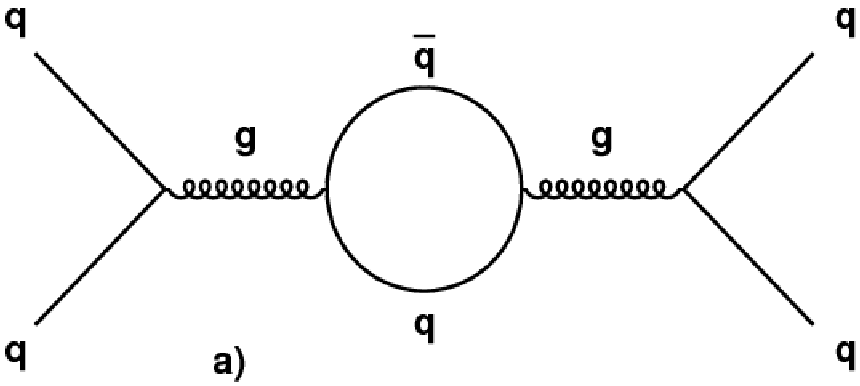

Figure 3: Feynman diagram of QCD interactions representing screening

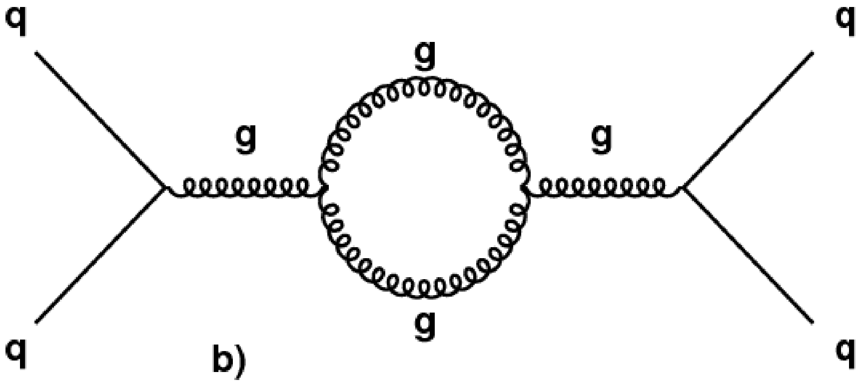

Figure 4: Feynman diagram of QCD interactions representing anti-screening

is measured in terms of the strong coupling constant α_s, follows the behavior as described in Figure 5. To understand the behavior of two quarks and the interaction between them, one can check the strong potential between them:

$$V(r) = -\frac{4}{3}\frac{\alpha_s}{r} + \kappa r, \tag{1}$$

where r is the distance between the quarks, and κ is a constant that is equivalent to the constant in the string tension equation. As momentum transfers become larger (i.e., as distances become smaller), anti-screening becomes less significant, and the strong coupling constant (α_s) decreases to a point where partons can exist as quasi-free particles. This phenomenon is known as asymptotic freedom. On the other hand, at low momentum transfers (i.e., for large distances

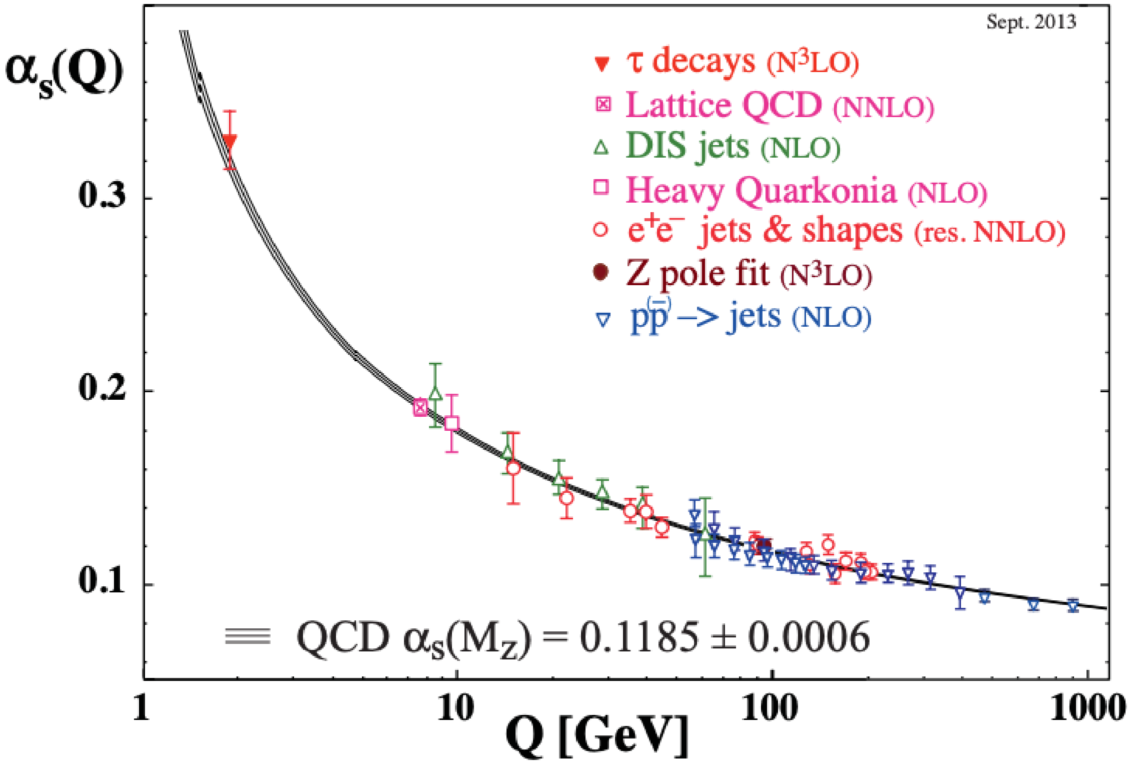

Figure 5: Measurements summary of the QCD coupling constant along with QCD predictions (bands) as a function of Q (energy scale) [85] .

between interacting quarks), anti-screening becomes dominant, and the strong coupling constant (α_s) diverges. The overall result can be effectively summarized as follows: when a quark and anti-quark pair are separated, the binding energy between them increases as the distance between the quarks increases. Eventually, the binding energy becomes so strong that it becomes energetically favorable to create another quark and anti-quark pair from the vacuum and split the original pair into two separate pairs. This behavior is commonly known as color confinement, which means that quarks are limited to forming colorless bound states, such as hadrons. These two distinct properties, namely asymptotic freedom and color confinement, are specific to QCD and define its dynamics. Although high-energy interactions in QCD are easily comprehended and can be computed via perturbation theory, low-energy interactions that involve ($\alpha_s > 1$) cannot be computed this way. Therefore, it is necessary to use effective theories and/or numerical methods, such as non-perturbative calculations in a discretized spacetime (Lattice QCD). The aforementioned approach, specifically non-perturbative calculations in a discretized spacetime, has proven to be highly beneficial for examining static QCD systems, as it will be discussed later. However, it encounters significant obstacles when it comes to forecasting the characteristics of dynamic QCD systems, which are more applicable in describing natural occurrences [32].

1.3 Lattice QCD

The equation of state of Quantum Chromodynamics (QCD) at finite temperatures and baryon densities has a broad range of applications in modern particle and nuclear physics, including the study of heavy ion collisions, the expansion of the early universe, and the interiors of compact stars. However, on most relevant scales, QCD is strongly coupled and cannot be studied through perturbative methods. In recent years, Lattice Quantum Chromodynamics (LQCD), a non-perturbative method for predicting the thermodynamic characteristics of hadronic matter through numerical simulations of the interactions between quarks and gluons, has been established. It is a lattice gauge theory, and the basic idea behind LQCD is to discretize space-time into a lattice of discrete points and to use numerical methods to solve the QCD equations on this lattice. This allows us to study the properties of QCD in a controlled and systematic way, without relying on perturbative approximations. Basically, it is a numerical technique to solve this theory:

$$\mathcal{L}_{QCD} = -\frac{1}{4}F^{a}_{\mu\nu}F^{a,\mu\nu} + \sum_{q=u,d,s,c} \bar{\psi}_q \left[i\gamma^{\mu}D_{\mu} - m_q\right]\psi_q \tag{2}$$

where $F^{a}_{\mu\nu}$ is the QCD gluon field strength tensor, ψ represents the quark field, D_{μ} is the gauge covariant derivative, m is the mass of the quarks, and γ^{μ} are the Dirac matrices.

Where F and D are defined as:

$$\begin{aligned} F^{a}_{\mu\nu} &= \partial_{\mu}A^{a}_{\nu} - \partial_{\nu}A^{a}_{\mu} + gf^{abc}A^{b}_{\mu}A^{c}_{\nu}, \\ D_{\mu}\psi &= \left(\partial_{\mu} - igT^{a}A^{a}_{\mu}\right)\psi. \end{aligned} \tag{3}$$

The gauge field dynamics can be described as follows:

$$-\frac{1}{4}F^a_{\mu\nu}F^{a,\mu\nu} = -\frac{1}{4}\left(\partial_\mu A^a_\nu - \partial_\nu A^a_\mu\right)\left(\partial_\mu A^a_\nu - \partial_\nu A^a_\mu\right) - g f^{abc}\partial_\mu A^a_\nu A^{b,\mu}A^{c,\nu} - \frac{g^2}{4} f^{abc} f^{ade} A^b_\mu A^c_\nu A^{d,\mu} A^{e,\nu} \tag{4}$$

and g is the coupling constant. In statistical mechanics, it is widely recognized that knowing a system's partition function allows for the theoretical calculation of all thermodynamic properties. QFT can be defined by a Hamiltonian $\hat{H}$ with eigenvalues E_i. At a temperature T, the partition function is:

$$Z = \sum_i e^{-E_i/T} = \mathrm{Tr}\, e^{-\hat{H}/T} \tag{5}$$

where the trace means one needs to integrate on some basis, e.g., position.

$$\begin{gathered} Z = \int d\phi^{(0)} \left\langle \phi^{(0)} \left| e^{-\hat{H}/T} \right| \phi^{(0)} \right\rangle \\ Z \sim \int D \prod_j e^{-\delta\tau \sum_i \left[\left(\frac{d\phi()^{()}}{\delta\tau} \right)^2 + V\left(\phi^{(j)}\right) \right]} = \int D\phi e^{-\int_0^{1/T} \mathcal{L}_E(\phi)} \end{gathered} \tag{6}$$

The partition function Z describes the probability of all possible configurations of quark and gluon fields on the lattice. Therefore, a quantum system at finite temperature is inherently a Euclidean system with periodic or antiperiodic boundaries for bosonic or fermionic fields, respectively.

Lattice QCD is utilized when the Lagrangian is discretized on a space-time lattice with dimensions of $N_\tau \times N_\sigma^3$ and lattice spacings of a_τ and a_σ, with $a_\tau = a_\sigma = a$ often being used for calculations. Other important variables include the volume, which is represented by V and equals L^3, where $L = N_\sigma a_\sigma$. For finite temperature calculations, β is generally selected to be less than L, where $\beta = N_\tau a_\tau$. The thermodynamic properties are determined by taking appropriate derivatives of the partition function. The lattice representation of QCD involves quark fields located on lattice sites and gluon fields defined as links connecting adjacent sites. As the lattice becomes fine and the sites become infinitesimally close, the continuum QCD is obtained. The issue with lattice QCD arises when the chemical potential is non-zero, resulting in an imbalance between quarks and anti-quarks, which breaks charge-conjugation symmetry and leads to a complex determinant that differs from its real counterpart. This is known as the “sign problem”, limiting lattice QCD calculations to high temperature and small baryon chemical potential. In this range, the partition function can be expanded as a Taylor series in μ_B/T, with the coefficients being the generalized susceptibilities.

Figure 6 is an illustration of a grid-like pattern of connecting points that has its sites spaced out periodically. In a 2D or 3D lattice, each site can only communicate with its neighboring sites through a link or line segment connecting them. This means that a single site can interact with a maximum of four neighboring sites in a 2D lattice (as shown in Figure 6) or six neighboring sites in a 3D lattice. However, there are limitations to calculations using a lattice due to various factors. Three main factors limit the use of lattice simulations. Firstly, as the number of sites and links between them increases in the simulation, the processing power required to simulate the interactions also increases. Secondly, the complexity of the interactions between the lattice sites requires more processing power to calculate and simulate the potential effects on the lattice. For example, using an Ising model to demonstrate the interactions between sites is far less complex than using quantum field theory, which requires more computational resources [69]. Thirdly, while lattice simulations can accurately describe a system in thermodynamic equilibrium, they are not well-suited for modeling dynamic processes. Therefore, lattice simulations may not be appropriate for studying systems that involve dynamic changes over time. However, despite these limitations, lattices are relatively easy to construct and simulate using modern computer systems. The use of lattices in simulating QCD relies on the incorporation of quarks and gluons into the sites and links of the lattice. By constructing a lattice where each site corresponds to a quark and each link represents a gluon, one can create a simulation that is similar to the physical representation of quarks and gluons in particles or a Quark-Gluon Plasma (QGP). Due to the nature of the lattice, the distance between the quarks (sites) is kept constant and determined by the length of the links between them. However, the strength of the links can be adjusted to approximate the effect that gluons would have on quarks, which allows for more accurate simulations. Additionally, the lattice can be constructed in such a way that the temporal dimension corresponds to a temperature dimension.

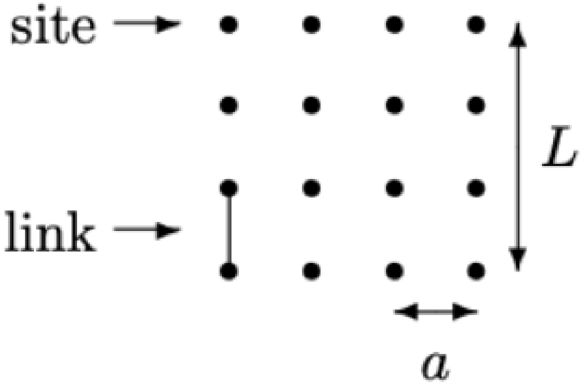

Figure 6: Lattice approximation [68].

1.4 Creating QGP Using Heavy Ion Collisions

Based on the phenomenon of asymptotic freedom mentioned before, it was expected by many theorists that a new state of nuclear matter containing deconfined quarks and gluons, if it could somehow be managed to be produced in the laboratory at high temperatures and energy densities, should demonstrate properties similar to a weakly interacting gas. Edward Shuryak first realized in 1978 that the thermal fluctuations of gauge fields might produce a dominant effect over vacuum fluctuations, which would translate into dominant screening over anti-screening of color fields [51, 52]. For this reason, he coined the term quark-gluon plasma for a state of matter consisting of deconfined quarks and gluons. Also, Hagedorn had already anticipated a temperature limit for hadronic matter ($T \simeq 170\text{MeV}$) using a statistical bootstrap model before the discovery of QCD and its properties, such as asymptotic freedom [33]. Additionally, the discovery of asymptotic freedom in QCD indicated the emergence of a new phase of weakly interacting quarks and gluons at high temperatures, known as the QGP [34]. As illustrated in Figure 7, QCD research and the statistical hadronization model have already identified two separate regimes, namely the quark-gluon plasma and hadronic matter. QCD is not the only way that one can prove the existence of QGP. The results from heavy-ion collision experiments have revealed various data and occurrences that provide evidence for the formation of QGP during these experiments. Several phenomena were observed in heavy-ion collision experiments that support the existence of QGP, including the suppression of J/ψ [36], increased production of strange hadrons compared to pp collisions [37], significant suppression of high-energy jets and heavy quarks [38], and a large azimuthal asymmetry in particle yields or elliptic flow, denoted by v_2 [39]. The surprising aspect of these experimental measurements was that, if the QGP consisted of weakly interacting quarks and gluons, then why did it display fluid dynamic behavior (as observed in the v_2 measurements) and jet quenching (as evidenced by the strong suppression of high-energy jets)? The experiments discovered that the QGP was, in fact, a strongly interacting fluid [40, 41, 42].

Also, another question was what is the transition temperature from a hadronic to a deconfined state, and if this temperature can be achieved in the laboratory? Calculations on lattice QCD predict the phase transition to occur at about $T_c \simeq 175$ MeV (which is a temperature when the transition to partonic degrees of freedom occurs, and the medium becomes the QGP), and this temperature is reached in heavy-ion collisions currently delivered both at RHIC and LHC. Since such a deconfined state of matter is believed to have existed a few microseconds after the Big Bang, by producing QGP in heavy-ion collisions, the same conditions which existed in the early universe are being created. By doing this, the current understanding of its origin and evolution can be enhanced. For completeness, other possible phases of nuclear matter, besides the QGP, are presented in Figure 7, and the region explored with heavy-ion collisions at the LHC is indicated. The baryon chemical potential indicates the difference in the number of baryons and antibaryons. For instance, $\mu_B > 0$ shows that the amount of baryon is more than anti-baryon. The line shows the pseudo-critical temperature, and the band represents the half-width of the crossover transition (the temperatures where a QGP and hadrons can co-exist) that is accessible to Lattice QCD calculations [53]. The open points demonstrate experimental observations to determine the chemical freeze-out

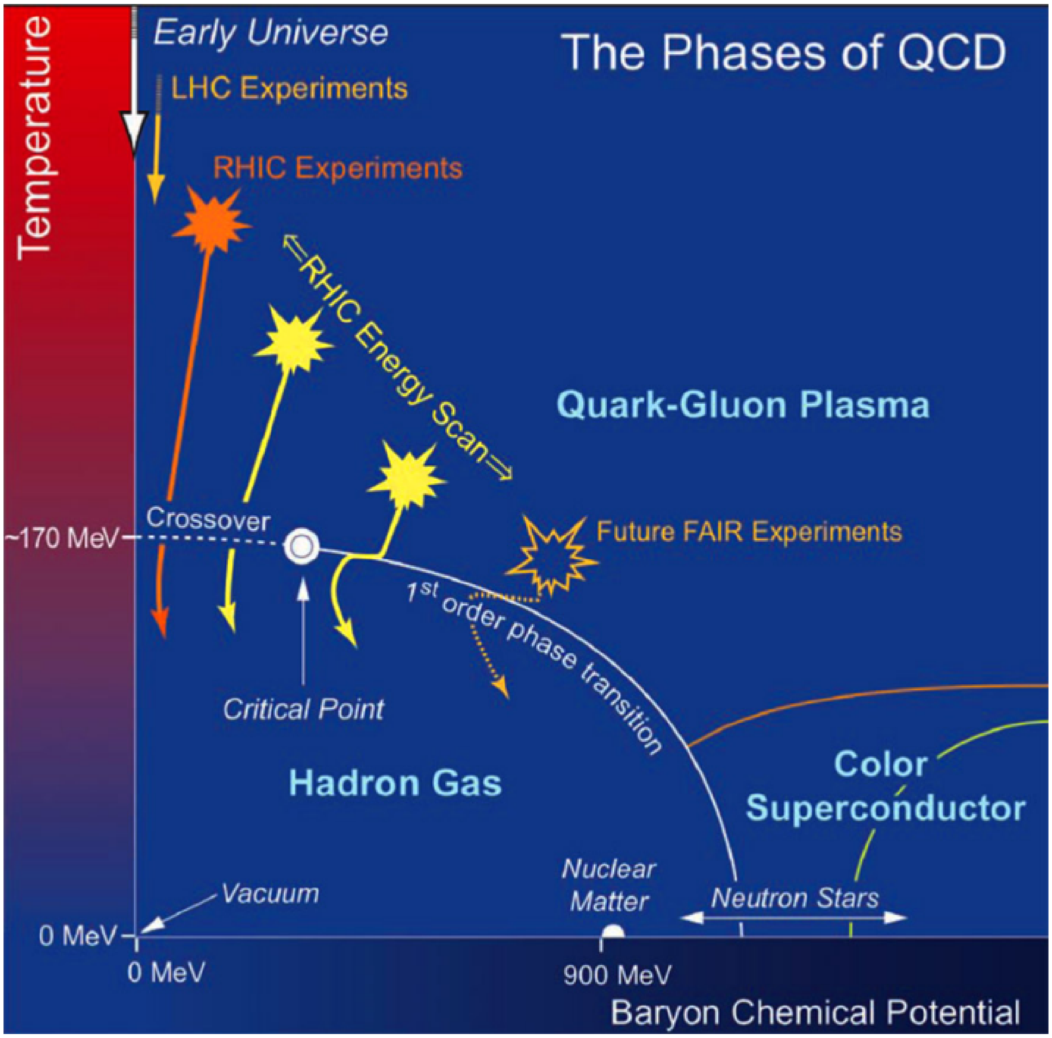

Figure 7: Representation of the QCD phase diagram [35]

parameters [54, 55].

After the collision, the pre-equilibrium stage forms before one fm/c in which quarks and gluons exist in a quasi-free deconfined state. Quarks, which are always confined into hadrons, are now free to interact with other quarks and gluons in this deconfined matter. The equilibrium stage between quarks and gluons happens around one fm/c, as one can see in Figure 8. The QGP system continues to expand and cool down through elastic and inelastic collisions during the expansion stage from ($1 < \tau < 10$fm/c). As the QGP expands and cools down, it reaches a critical temperature T_c. This

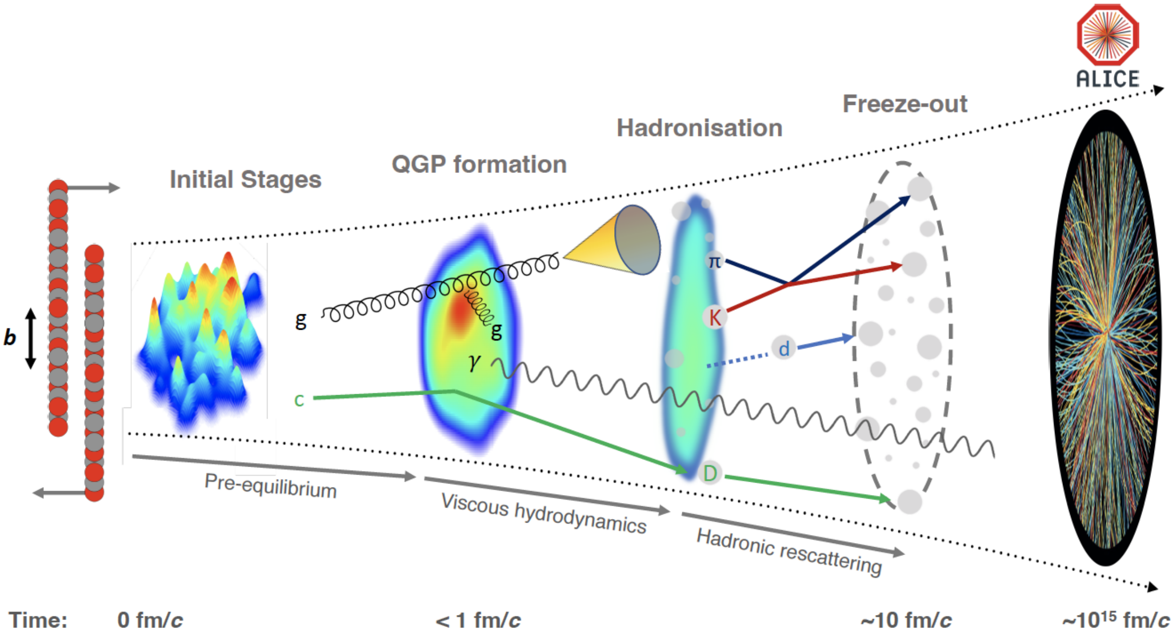

Figure 8: Heavy-ion collision stages at the Large Hadron Collider (LHC). Figure is taken from [43]

is when the hadronization happens, and quarks and gluons start to form hadrons. The chemical freeze-out temperature $T_{ch} \approx 155$MeV occurs during the mixed-phase or cross-over phase when the number of hadrons is fixed, inelastic collisions cease and relative particle abundances do not change [56]. After chemical freeze-out, elastic collisions continue to occur, and the particle's momentum can change but will not produce any new particles. At kinetic freeze-out, $T \approx 120$MeV, around 15 fm/c, elastic collisions cease, and the system reaches a point where the kinematic distributions of hadron species have been fixed. At this stage, the detectors will measure the particles.

1.5 The QCD Equation of State (EOS) in the QGP

The equation of state (EOS) in Quark-Gluon Plasma is one of the fundamental properties of quantum chromodynamics (QCD) which establishes how the pressure of a system depends on factors such as energy, baryon density, temperature, and chemical potential. Specifically, the pressure can be expressed as a function of energy and baryon density, denoted as $P = P(\mathcal{E}, n_B)$, or as a function of temperature and chemical potential, denoted as $P = P(T, \mu)$. This is because, in a state of thermodynamic equilibrium, the total electric charge must be zero and strangeness is not conserved. To determine the expansion of hot dense matter, the speed of sound, represented by c_s^2, can be defined as:

$$c_s^2 = \left.\frac{\partial P}{\partial \mathcal{E}}\right|_{s/n_B} . \tag{7}$$

The derivative of the pressure with respect to the energy is taken at a constant entropy per baryon. The EOS provides a helpful representation of how pressure gradients arise from gradients in the energy density profile. The speed of sound is also informative about the various regimes in the QCD phase diagram. In the regime of high temperatures, where the temperature greatly exceeds the critical temperature ($T \gg T_c$), the EOS is characterized by the relationship $\mathcal{E} = 3P$. As a result, according to Equation (7), the speed of sound is equal to $c_s^2 = 1/3$. The speed of sound also equals 1/3 in the case of low temperature and zero baryon density, where the pressure is dominated by weakly interacting, massless pions. As the QCD phase is approached from low and high temperatures, the behavior of the speed of sound follows a pattern of initially increasing towards its maximum value $c_s^2 = 1/3$. As the crossover temperature is approached, the compressibility of the matter is high, and the speed of sound reaches a minimum for the low temperature and zero baryon density regime. However, at high temperatures, the speed of sound increases towards the perturbative value of 1/3, indicating that a system initially produced with an energy density far exceeding the critical density will accelerate rapidly and then transition smoothly through the phase (see Figure 9).

1.6 Lattice QCD Predictions for Speed of Sound

The lattice spacing, denoted by a, is used to discretize the hypercubic lattice with a fixed number of points in the temporal and spatial directions. By adjusting the lattice spacing, the temperature can be set. This adjustment requires changing the bare parameters of the lattice action. Conversely, to investigate the effects of lattice discretization at a fixed temperature, the value of N_t can be varied:

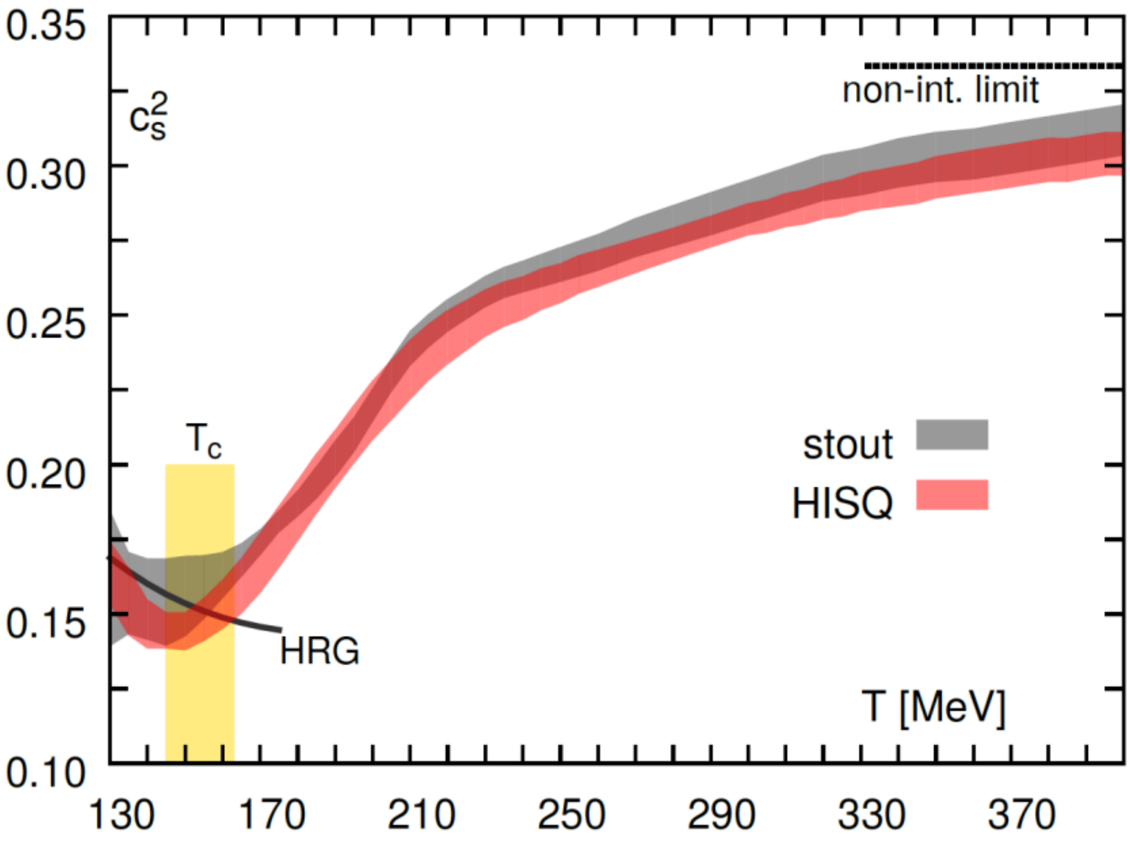

Figure 9: This plot represents a comparison of the speed of sound squared obtained from lattice QCD simulations (using HISQ and stout methods) and the Hadron Resonance Gas (HRG) model as a function of temperature. The crossover region, which occurs at a temperature of approximately 154 ± 9MeV, is marked by a vertical band on the plot. The horizontal line in the upper right corner represents the ideal gas limit. The Figure is taken from [86].

$$T = \frac{1}{N_t a}, \quad V = (N_s a)^3 \, . \tag{8}$$

The change in lattice spacing affects the discretization of spacetime and can affect the accuracy of the calculations. Therefore, changing N_t can affect the prediction of the speed of sound values.

As mentioned in the previous section, by calculating the pressure and energy density of the system one can calculate the speed of sound:

$$c_s^2 = \frac{\partial P}{\partial \epsilon}, \tag{9}$$

where P is the pressure and ϵ is the energy density. As the temperature increases, the thermodynamic quantities approach the values of the non-interacting massless relativistic gas, which is known as the Stefan-Boltzmann limit.

In lattice Quantum Chromodynamics, the pressure and energy density can be obtained by calculating the trace anomaly:

$$\theta^{\mu}_{\mu} = \epsilon - 3P = -a^4 \frac{\partial \log Z}{\partial a}, \tag{10}$$

where Z is the partition function, and a is the lattice spacing. By taking the derivative of $\log Z$ with respect to a and multiplying by $-a^4$, the trace anomaly can be computed. From the trace anomaly, the pressure and energy density can be calculated as:

$$P = \frac{1}{3}\theta^{\mu}_{\mu} - \frac{\epsilon}{3}. \tag{11}$$

By using the equation for the speed of sound and the expressions for the pressure and energy density obtained from the trace anomaly, the speed of sound can be computed.

Figure 10 presents results for the QCD pressure with $N_f = 2 + 1$ flavor dynamical quarks as a function of the temperature. This result is from three different lattice spacing. The temperature range for $N_t = 6$ and 8 is from 100 to 1000 MeV. But for $N_t = 10$, the range is from 100 up to 365 MeV. As the temperature increases, the thermodynamic properties tend to resemble those of a non-interacting, massless relativistic gas, which is known as the Stefan-Boltzmann limit. Specifically, the limit for the pressure of the three-flavor system is $p_{SB}/T^4 \approx 5.209$, while the energy density is $\epsilon_{SB} = 3p_{SB}$, and the entropy density is $s_{SB} = 4p_{SB}/T$ (these limits are all shown as arrows in Figures).

Figures 11 and 12 are results for the energy density and the entropy density, and Figures 13 and 14 demonstrate the speed of sound and p/ϵ.

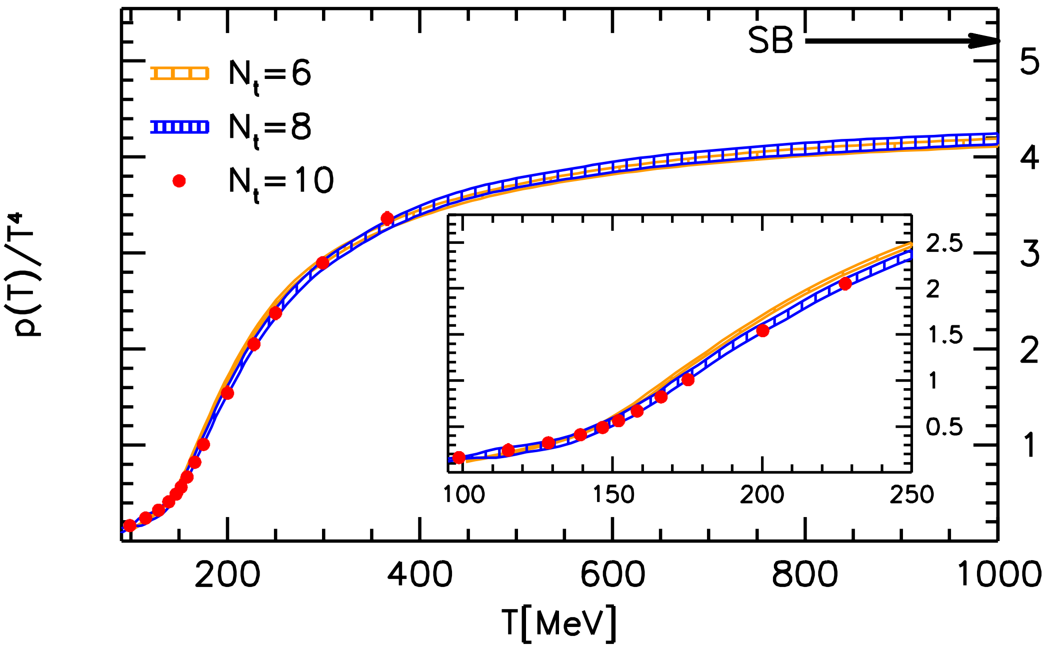

Figure 10: The pressure normalized by T^4 as a function of the temperature [70].

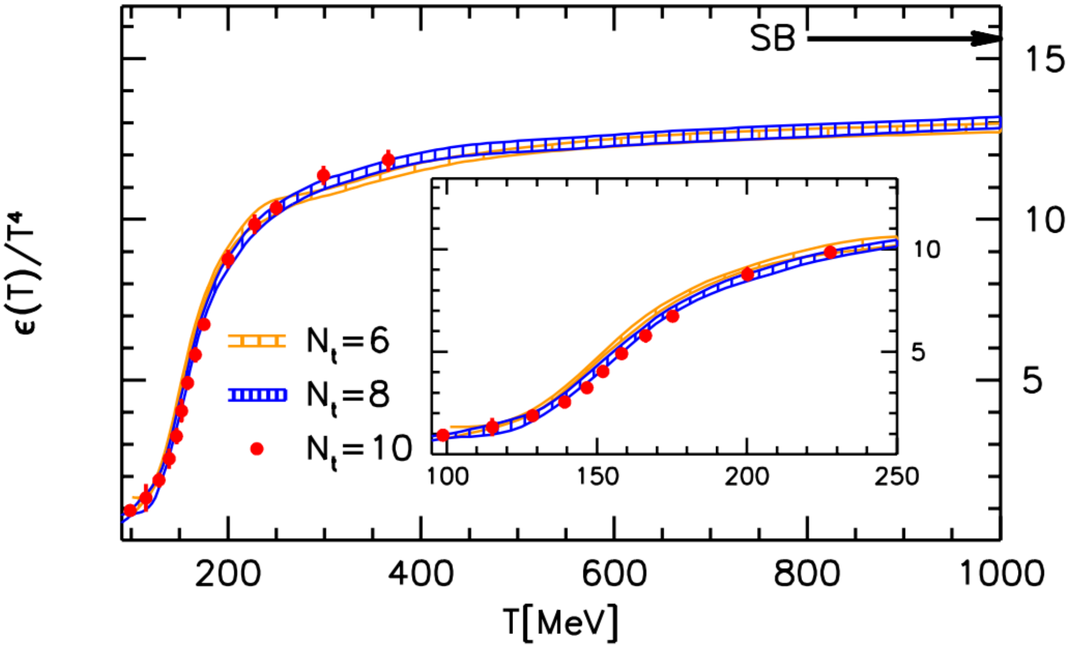

Figure 11: The plot shows the energy density divided by T^4 as a function of temperature for lattices with N_t values of 6, 8, and 10. An arrow indicates the Stefan-Boltzmann limit of $3p_{SB}$ [70].

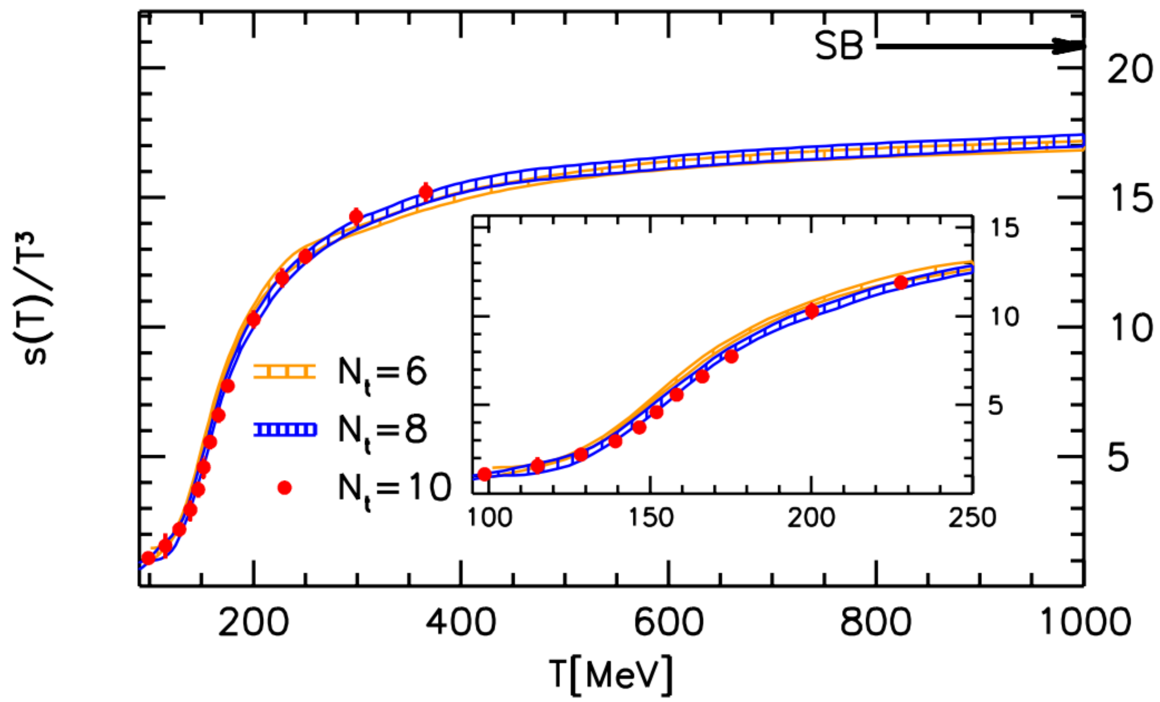

Figure 12: The graph displays the entropy density divided by T^3 plotted as a function of temperature for lattices with N_t values of 6, 8, and 10. An arrow is used to indicate the Stefan-Boltzmann limit of $s_{SB} = 4p_{SB}/T$ [70].

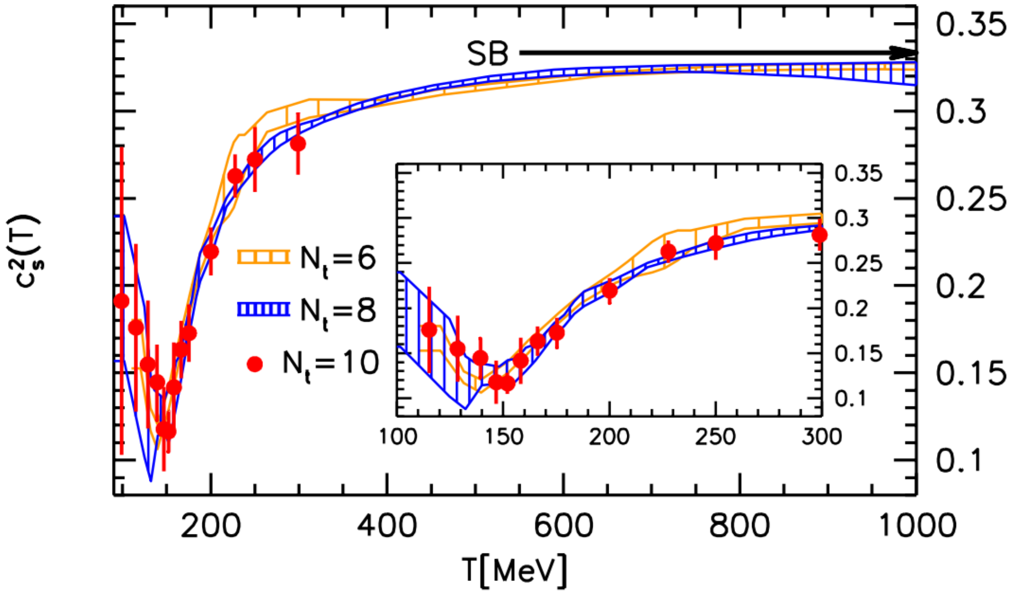

Figure 13: The graph illustrates the square of the speed of sound plotted as a function of temperature for lattices with N_t values of 6, 8, and 10. An arrow indicates the Stefan-Boltzmann limit of $c^2_{s,SB} = 1/3$ [70].

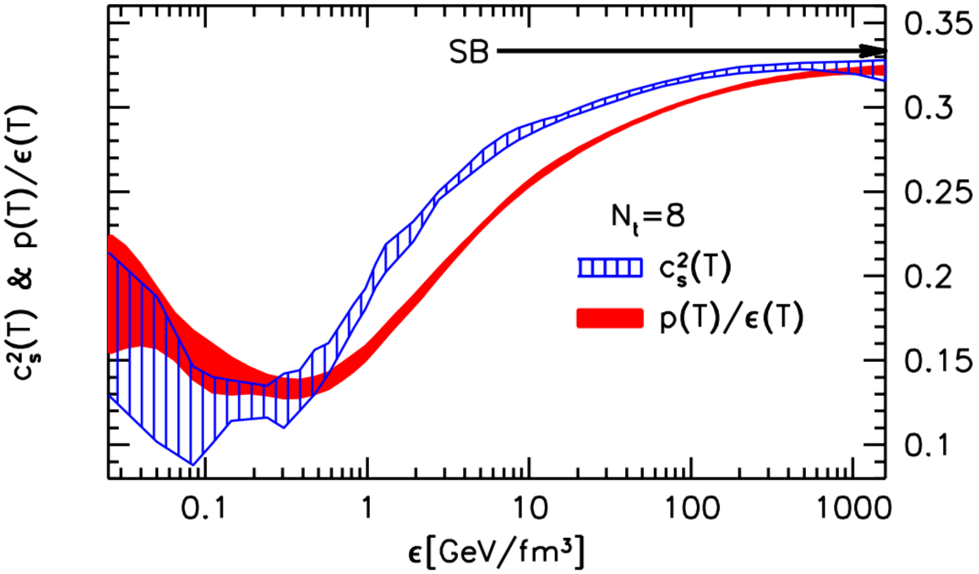

Figure 14: This plot shows the relationship between the energy density on $N_t = 8$ lattices and the speed of sound and p/ϵ. An arrow is used to indicate the Stefan-Boltzmann limit [70].

2 Definitions and Terminology

2.1 ALICE Coordinate System and Transverse Momentum

Figure 15 demonstrates the coordination space used in the ALICE detector. The beam axis is in the z-direction, and the xy-plane, which is perpendicular to the beam direction, is called the transverse plane. The center of the detector locates at x = y = z = 0. The angle between the x direction and the projection of the produced particle direction in the transverse plane is referred to as the azimuthal angle and is denoted as φ. The angle between the z direction and the direction of the produced particle is referred to as the polar angle or θ.

The mean transverse momentum, $\langle p_{\mathrm{T}} \rangle$, and its correlation with the charged-particle multiplicity N_{ch} carries essential information on the underlying particle production processes. In this dissertation, this has been studied by using Xe–Xe and Pb–Pb collisions at $\sqrt{s_{\mathrm{NN}}} = 5.44$ TeV and $\sqrt{s_{\mathrm{NN}}} = 5.02$ TeV, respectively. Basically, the corelation between $\langle p_{\mathrm{T}} \rangle$ and N_{ch} is an observable for tuning theoretical models. Besides, it allows the extraction of fundamental properties of a deconfined quark–gluon medium. Transverse momentum can be expressed by two momentum components on the transverse plane:

$$p_{\mathrm{T}} = \sqrt{p_x^2 + p_y^2}$$

where p_x and p_y are the momentum components in the x and y directions, respectively.

2.2 Rapidity and Pseudorapidity

Rapidity characterizes the momentum component of a produced particle in the longitudinal or z direction. A key property of rapidity is that differences in rapidity are invariant under a Lorentz transformation in the z direction [11]. It can be expressed as:

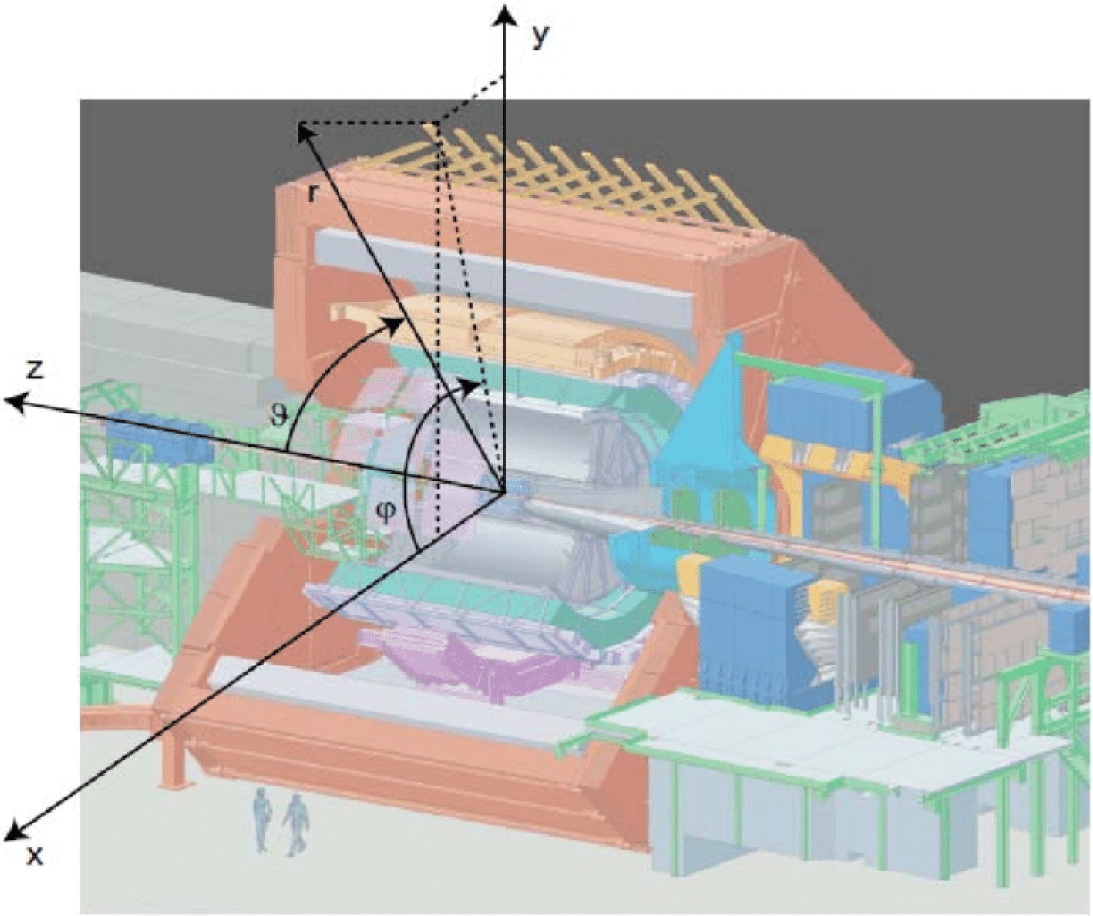

Figure 15: A schematic view of ALICE coordinate system axis and angles. Figure taken from [10].

$$y = \frac{1}{2} \ln \left(\frac{E + p_z}{E - p_z} \right) \tag{12}$$

where E and p_z are the total energy of the particle and longitudinal momentum along the z-axis, respectively. However, it is common to use pseudorapidity η since the total energy of the particle is not always known because the mass of the particle is not always known in the equation:

$$E^2 = p^2 + m_0^2 \tag{13}$$

When the speed of the particle is very close to the speed of light, the energy coming from the particle's mass is approximately zero, so $E \approx p$, and one can neglect the second part in Equation (13); thus the rapidity (y) approaches the pseudorapidity and can be expressed as below:

$$\eta = -\ln\left[\tan\left(\frac{\theta}{2}\right)\right], \tag{14}$$

where θ, is the angle between the collision axis and the particle's momentum vector, just like rapidity, differences in pseudorapidity (η) are also Lorentz invariant [30]. This is the reason why pseudorapidity (η) is used to describe the angle of a particle relative to the beam axis plane instead of θ since the Lorentz transformations become very complicated.

2.3 Impact Parameter and Centrality

A schematic view of heavy ion collisions is shown in Figure 16, in which two nuclei are coming toward each other in opposite directions. The variable b is the impact parameter, which refers to the length connecting the centers of the colliding nuclei in the transverse plane.

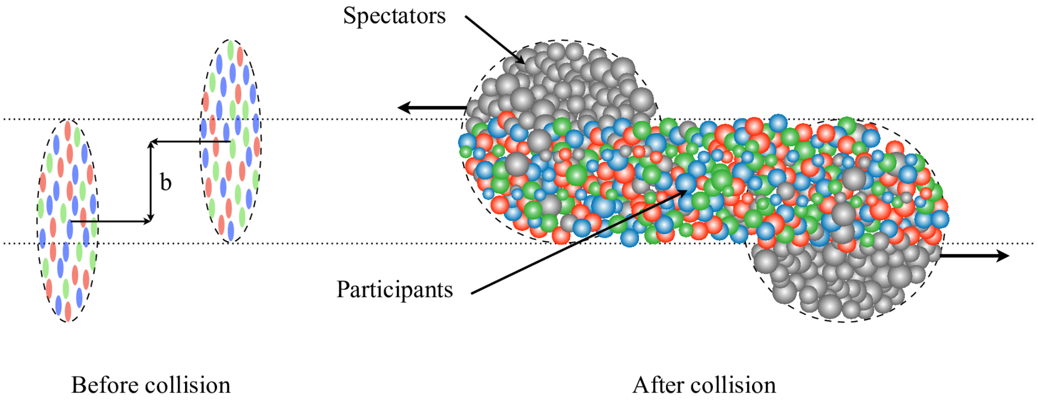

Figure 16: A schematic view of a heavy-ion collision [50]

Centrality is used to characterize the collision geometry with respect to the impact parameter b. When $b = 0$, the centrality is 0%, and this is referred to as a "head-on collision" since all the matter of the incoming nuclei participates in the interaction. Large values of centrality correspond to larger values of b, and therefore less matter will participate in the interaction. The impact parameter cannot be measured experimentally, since direct access to the collision is not possible. Instead, the multiplicity of produced particles is used to determine the centrality. This is based on the intuitive assumption that the number of particles produced in the collision increases monotonically with an increasing number of participating nucleons and, therefore, with decreasing values of b.

The impact parameter (b) plays a significant role in ultrarelativistic nucleus-nucleus collisions as it determines the size and transverse shape of the quark-gluon matter created during the collision. When the impact parameter is small, central collisions occur, resulting in large and circular interaction regions. However, when the impact parameter is large, peripheral collisions happen, producing smaller interaction regions with a pronounced elliptical anisotropy. On the other hand, elliptic flow [15, 16] arises from the elliptical shape of the nuclear overlap region and is more prominent in peripheral events [17]. The dependence of various observables on centrality provides insight into their relationship with the global geometry of the collision. High-momentum particles [12, 13] or jets [14], (more detail about jets are explained in Appendix A) tend to lose more energy in central collisions, as their path length inside the quark-gluon plasma is longer.

As mentioned before, at extremely high energies, the impact parameter of a single collision is a well-defined quantity and has negligible quantum uncertainty, but it cannot be directly measured in experiments. Instead, a single observable (denoted as n) [18] is used to estimate the impact parameter, which can either be the number of produced particles in a detector [19, 20, 21, 22] or the transverse energy deposited in a calorimeter [23, 24]. The general idea is that collisions with smaller impact parameters tend to produce larger values of n. However, the relationship between n and the impact parameter is not one-to-one, and the variation of n with the impact parameter is unknown. This relationship is typically inferred from a microscopic model of the collision, such as the HIJING [25] model or a two-component Glauber model [26], coupled with a simple particle production model. These models are calibrated to match the observed probability distribution of n, but they may not accurately describe the actual dynamics of a collision. During experiments, collisions are categorized based on a single measure, denoted as n. The definition of n varies among different collaborations. For instance, the STAR Collaboration [27] defines n as the number of tracks detected within the pseudorapidity range of $-0.5 < \eta < 0.5$, while the ALICE Collaboration [22] uses the count of hits in two scintillators that cover the windows $-3.7 < \eta < -1.7$ and $2.8 < \eta < 5.1$. The ATLAS [24] and CMS Collaborations [28], on the other hand, utilize the energy deposited in two forward calorimeters with acceptance windows of $3.2 < |\eta| < 4.9$ and $3.0 < |\eta| < 5.2$, respectively.

The centrality with respect to the number of produced particles is defined as:

$$c = \frac{1}{N_{\text{events}}} \int_{M_0}^{\infty} \frac{dN}{dM} dM. \tag{15}$$

The term M, also referres to as the multiplicity is the number of particles produced in a heavy-ion collision. The term M_0 refers to a set of collisions with a particular multiplicity, of which the centrality c is determined. The term N_{events} represents the number of collisions, and dN/dM is the number of collisions as a function of the multiplicity M.

As illustrated in Figure 17, more particles are produced for the lower centrality percentages (central collisions) and fewer particles for the higher centrality percentages (peripheral collisions).

2.4 Initial State Models

One of the primary goals of heavy-ion physics is to determine the properties of the quark-gluon plasma (QGP), such as the characteristics of the initial state that leads to its formation. Due to the fact that the QGP medium created in heavy-ion collisions is highly transient, its properties are not directly measurable. One can compare the computational models, such as initial state models, to experimental observations. In heavy-ion collision experiments, initial state models are used to create energy or density profiles before the Quark-Gluon Plasma (QGP) formation occurs in the overlap region. Having an accurate initial state model is crucial to accurately calculate the essential properties of the QGP medium. The QGP behaves like an almost perfect fluid, and calculations

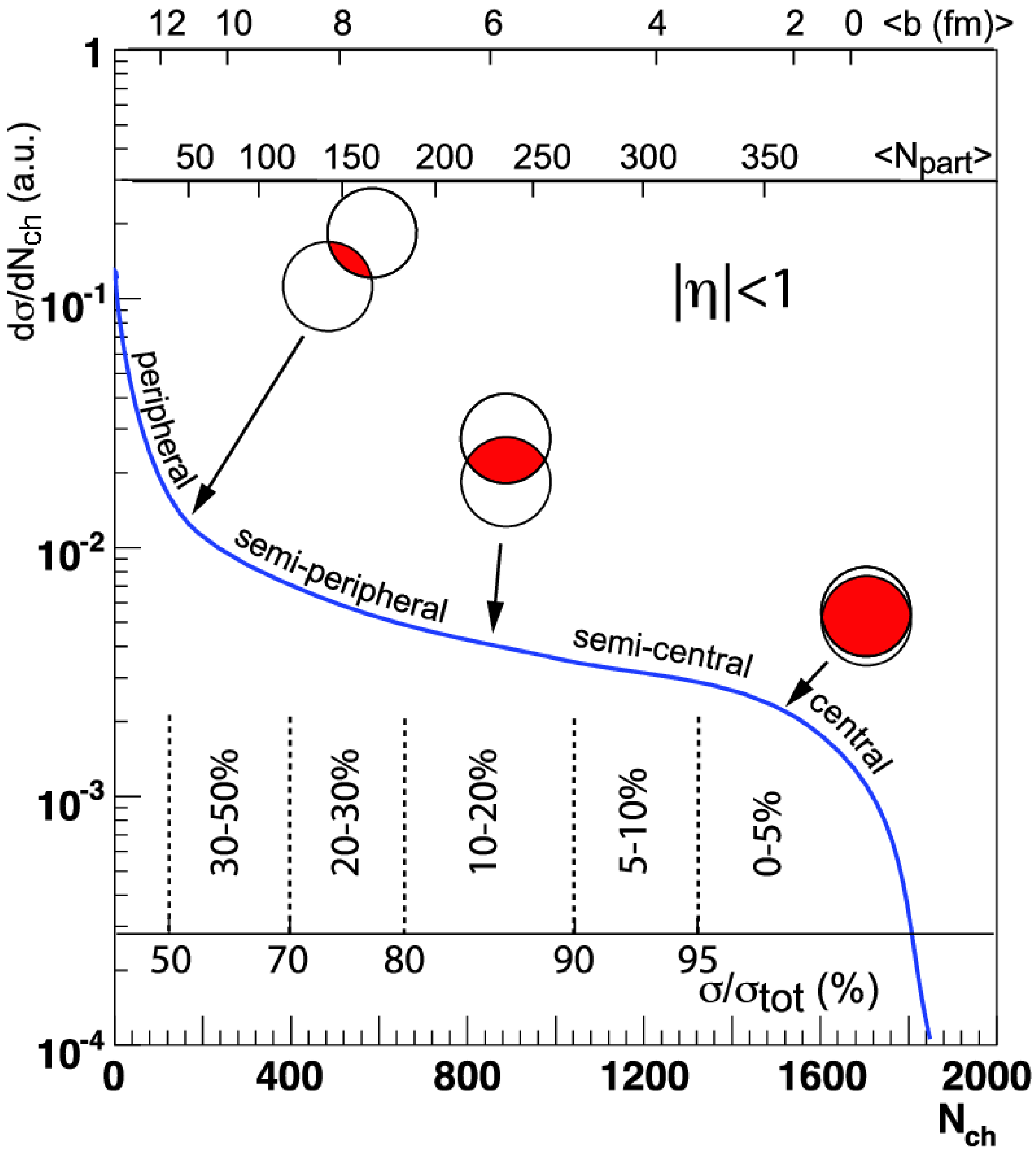

Figure 17: Correlation between final state observable (Multiplicity) and impact parameter. The Figure is taken from [29]

using different initial state models have shown that relativistic viscous hydrodynamics can often describe the multiplicity distributions, particle spectra, and integrated flow measurements at the same time. The measurement of azimuthal anisotropies in the initial state has been the subject of extensive research in recent decades. Specifically, the use of Fourier decomposition and flow coefficients (v_n) to describe observed azimuthal anisotropies have been studied in detail.

Anisotropic flow occurs as a result of the initial spatial anisotropy of a system formed during heavy-ion collisions. By using Fourier expansion, we can examine the azimuthal variation of the particles produced, breaking down the distribution into different flow harmonics or Fourier coefficients. This process allows us to analyze the angular distribution of the particles relative to the angles of the symmetry planes and can be written as:

$$\begin{aligned} \frac{dN}{d\varphi} &\propto 1 + 2\sum_{n=1}^{\infty} v_n \cos\left[n\left(\varphi - \Psi_n\right)\right] \\ &\propto 1 + 2\left\{v_1 \cos\left[\left(\varphi - \Psi_1\right)\right] + v_2 \cos\left[2\left(\varphi - \Psi_2\right)\right] + \cdots\right\}, \end{aligned} \tag{16}$$

As mentioned before, φ is defined as the azimuthal angle, and Ψ_n represents the n-th order symmetry and also indicates the direction of anisotropic flow with order n. The magnitude of anisotropic flow is measured using flow harmonics denoted by v_n. Elliptic flow and triangular flow are represented by the second and third harmonics, v_2 and v_3, respectively. The initial almond-shaped interaction region causes the second-order flow to be the dominant component in the Fourier expansion. On the other hand, the third-order flow is solely caused by fluctuations in the initial state density as shown in Figure 18.

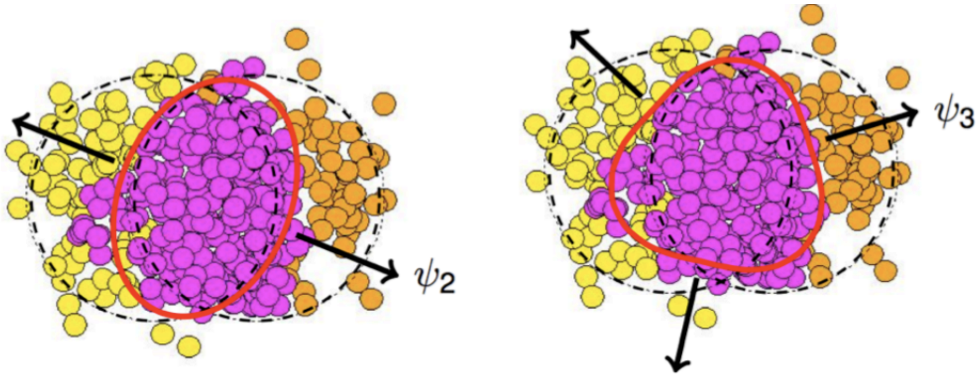

Figure 18: Graphic illustration of v_2 and v_3

The nuclear matter in the interaction region during a heavy-ion collision experiences fluctuations on an event-by-event basis. Anisotropic pressure gradients, which are most pronounced in the direction of the arrows in Figure 18 (where the arrows correspond to the respective Ψ_n angles), drive both types of flow. Because these flows are influenced by the medium's pressure, studying them can reveal details about the equation of the state of the quark-gluon plasma. By comparing the observed flow coefficients with initial state models such as MC Glauber and TRENTo, one can constrain the transport properties of the QGP, such as the ratio of shear and bulk viscosity to entropy.

2.4.1 The TRENTo Model

What initial state models do, is generate the energy or entropy density after the collision. There are two main methods for creating profiles of energy or entropy at the time of the QGP [57] thermalization that can be used in fluid dynamics. The first approach is through dynamical models, which simulate both the initial state and pre-equilibrium evolution of the collision [58, 59]. The second approach involves using simpler nondynamical models, which do not consider pre-equilibrium evolution and instead construct static profiles at the time of thermalization. Non-dynamic models create initial conditions at the time of thermalization by making assumptions about the deposition of entropy. Although they cannot account for the formation of the QGP, they do provide the required information for fluid dynamics and can limit the results of ab initio initial-condition calculations. The two-component Monte Carlo Glauber model is the most commonly employed method for this purpose. It determines which nucleons participate by measuring the optical overlap and assigns energy or entropy for each participant as well as for binary nucleon-nucleon collisions. The TRENTo model, on the other hand, utilizes the Reduced Thickness Event-by-event Nuclear Topology model as a new initial-condition approach for high-energy collisions involving proton-proton, proton-nucleus, and nucleus-nucleus. It is an efficient method that aims at producing practical Monte Carlo initial entropy profiles without making any specific assumptions about the physical mechanisms responsible for entropy production, pre-equilibrium dynamics, or thermalization [6]. The TRENTo model [6] can be applied in high-energy proton-proton, proton-nucleus, and nucleus-nucleus collisions. Consider two projectiles Labeled A and B colliding along the beam axis z.

Suppose that the density of nuclear matter that participates in inelastic collisions is $\rho_{A,B}^{\text{part}}$. As a result, each projectile might be represented by its participant thickness [6]:

$$T_{A,B}(x,y) = \int dz \rho_{A,B}^{\text{part}}(x,y,z), \tag{17}$$

then consider a so-called reduced thickness (see Figure 19):

$$T_R\left(p; T_A, T_B\right) \equiv \left(\frac{T_A^p + T_B^p}{2}\right)^{1/p}, \tag{18}$$

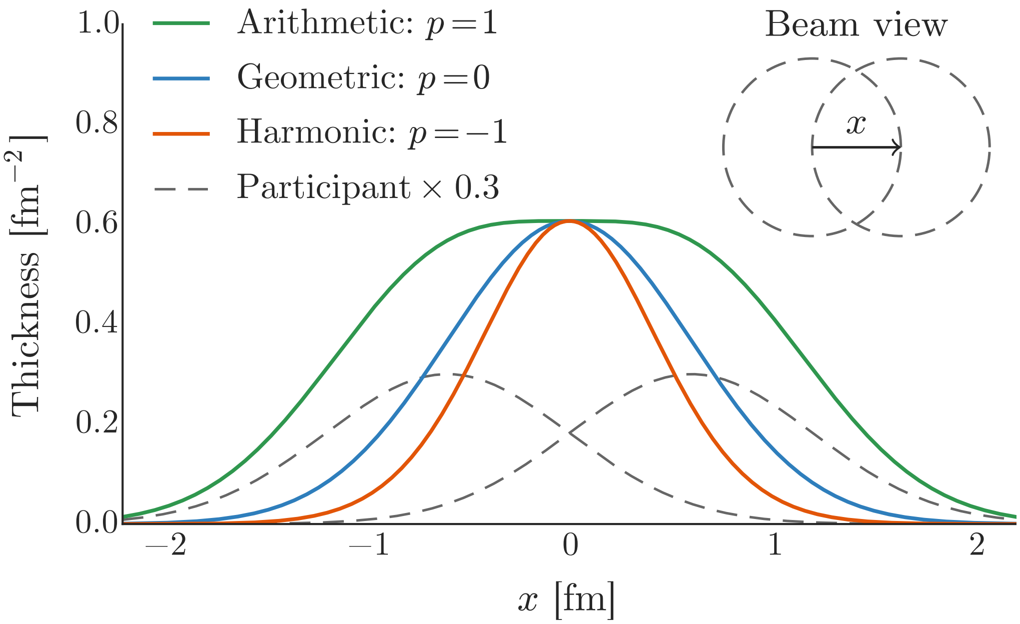

Figure 19: Reduced thickness of a pair of nucleon participants. The grey dashed lines are one-dimensional cross sections of the participant nucleon thickness functions T_A, T_B. The colored lines are the reduced thickness T_R for p = 1, 0, -1 (green, blue, orange).

so named due to the fact that it takes two thicknesses T_A and T_B and reduces them to the third thickness, which is similar to the reduced mass [6]. Here, p is the key parameter and controls the nuclear matter distribution in the initial conditions. Firstly, nucleon positions should be sampled, and then computing the participant nuclear thickness functions T_A, T_B, TRENTo deposits entropy according to the ansatz:

$$s \propto \left(\frac{T_A^p + T_B^p}{2} \right)^{1/p} \tag{19}$$

where p is a continuous parameter that is tunable, that effectively interpolates among different entropy deposition schemes (see Figure 20). When $p = 1$, the ansatz reduces to a wounded nucleon model ($\boldsymbol{s} \propto \boldsymbol{T}_A + \boldsymbol{T}_B$), while $p = 0$ implies entropy deposition proportional to the geometric mean of thickness functions ($s \propto \sqrt{T_A T_B}$).

2.5 Simulation Studies

Monte Carlo event generators can be beneficial for producing output that can be compared directly to many experimental observables, including limited acceptance calorimeters, charged particle correlations, etc. Besides, event generators are helpful for planning and designing future experiments.

In heavy ion collision experiments, the detected dataset has limited statistics. In addition, the detectors' data collection has limited efficiency. Therefore, it is essential to know the detector efficiencies and how to do the corrections for the detector effects. Also, depending on the analysis, various event generators are used for Monte Carlo (MC) studies. This is addressed through HIJING and GEANT Monte Carlo simulations.

2.5.1 GEANT Model

GEANT [7] is an acronym formed from “GEometry ANd Tracking” and a collection of tools used for simulating and describing detectors as the complexity of High Energy Physics experiments increases. Its main purposes are to create and evaluate reconstruction and analysis programs, design and optimize the detectors and comprehend the experimental data. it was originally created for use in High Energy Physics experiments, and it is designed to model the movement of fundamental particles as they travel through different types of matter. Its applications are: tracking the particles through the experiment to simulate the detector response and graphical demonstration of the

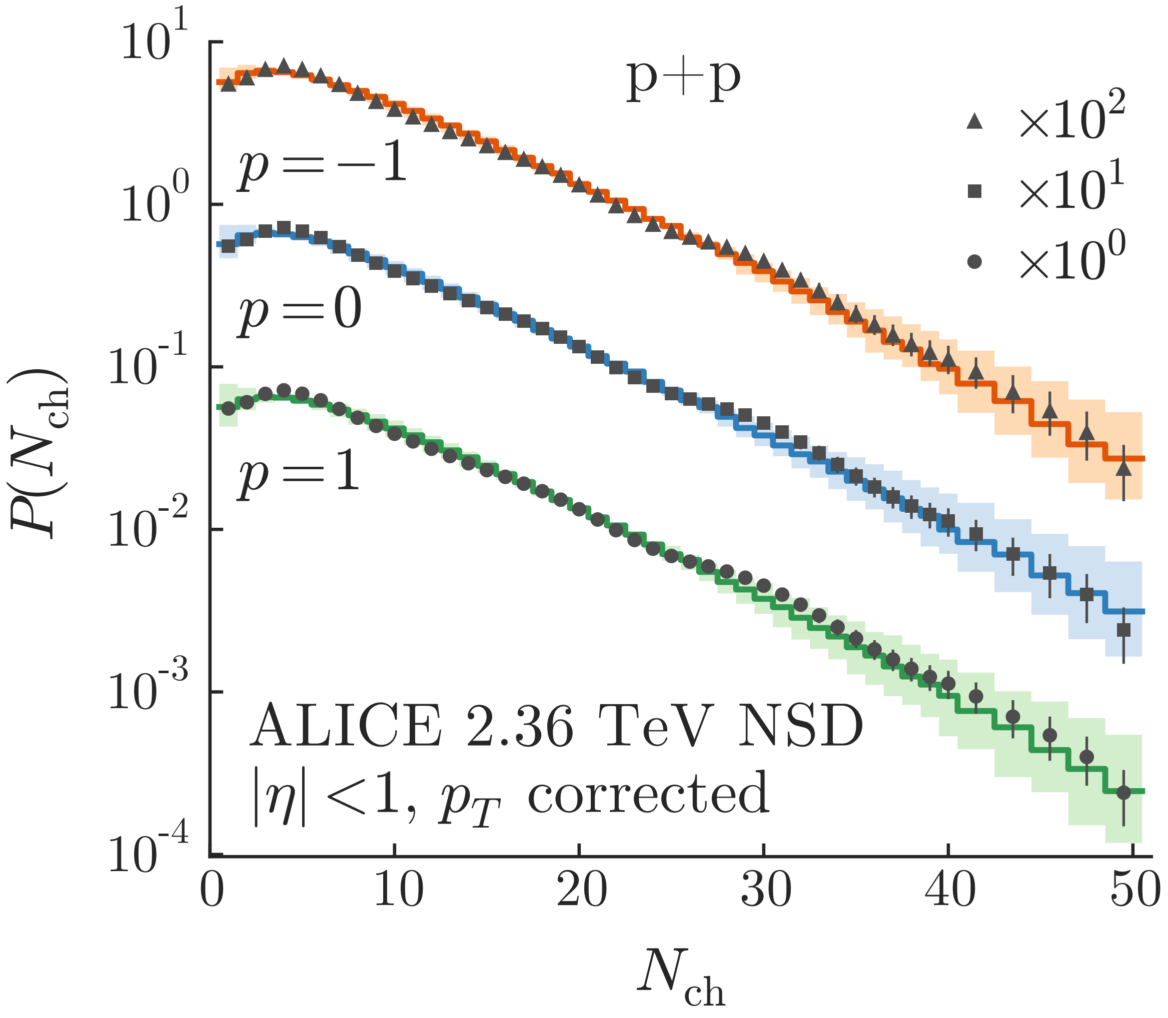

Figure 20: Multiplicity distributions for proton-proton collisions. The histograms are TRENTo results for reduced thickness parameter $p = -1$ (top, orange), $p = 0$ (middle, blue), and $p = 1$ (bottom, green) [6].

setup and particle trajectories. Based on these applications, it is possible to represent an experimental configuration using a series of geometrical volumes, each of which is assigned a numerical medium value (referred to as "GEOM") by the user. It is possible for different volumes to have the same medium number. The characteristics of each medium are determined by the "TRACKING MEDIUM" parameters, which include information about the material that fills the volume. It will also allow us to accept events simulated by Monte Carlo generators. The GEANT software is capable of transporting particles through different sections of an experimental setup while considering factors such as the boundaries of geometrical volumes, the nature of the particles being studied, their interactions with matter, and the presence of a magnetic field. This enables researchers to better understand the behavior of particles in complex experimental configurations. In addition, GEANT is capable of recording important data such as particle trajectories and the reactions of sensitive detectors. The software also includes features that allow researchers to visualize both the detectors and the trajectories of the particles being studied.

2.5.2 HIJING Model

Heavy Ion Jet Interaction Generator (HIJING) is a Monte Carlo model for multiple jet production in pp, pA, and AA collisions [8]. By merging perturbative-QCD motivated models for producing multiple jets with low p_T multi-string observations, they have created this Monte Carlo event generator. The generator is designed to examine the production of jets and multiple particles in high-energy collisions involving pp, pA, and AA interactions. The model incorporates the generation of numerous mini-jets, as well as the nuclear shadowing of parton distribution functions, and a simplified mechanism for jet interactions that occur within a dense environment. Some of the main features included in HIJING are as follows. The number of inelastic processes and their dependence on the impact parameter are calculated using precise diffuse nuclear geometry, as stated in [9]. Besides, a parton structure-function that depends on the impact parameter is presented, to investigate how nuclear shadowing affects observables, with a particular focus on the structure functions of the gluon. In addition, the analysis includes a jet quenching model that allows the examination of how moderate and high p_T observables are affected by an assumed parton energy loss (dE/dx) as they pass through the produced dense matter.

HIJING incorporates a successful multi-string phenomenology that is suitable for studying low p_T interactions at intermediate energies. As a result, it provides a connection between the dominant nonperturbative fragmentation physics at intermediate CERN Super Proton Synchrotron (SPS) energies and the perturbative QCD physics at the highest collider energies that are expected. However, HIJING does not account for the mechanism of final state interactions among the low p_T particles produced, which limits its ability to address the approach to local equilibration. The primary goal of HIJING is to explore the range of potential initial conditions that may occur in nuclear collisions at collider energies. In contrast, the model also incorporates a basic approach to the final state interactions of high p_T partons through an effective energy loss parameter, dE/dx, to examine the extent of jet quenching that may arise from such collisions.

3 Experimental Setup

In this chapter, the features of the experimental setup will be introduced for a brief introduction to the Large Hadron Collider (LHC). Then one of the major experiments at CERN will be described: A Large Ion Collider Experiment (ALICE). Finally, a comprehensive explanation of the ALICE sub-detectors, whose data are utilized in this thesis, will be provided.

3.1 The LHC at CERN

The largest and most powerful particle accelerator, also known as the Large Hadron Collider(LHC), is built at CERN, the European Organization for Nuclear Research, near Geneva, Switzerland. It is 27 kilometers in circumference, has a ring of superconducting magnets, and has an average depth of 100 meters underground beneath the French-Swiss border. It was built from 1998 to 2008, steering the first beam on 10 September 2008. It consists of two beam pipes where particles, beams of protons or ions, move in two opposite directions. The LHC houses four main experiments, located along the superconducting ring: ALICE (A Large Ion Collider Experiment), ATLAS (A Toroidal LHC Apparatus), CMS (Compact Muon Solenoid experiment), and LHCb (LHC beauty) (see Figure 21).

Each experimental setup is built for different purposes. The ATLAS and CMS were built with the same goal and were designed mostly to analyze proton-proton collisions for detecting the Higgs boson and physics beyond the standard model. The LHCb experiment studies particles containing the b quark in order to investigate the slight difference between matter and antimatter. However, the main goal of the ALICE experiment is to study Quark-Gluon plasma (QGP) and its phase transition to hadronic matter. The Large Hadron Collider started its third period of operation (Run 3) in July 2022. Since then, it has been colliding protons at a record-breaking energy of 13.6 TeV (6.8 TeV per beam). Also, Pb-Pb is accelerated and collided at a record energy of 5.36 TeV per nucleon-nucleon collision. In addition to higher energy, the LHC is expected to reach a higher luminosity.

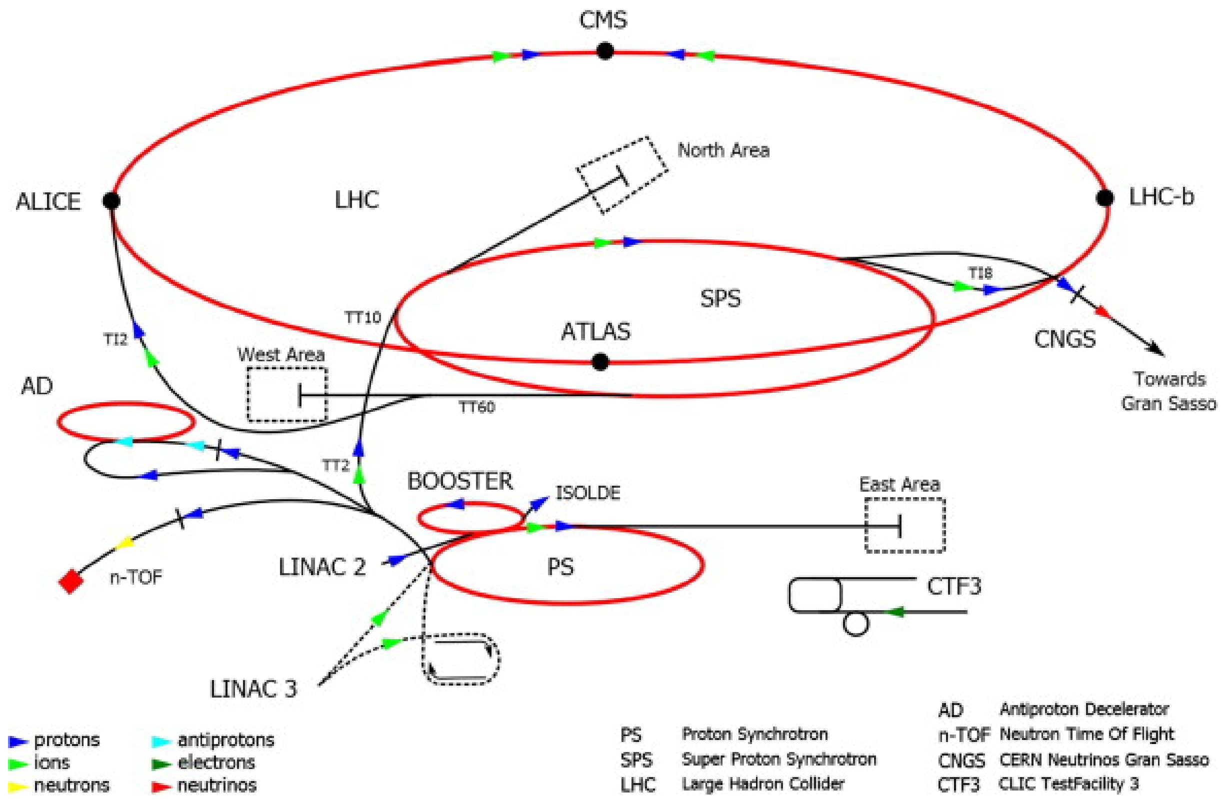

Figure 21: A schematic view of the accelerator complex at CERN

3.2 A Large Ion Collider Experiment (ALICE)

The ALICE [46, 47, 48] (A Large Ion Collider Experiment) collaboration includes nearly 2000 scientists from 174 physics institutes in 40 different countries [49]. The detector has overall dimensions of $16\times16\times26$ m^3 and is approximately 10,000 tons in weight (see Figure 22). It was designed to cope with the particle densities expected in central Pb–Pb collisions at the LHC. It is one of the main experiments at the LHC and has been designed to study QGP matter created in high-energy collisions between lead nuclei.

The experiment has a high detector granularity, a low transverse momentum threshold $p_{\mathrm{T}}^{\mathrm{min}} \approx$ 0.15GeV/c, and good particle identification capabilities up to 20 GeV/c. There are seventeen sub-detectors of three categories: central-barrel detectors, forward detectors, and the MUON spectrometer. In this section, a brief outline of their features is given. The central-barrel detectors are Inner Tracking System (ITS), Time Projection Chamber (TPC), Electromagnetic Calorimeter

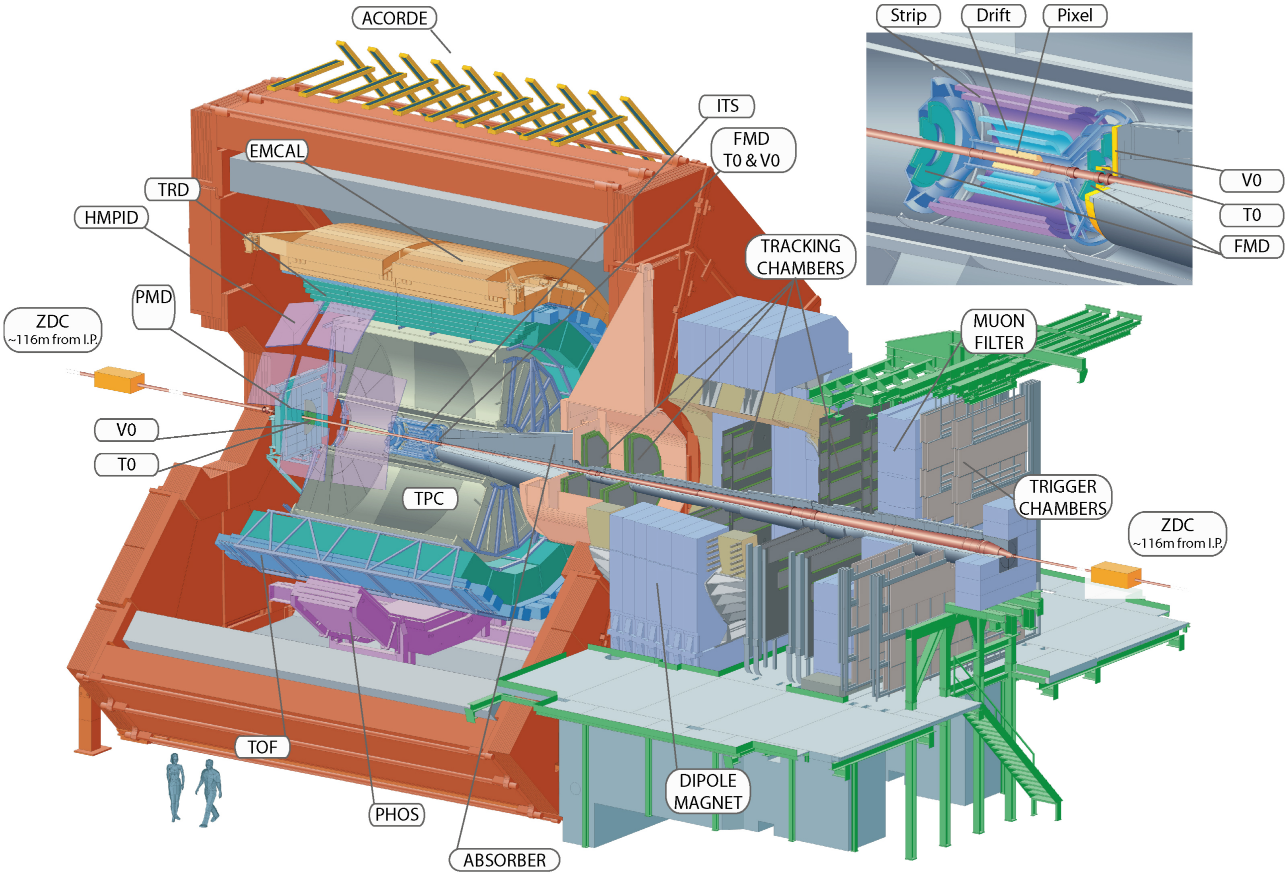

Figure 22: The ALICE experiment at the LHC

(EMCal), Time Of Flight (TOF), Photon Spectrometer (PHOS), Transition Radiation Detector (TRD) and High Momentum Particle Identification Detector (HMPID). The Inner Tracking System and the Time Projection Chamber are the main charged-particle tracking detectors in ALICE. In addition to tracking, SDD, and TPC provide charged-particle identification by measuring the specific ionization energy loss dE/dx. The detectors used in this dissertation are Time Projection Chamber (TPC), Inner Tracking System (ITS), and VZERO (V0). More details can be found in Ref. [48].

3.2.1 Time Projection Chamber (TPC)

Overall, the ALICE Time Projection Chamber (TPC) is a critical component of the ALICE experiment and provides essential information for many aspects of the physics program at the LHC. The TPC is a central tracking and particle identification detector (PID). By combining the information from multiple measurements, the TPC can determine the trajectory of the charged particles and their momenta. It covers a symmetric pseudorapidity interval around midrapidity $|\eta| < 0.9$ and a full azimuthal angle.

The TPC has a cylindrical shape that surrounds the ITS with a length and outer diameter of about 5 m, resulting in a total volume of 88 m^3 and a length along the beam axis of 500 cm, filled with $Ne - CO_2 - N_2$ (see Figure 23). It employs a cylindrical field cage with a high-voltage electrode in its center, dividing its volume into two halves (see Figure 23). Each of the two endplates includes 18 inner and outer readout chambers, which are arranged in pairs to form 18 equal azimuthal sectors. The TPC was successfully operated in pp, p–Pb, Pb–Pb, and Xe–Xe collisions at a variety of collision energies during LHC Run 1 and Run 2 [64].

The ALICE TPC and other central-barrel detectors sit inside a 0.5 T solenoidal magnetic field [26]. This constant magnetic field, combined with the electric field from the TPC, will cause charged particles moving through the chamber to have a curved path or helical motion. The direction of the charged particle is determined by the initial kinematics after the collision and the electric field. It operates by detecting the ionization of gas atoms caused by the passage of charged particles. When a charged particle from a collision enters the TPC, the particle traverses the gas chamber, ionizing gas molecules. The electric field drifts the resulting ionization electrons toward a set of readout electrodes, where the position and amount of the ionization can be measured. This drift is based on the central high voltage electrode with electric potential, which creates a uniform electric field in the z-direction [65]. Ionization plays a special role because it is a function of particle velocity. Each plate provides a maximum of 159 points along the particle path for tracking. The read-out pad provides the coordinate in the $x-y$ plane, whereas the z-coordinate is calculated from the drift time and drift velocity. The maximum drift time is approximately 88 μs. As a charged particle passes

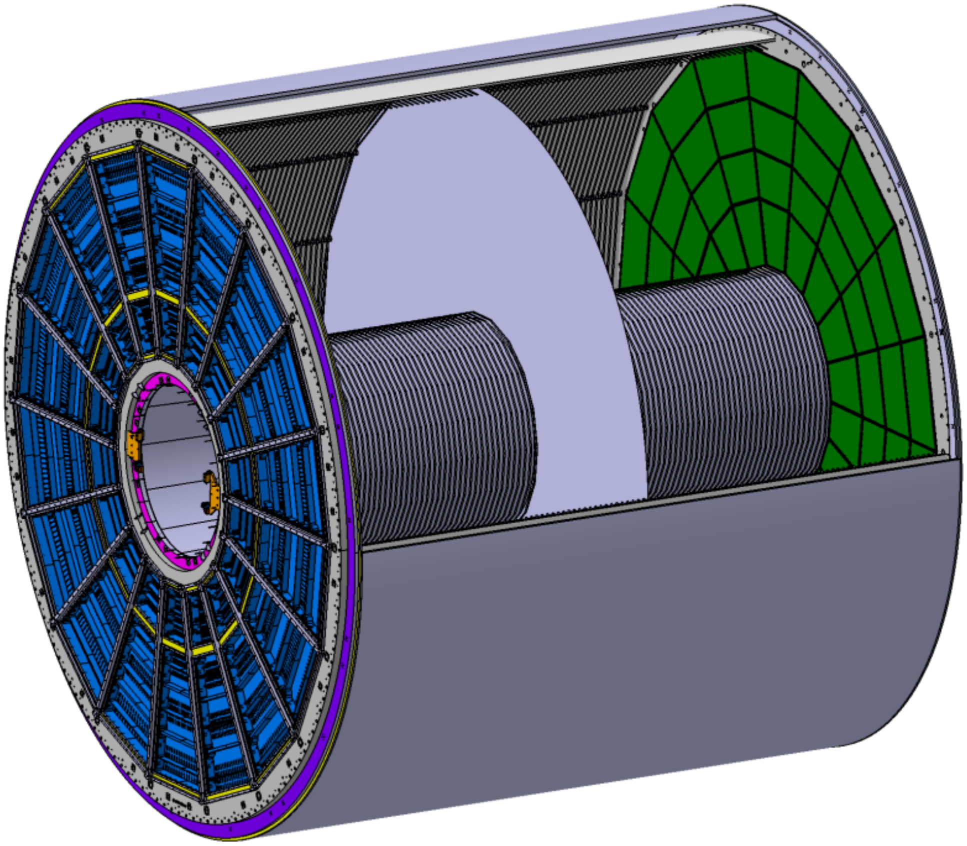

Figure 23: Schematic view of the ALICE TPC

through the gas mixture medium, the inelastic collisions between a produced charged particle and atoms in the gas result in the ionization of the gas, which corresponds to a decrease in the particle energy. The energy loss depends on the momentum of the produced particle.

3.2.2 Inner Tracking System (ITS)

The innermost detector of ALICE is called Inner Tracking System (ITS) and is the closest detector to the collision point. Its distance from the beam line ranges from 3.9 cm for the innermost layer and 43 cm for the outermost. Its goal is to determine the primary collision vertex to a resolution better than 100 μm and to help improve the resolution of p_{T} and angle from reconstructed particles by the TPC. Also, it provides momentum determination for low momentum particles, which are less than 200 MeV/c [75] and cannot be measured by the TPC. The ITS consists of six tracking layers: two Silicon Pixel Detectors (SPD), two Silicon Drift Detectors (SDD), and two Silicon Strip Detectors (SSD) (see Figure 24).

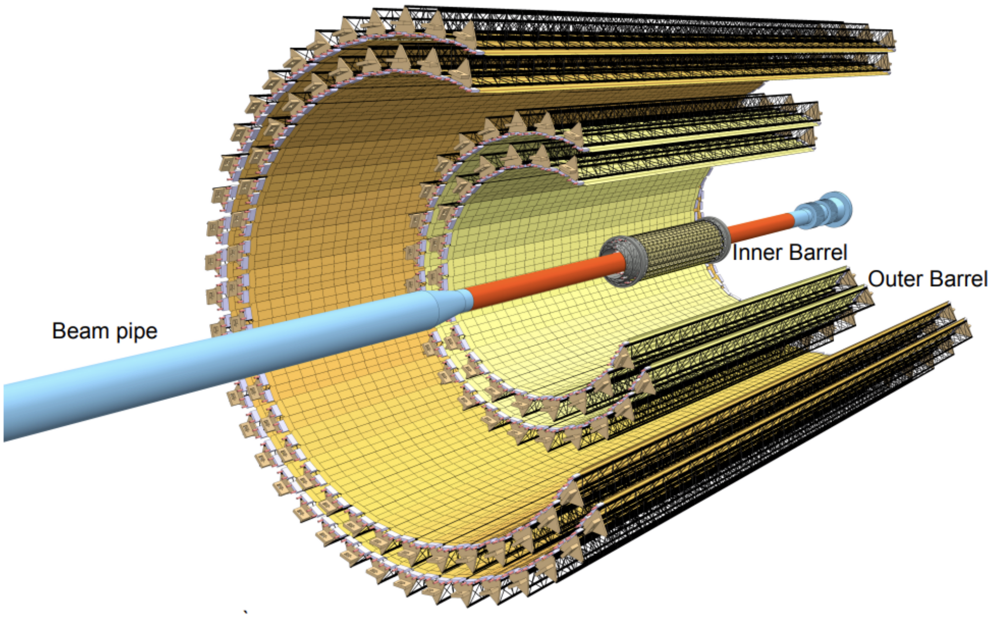

Figure 24: Schematic view of cylindrical detector ITS that is made up of six total layers.

The two innermost layers are silicon pixel detectors (SPD), high spatial resolution detectors that can provide two-dimensional hit information, which is required for primary vertex determination. The SPD has a resolution of about 0.5 percent centrality bin width, which can be used for centrality determination. These layers are located at radii of 3.9 cm and 7.6 cm away from the beam axis and can cover pseudorapidity of $-1.98 < \eta < 1.98$. The third and fourth layers are located at radii of 15.0 cm and 23.9 cm away from the beam axis and consist of silicon drift detectors (SDD). Their main function is to determine the drift time of the charge deposited when a particle passes through the detector together with the segmentation through cathode strips to determine the position of the particle by providing energy-loss information (dE/dx) (see Figure 25).

Silicon Strip Detectors (SSD) consist of the two outermost layers of the ITS, which are located at

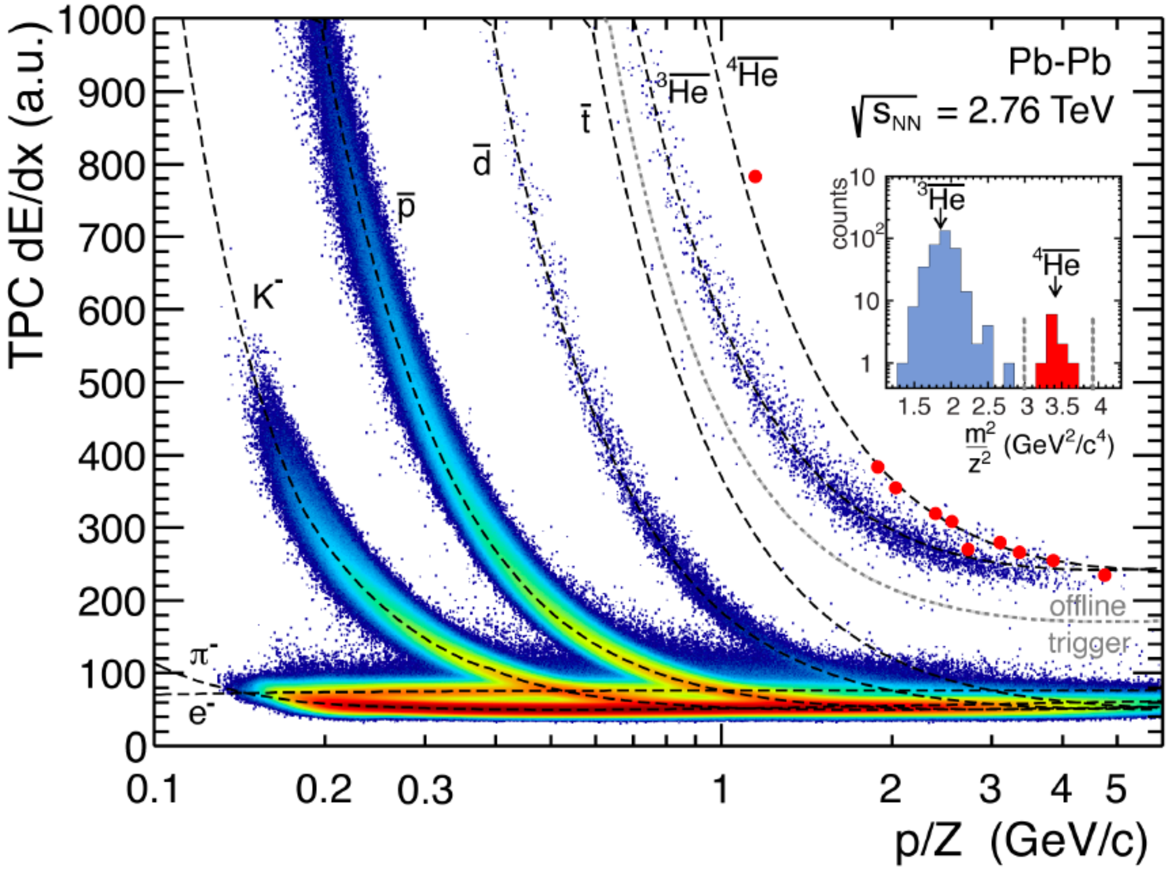

Figure 25: TPC energy loss dE/dx measurements as a function of magnetic rigidity for 2011 Pb-Pb data. The Figure is taken from [63].

radii of 30.0 cm and 43.0 cm away from the beam axis. SSDs are equipped with double-sided Silicon Strip Detectors and cover the pseudorapidity range $|\eta| < 0.9$ with full azimuthal coverage, which provides a two-dimensional measurement of track position, which is very important in matching tracks from the ITS to the TPC. They also provide energy loss (dE/dx) information for PID. More details of the ITS detector are shown in Figure 26.

3.2.3 VZERO (V0)

The V0 detector is a small detector located at a forward angle, which is made up of two arrays of scintillator counters called V0A and V0C, as shown in Figure 27, which are arrays situated on both sides of the ALICE intersection point, in certain pseudo-rapidity ranges $2.8 \leq \eta \leq 5.1$ and

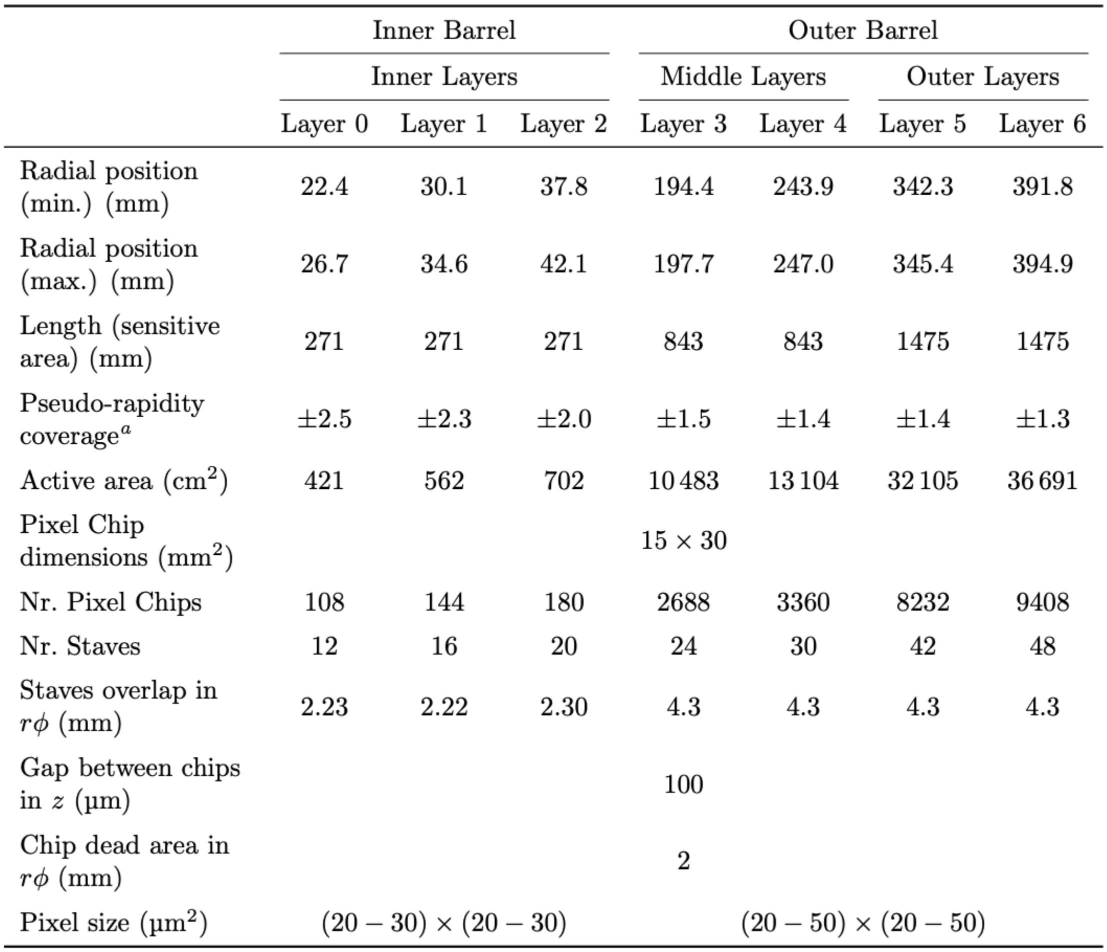

	Inner Barrel			Outer Barrel			
	Inner Layers			Middle Layers		Outer Layers	
	Layer 0	Layer 1	Layer 2	Layer 3	Layer 4	Layer 5	Layer 6
Radial position (min.) (mm)	22.4	30.1	37.8	194.4	243.9	342.3	391.8
Radial position (max.) (mm)	26.7	34.6	42.1	197.7	247.0	345.4	394.9
Length (sensitive area) (mm)	271	271	271	843	843	1475	1475
Pseudo-rapidity coverage[a]	±2.5	±2.3	±2.0	±1.5	±1.4	±1.4	±1.3
Active area (cm^2)	421	562	702	10 483	13 104	32 105	36 691
Pixel Chip dimensions (mm^2)				15×30			
Nr. Pixel Chips	108	144	180	2688	3360	8232	9408
Nr. Staves	12	16	20	24	30	42	48
Staves overlap in $r\phi$ (mm)	2.23	2.22	2.30	4.3	4.3	4.3	4.3
Gap between chips in z (µm)				100			
Chip dead area in $r\phi$ (mm)				2			
Pixel size ($\mu\mathrm{m}^2$)	$(20-30) \times (20-30)$			$(20-50) \times (20-50)$			

Figure 26: Geometrical parameters of the upgraded ITS [76].

$-3.7 \leq \eta \leq -1.7$ respectively [66].

The main objective of the V0 detector is to provide minimum-bias triggers for the central-barrel detectors in p-p and A-A collisions. These triggers are activated by particles originating from the initial collisions and from secondary interactions in the vacuum chamber elements. As the correlation between the number of registered particles on the V0 arrays and the number of primary emitted particles is linear, the V0 serves as an indicator of the centrality of a Pb − Pb collision via the multiplicity recorded in the event. The purpose of these triggers is to sort events based on certain criteria that they are designed to detect during the experiment. The minimum bias (MB) trigger is the most basic type of trigger, as an event is classified as part of the minimum

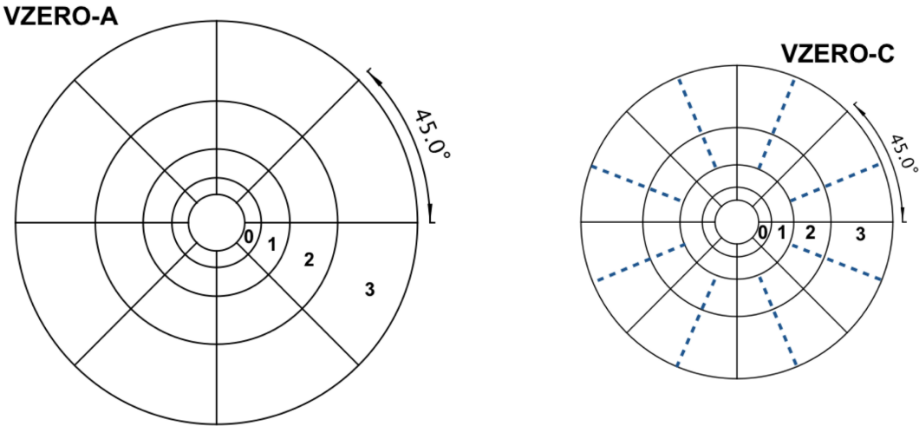

Figure 27: The VZERO sensors, consisting of V0-A and V0-C on either side of ITS [67].

bias data set if it generates a signal in the V0A or V0C detectors. As a result of these triggers, it is feasible to identify whether a collision took place or whether the signal observed in the detectors originated from interactions between the beam and the gas. Additional triggers utilized for $\mathrm{Pb}-\mathrm{Pb}$ data comprise those that mandate a signal surpassing a particular threshold in the V0 detector to document favorable central collisions. The central trigger (kCent) pertains to events with centrality ranging from 0-10 percent, the semi-central trigger (kSemiCent) pertains to events with centrality ranging from 30-50 percent, and the minimum bias trigger (kINT7) pertains to events with centrality ranging from 0-90 percent.

3.3 The ALICE Analysis Train System

The ALICE collaboration stores approximately 10 PBs of data annually across various storage elements worldwide. To analyze a single dataset, around 105 files, each containing approximately 50 TB of data, must be read. The ALICE analysis framework can create and submit analysis jobs to the Grid, which can then be monitored and resubmitted using the MonALISA monitoring service. The LEGO train system was developed on top of these existing frameworks to improve CPU efficiency and enable more user analysis with the same amount of computing resources. This is achieved by collecting multiple analysis tasks that analyze the same dataset and running them within the same analysis job, which reads the data once and uses it for multiple analysis tasks. By doing so, the data is not read repeatedly for each analysis task, resulting in higher CPU efficiency and faster processing time. Additionally, the LEGO trains hide the complexity of the Grid from users, allowing them to define their code on a web page and providing the analysis results as soon as they become available. The system is fully automated, and the jobs running on the Grid do not require supervision [61]. Improvements are continuously implemented in the computing process to utilize available resources more efficiently [60]. The train system is divided into several trains based on physics working groups such as jet analysis, particle correlations, etc., and different types of datasets such as p-p, p-Pb, or Pb-Pb collisions, as well as data or Monte Carlo simulations. Analyzing a dataset using a train is referred to as a train run. After working as a train operator for over two years, part of my responsibilities was testing and running trains. To run on a train, a user must first submit their analysis code to a repository. The code configuration is then defined on a web page in a train wagon. Train operators manage the trains by defining the datasets and configuring the train runs' jobs. The trains are started on a regular basis, usually once per day, by an operator who composes a train run from a set of wagons and a dataset. The train run undergoes an automated testing procedure, and only if the test is successful can it start on the Grid. Figure 28 shows an example of a train test. The Baseline tests the train configuration and does not contain any user code, while the Full train contains all train wagons. Each wagon is individually tested in between. The test provides various measurements, including the status (OK or Failed) and memory consumption, which is divided into total consumption and growth per event. The growth per event indicates a memory leak, and the number is highlighted in red if one is suspected. The timing information shows the time used per event, providing a rough estimate of the train duration. The last column reports the result of the merging test.

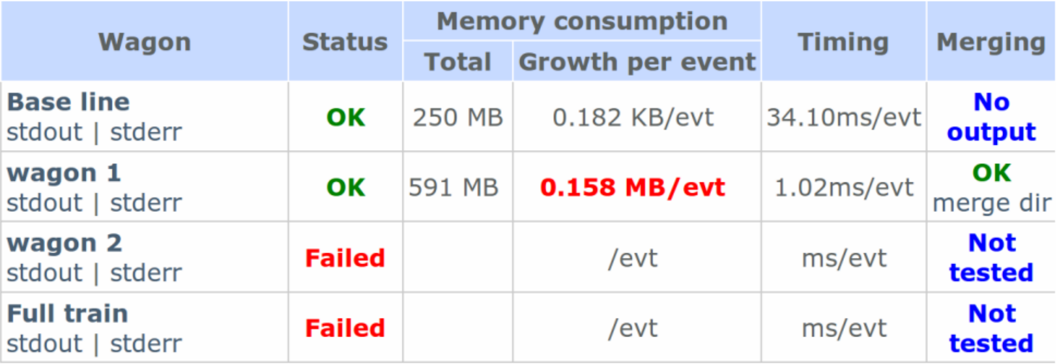

Wagon	Status	Memory consumption		Timing	Merging
		Total	Growth per event		
Base line stdout | stderr	**OK**	250 MB	0.182 KB/evt	34.10ms/evt	**No output**
wagon 1 stdout | stderr	**OK**	591 MB	**0.158 MB/evt**	1.02ms/evt	**OK** merge dir
wagon 2 stdout | stderr	**Failed**		/evt	ms/evt	**Not tested**
Full train stdout | stderr	**Failed**		/evt	ms/evt	**Not tested**

Figure 28: Representation of an example test before train run [61].

4 Determining the Speed of Sound from Experimental data

Finding the temperature reached in heavy-ion collisions has been an open challenge for decades, as well as other thermodynamic quantities such as entropy. In recent endeavors that have been published in Nature Physics [73], using hydrodynamic simulations, the authors obtained the so-called effective temperature, which is the temperature averaged over the spacetime evolution of the medium. In order to understand the idea, consider a uniform gas at rest that has volume V in a vacuum. At the time $t = 0$, the gas starts to expand freely. If the interactions between particles are sufficiently strong, the expansion will be governed by ideal hydrodynamics, and the total energy and entropy of the system will be conserved. Since the initial volume is known, by measuring the final state variables like the total number of particles and the average energy per particle, the thermodynamics of the initial state can be reconstructed without having any information about the hydrodynamic expansion. In order to apply this idea in the QGP expansion, one can define an effective volume, which is a volume of the QGP at rest that has the same energy and entropy produced in the collision. In order to formulate this idea, the effective temperature T_{eff} , and the effective volume V_{eff} , those of a uniform fluid at rest which would have the same energy and entropy as the fluid at freeze-out, are shown by these equations [73]:

$$\begin{aligned} E &= \int_{\text{f.o.}} T^{0\mu} \mathrm{d}\sigma_\mu = \epsilon\left(T_{\text{eff}}\right) V_{\text{eff}} \\ S &= \int_{\text{f.o.}} s u^\mu \mathrm{d}\sigma_\mu = s\left(T_{\text{eff}}\right) V_{\text{eff}} \,. \end{aligned} \tag{20}$$

The integral is taken over the freeze-out hypersurface, with $\mathrm{d}\sigma_\mu$ representing the elementary hypersurface element. The first line of the stress-energy tensor of the fluid is denoted as $T^{0\mu}$, where u^μ represents the fluid's 4-velocity. The energy and entropy density in the fluid rest frame is denoted as ϵ and s, respectively. By using the ratio E/S, one can solve for T_{eff} in the resulting equation while eliminating V_{eff} and using the same equation of state as in the hydrodynamic calculation. It is important to note that the equation of state of the fluid constrains the relationship between T_{eff} and $s\left(T_{\text{eff}}\right)$. The effective temperature is lower than the initial temperature due to longitudinal cooling but higher than the freeze-out temperature because the kinetic energy from the collective motion of the fluid is included in the energy E defined by Equation (20).

In an ideal gas with Boltzmann statistics, the energy per particle is equal to three times the temperature. The Boltzmann constant and the speed of light in vacuum are set to unity in natural units, making momentum and temperature have the same dimension. At high energy and near midrapidity, the transverse momentum of a particle is expected to be approximately equal to three times the effective temperature $\langle p_{\mathrm{T}} \rangle \approx 3T_{\text{eff}}$. To test this expectation, hydrodynamic simulations of Pb +Pb collisions were carried out. Three sets of calculations were performed using ideal hydrodynamics, viscous hydrodynamics with only shear viscosity, and viscous hydrodynamics with only bulk viscosity [73] since the transport coefficients of the quark-gluon plasma are not well constrained. Using empirical evidence, they ascertain the temperature, entropy density, and speed of sound in the material formed during lead-lead collisions at the Large Hadron Collider. As one can observe in Figures 29 and 30, the relation between the effective temperature T_{eff} the effective volume $V_{\text{eff.}}$ and the multiplicity of charged particles is shown.

Results are presented as a function of the collision energy for a fixed centrality range (5 percent of most central collisions). They finally obtain the speed of sound by using two collision energies using 0–5 percent centrality in Pb–Pb collisions. In a fixed central interval, the volume is fixed as

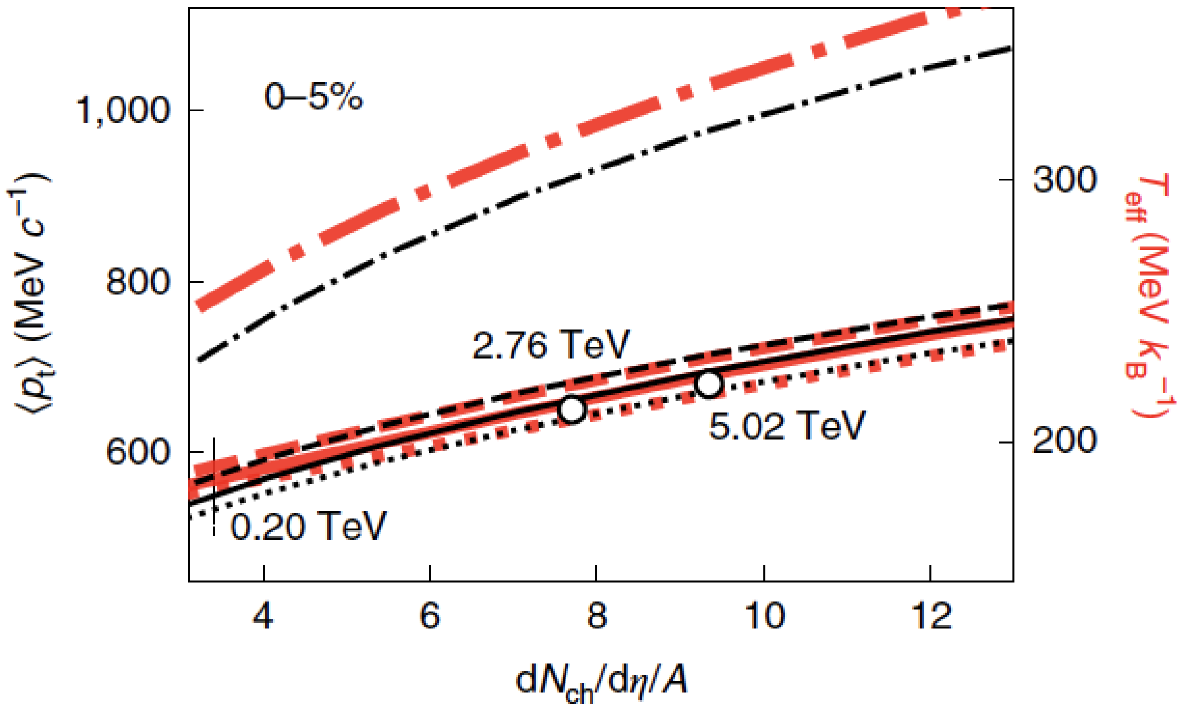

Figure 29: Representaion of hydrodynamic simulations of Pb + Pb collisions. Black curves correspond to the average transverse momentum, $\langle p_t \rangle$, red curves to the effective temperature, T_{eff} [73].

one increases the energy pressure and the temperature increase which yields compressibility. The latter is related to the speed of sound, which is (see Figure 31):

$$c_{\mathrm{s}}^2\left(T_{\text{eff}}\right)=0.24 \pm 0.04. \tag{21}$$

Two methods are used in this dissertation to calculate the speed of sound experimentally. One by the definition of the speed of sound in the relativistic limit and one by an analytical method. The idea is that ultra-central collisions (defined, for instance, as the 0.1 percent most central collisions) produce a quark-gluon plasma that always has the same volume as one can see in Figure 30. In a relativistic fluid, the square of the speed of sound is defined as the change in pressure when the energy density changes:

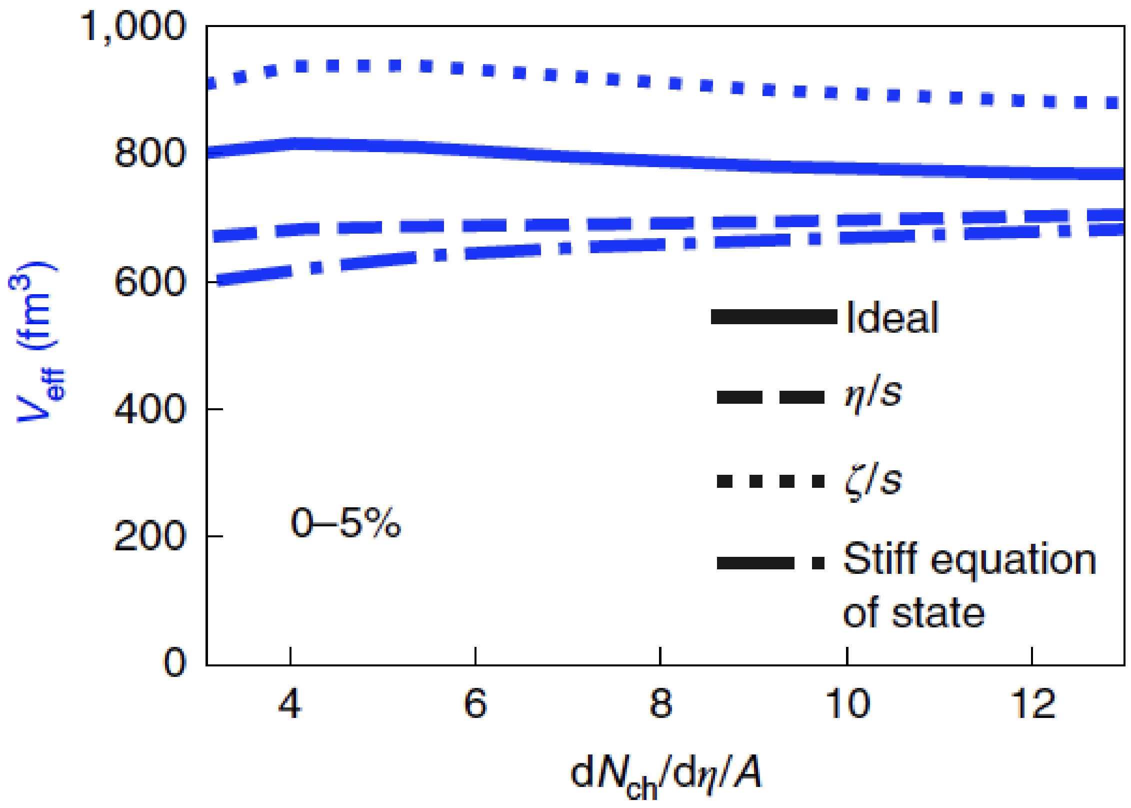

Figure 30: Representaion of hydrodynamic simulations of Pb + Pb collisions. The plot shows the relation between effective volume, V_{eff}, and the multiplicity of charged particles [73].

$$c_s^2 = \frac{dP}{d\epsilon} \tag{22}$$

then by using thermodynamics relations:

$$d\varepsilon = Tds, \quad dP = sdT \tag{23}$$

and by substituting these relations in Equation (22), one can get:

$$c_s^2 = \frac{dP}{d\varepsilon} = \frac{s}{T}\frac{dT}{ds}, \tag{24}$$

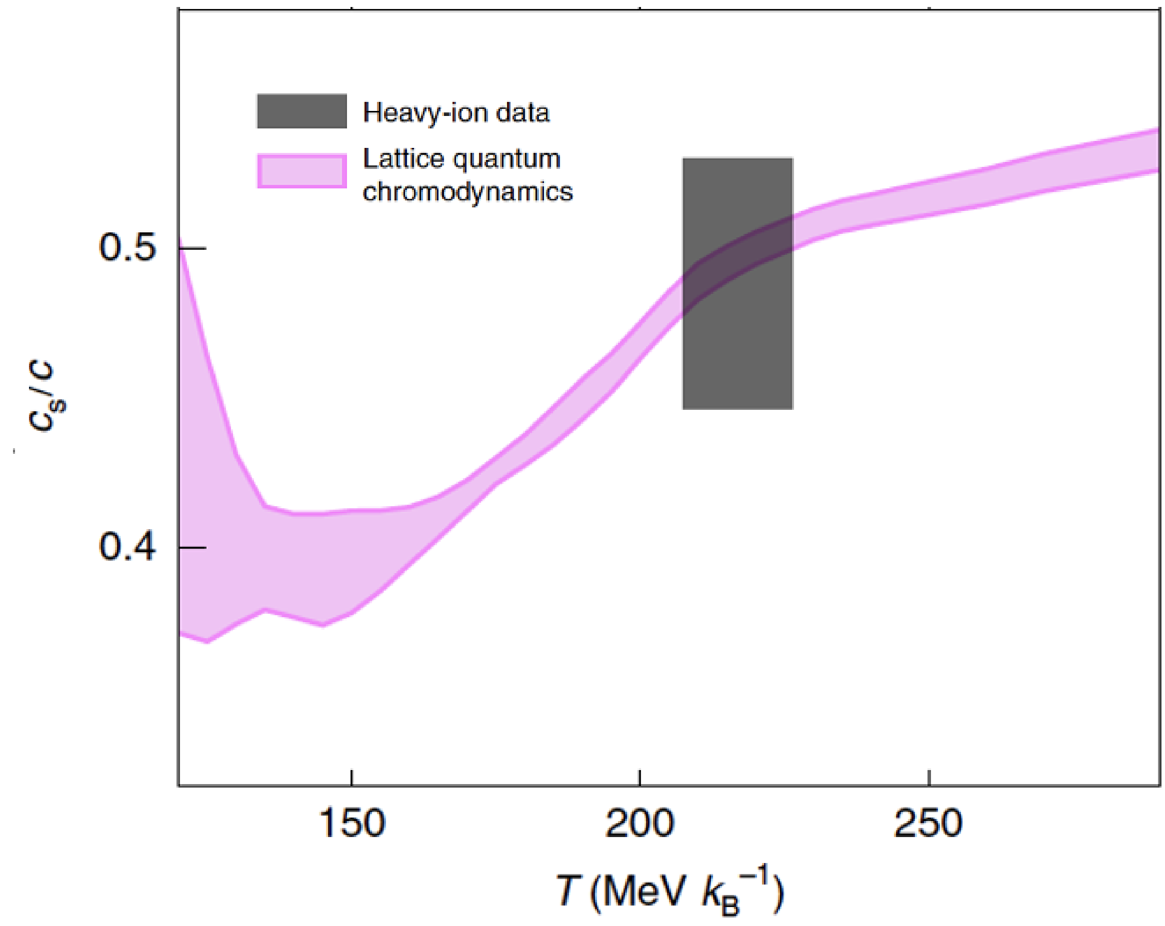

Figure 31: Speed of sound as a function of the temperature. Magenta bands are obtained by ab initio calculations using LQCD, and the Grey box represents the result from heavy-ion experimental data [73].

using the relations:

$$\frac{dT}{T} = d\ln T, \quad \frac{ds}{s} = d\ln s, \tag{25}$$

one gets:

$$c_s^2 = \frac{dP}{d\epsilon} = \frac{d\ln T}{d\ln s}. \tag{26}$$

.

The effective volume is essentially constant as a function of the energy so that the effective entropy density is proportional to the multiplicity. Analogously, the effective temperature is proportional to $\langle p_{\mathrm{T}} \rangle$. This implies:

$$\frac{\mathrm{d}s\left(T_{\mathrm{eff}}\right)}{s\left(T_{\mathrm{eff}}\right)}=\frac{\mathrm{d}N_{\mathrm{ch}}}{N_{\mathrm{ch}}}, \quad \frac{\mathrm{d}T_{\mathrm{eff}}}{T_{\mathrm{eff}}}=\frac{\mathrm{d}\left\langle p_{\mathrm{T}}\right\rangle}{\left\langle p_{\mathrm{T}}\right\rangle} \tag{27}$$

then the equation for the speed of sound becomes:

$$c_{\mathrm{s}}^{2}\left(T_{\mathrm{eff}}\right) \equiv \frac{\mathrm{d}P}{\mathrm{d}\varepsilon}=\left.\frac{s\ \mathrm{d}T}{T\ \mathrm{d}s}\right|_{T_{\mathrm{eff}}}=\frac{\mathrm{d}\ln\left\langle p_{\mathrm{T}}\right\rangle}{\mathrm{dln}\left(\mathrm{d}N_{\mathrm{ch}}/\mathrm{d}\eta\right)} \tag{28}$$

where P, ϵ, T, and s represent the pressure, energy density, temperature, and entropy density, respectively. p_{T} is the proxy for temperature, and N_{ch} is the proxy for entropy.

The second method is an analytical method developed by a simple assumption that the probability distribution of S at a fixed impact parameter b is a Gaussian [72]. As mentioned before, the original meaning of centrality was based on impact parameter classification. However, in current experiments, it is defined by collision classification using the parameter n. To avoid confusion, the term b-centrality is used when referring to centrality determined based on impact parameters. The relationship between n and b can be established following a Gaussian distribution. This Gaussian distribution is characterized by a mean $\bar{n}$ and width σ, both of which depend on the impact parameter [72]:

$$P\left(n \mid c_{b}\right)=\frac{\eta\left(c_{b}\right)}{\sigma\left(c_{b}\right)\sqrt{2\pi}} \exp\left(-\frac{\left(n-\bar{n}\left(c_{b}\right)\right)^{2}}{2\sigma\left(c_{b}\right)^{2}}\right). \tag{29}$$

Due to the central limit theorem, it is anticipated that this will be a good estimate for a large system. The parameter n comprises contributions from numerous collision processes located at distinct points in the transverse plane, making them causally disconnected and independent. In order to normalize the Gaussian to unity, one can perform:

$$\eta\left(c_{b}\right)=2\left[1+\operatorname{erf}\left(\frac{\bar{n}\left(c_{b}\right)}{\sigma\left(c_{b}\right)\sqrt{2}}\right)\right]^{-1}. \tag{30}$$

Testing the Gaussian approximation on a model is a practical approach. Within the hydrodynamic framework, the final-state observables that establish collision centralities, such as transverse energy or multiplicity, are proportional to the initial entropy of the system. The initial entropy represents the experimental parameter n and is determined by models of initial conditions, such as TRENTo. Figures 32 and 33 demonstrate some checks [72] on this approximation for $\mathrm{Pb}+\mathrm{Pb}$ collisions at ($\sqrt{s_{NN}}=2.76$ TeV utilizing the TRENTo model, which has been described before.

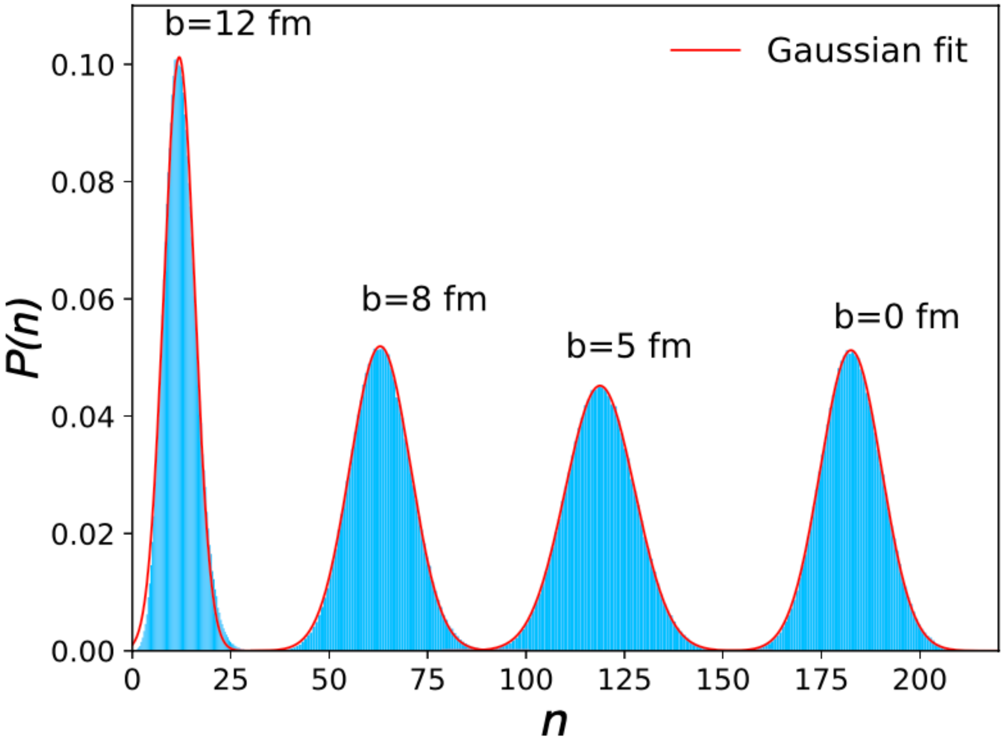

Figure 32: The shaded regions are the probability distribution of the variable n for a fixed impact parameter. The values of impact parameter used were $0, 5, 8$, and 12 fm , corresponding to collision centrality percentages of $0\%, 10\%, 26\%$, and 58%, respectively. The number of events for each impact parameter is $5 \times 10^{\wedge}5$. The solid lines are Gaussian fits on data. [72]

By integrating over c_b in Equation (29), basically the final state observable will be obtained:

$$P(n)=\int_0^1 P\left(n \mid c_b\right) d c_b \tag{31}$$

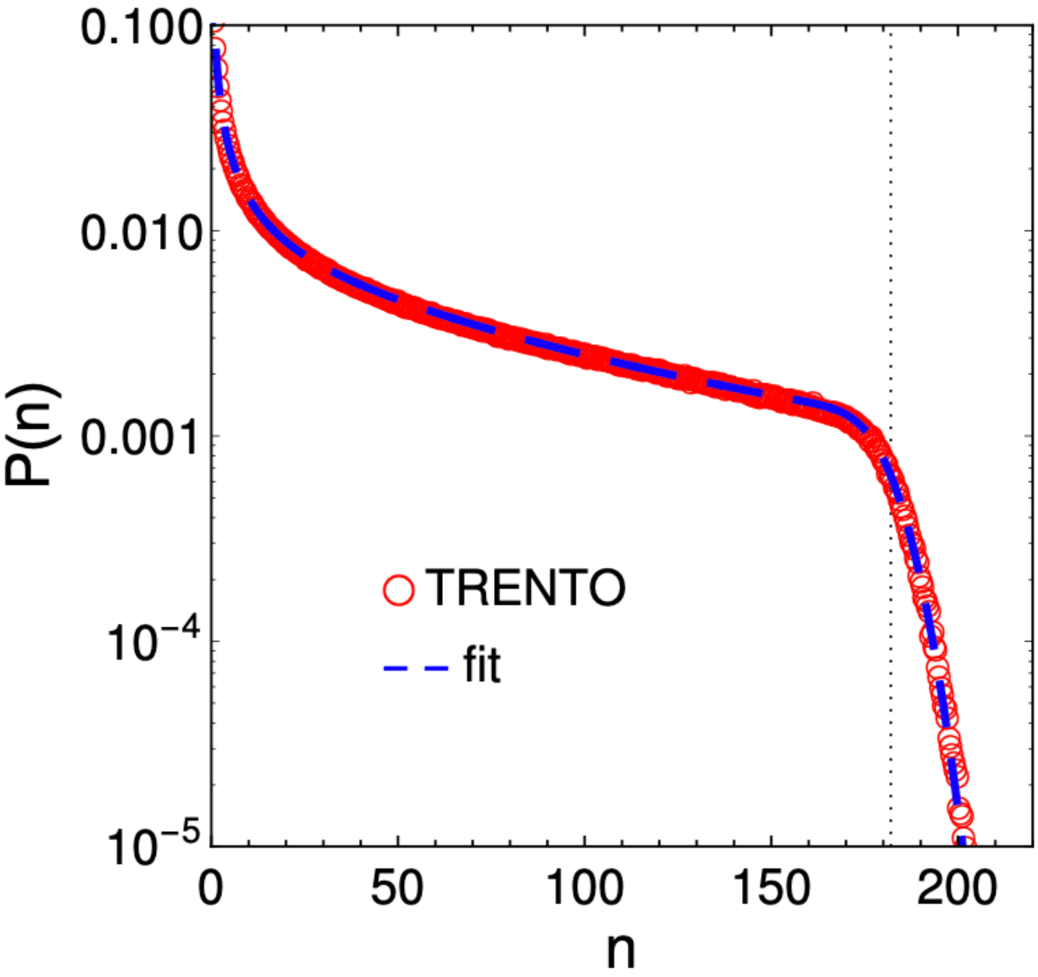

Figure 33: Final observable distribution with Gaussian fit [72].

In order to fit Equation (31) on data, a smooth function of $\bar{n}\left(c_b\right)$ is needed, which should be positive and monotonically decreasing as a function of c_b and that can be [72]:

$$\bar{n}\left(c_b\right) = n_{\text{knee}}\ \exp\left(-a_1 c_b - a_2 c_b^2 - a_3 c_b^3\right) \tag{32}$$

which is a five-parameter fit function to fit on $P(n)$, using Equations (29), (30) and (31).

Using Equation (29), and considering that one of the final observables (n), can be entropy S, one can write:

$$P(S \mid b) = \frac{1}{\sigma\sqrt{2\pi}} \exp\left(-\frac{(S-\bar{S}(b))^2}{2\sigma^2}\right). \tag{33}$$

By integrating over the impact parameter, the distribution of entropy S can be derived (note that the knee is defined as the mean value of S at zero impact parameter $S_{\text{knee}} \equiv \bar{S}(0)$ and the change of variable is $b \to \bar{S}(b)$) [71]:

$$P(S \mid \bar{S}) = \frac{1}{\sigma\sqrt{2\pi}} \exp\left(-\frac{(S-\bar{S})^2}{2\sigma^2}\right). \tag{34}$$

By integrating over $\bar{S}$ and assuming that the probability distribution of $\bar{S}$, $P(\bar{S})$ is constant:

$$\begin{aligned} P(S) &= \int_0^{S_{\text{knee}}} P(S \mid \bar{S})P(\bar{S})d\bar{S} \\ &\propto \int_0^{S_{\text{knee}}} P(S \mid \bar{S})d\bar{S} \\ &\propto \operatorname{erfc}\left(\frac{S-S_{\text{knee}}}{\sigma\sqrt{2}}\right). \end{aligned} \tag{35}$$

The dashed line in Figure 34 (a), is a representation of this model in which the parameters S_{knee} and σ have been calculated by using TRENTo model. The next assumption is that the initial radius R is solely dependent on the impact parameter, or in other words, on the parameter $\bar{S}$ [71]. Using Bayes' theorem, the distribution of $\bar{S}$ can be determined at fixed entropy, and following that, R can be determined for fixed S.

$$P(\bar{S} \mid S) = \frac{P(S \mid \bar{S})P(\bar{S})}{P(S)}. \tag{36}$$

Integrating the above equation gives:

$$\langle \bar{S} \mid S \rangle = S - \sigma\sqrt{\frac{2}{\pi}} \frac{\exp\left(-\frac{(S-S_{\text{knee}})^2}{2\sigma^2}\right)}{\operatorname{erfc}\left(\frac{S-S_{\text{knee}}}{\sqrt{2}\sigma}\right)}. \tag{37}$$

For $S < S_{\text{knee}}$, the second term on the right-hand side can be ignored, and the inner product $\langle \bar{S} \mid S \rangle$ is approximately equal to S, indicating that fluctuations are averaged out [84]. On the

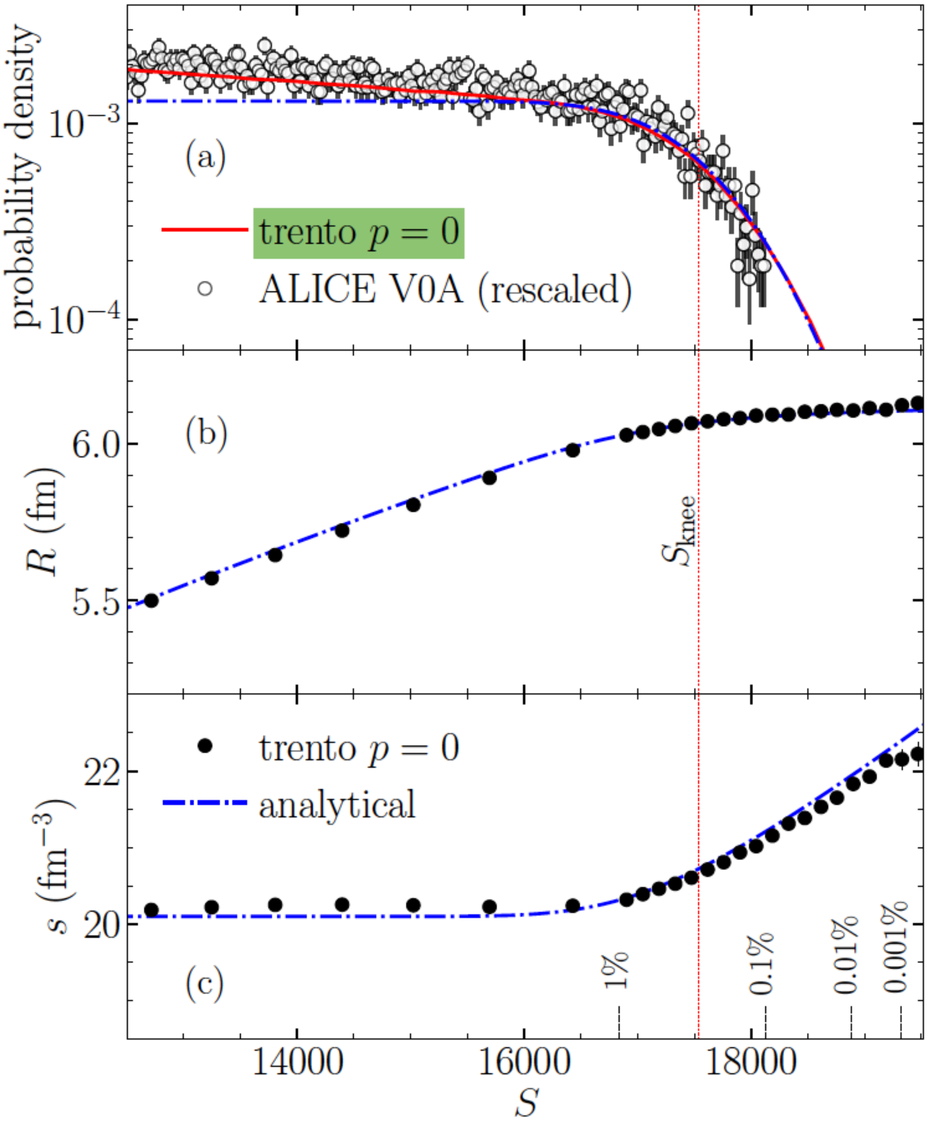

Figure 34: This Figure displays the outcomes of the TRENTo model utilizing initial conditions with $p = 0$ and $k = 2.0$, using 20 million Pb + Pb collisions at ($\sqrt{s_{\mathrm{NN}}} = 5.02$ TeV. Only the top 10% of events with the highest values of the total entropy per unit rapidity (S), corresponding to $0 - 10\%$ centrality, were considered. The probability distribution of S and the V0 amplitude (used by ALICE to determine centrality) are shown in panel (a). The initial radius (R) and effective entropy density (s) are presented in panels (b) and (c), respectively. The dots and dashed lines represent the averaged results of the TRENTo simulation, while the dot-dashed lines indicate one-parameter fits employing Eqs. (35), (38), and (39). The knee's position and the specific values of the centrality percentile are highlighted with vertical lines [71].

right-hand side of the knee, $\bar{S}$ saturates at its maximum value: $\langle \bar{S} \mid S \rangle \simeq S_{\text{knee}}$. According to the TRENTo calculation, which shows that the entropy density remains constant to the left of the knee, it is assumed that the volume is proportional to $\bar{S}$. Based on this assumption, the radius R can be expressed as follows:

$$R = R_0 \left(\frac{\langle \bar{S} \mid S \rangle}{S_{\text{knee}}} \right)^{1/3}, \tag{38}$$

where the entropy density s is given by:

$$s = s_0 \frac{S}{\langle \bar{S} \mid S \rangle}. \tag{39}$$

These equations have two fit parameters, R_0 and s_0, which represent the value of R to the right of the knee and the value of s to the left of the knee, respectively. Figure 34, panels (b) and (c), demonstrate the initial radius R, and effective entropy density s, both averaged over events, respectively.

Now the crucial aspect is determining how to extract the parameters using data through this analytical approach. To obtain the values for S_{knee} and σ, one can replace the variable S with the number of charged particles N_{ch} and analyze its distribution. This can be achieved through either the straightforward Bayesian method outlined in Reference [13] or by fitting a model such as the Glauber model to the experimental histogram and computing the values for S_{knee} and σ within the model. In this study, the methodology outlined in Reference [72], is used for the analysis of ALICE data:

$$\langle p_{\text{T}} \rangle = p_{\text{T}0} \left(\frac{S}{\langle \bar{S} \mid S \rangle} \right)^{c_s^2}. \tag{40}$$

The expression $\langle p_T \rangle$ refers to the average transverse momentum left of the knee and its initial value is denoted as p_{t0}. The conditional average $\langle \bar{S} \mid S \rangle$ is determined by the Equation (37). In this study, the value of p_{t0} is taken as 682 MeV, which was measured by ALICE for collisions in the

0-5 percent centrality range [74] and corresponds to an effective temperature of $T_{\text{eff}} = 222$ MeV, which is predicted by lattice QCD to have a squared speed of sound of $c_s^2 = 0.252$.

5 Analysis Details

5.1 Analysis Software, ROOT Framework

The analysis in this dissertation utilizes the ROOT [46] software package, which is a widely used software package developed at CERN for data analysis in numerous high-energy physics experiments. This software framework is implemented in the C++ programming language and is appropriate for analyzing experimental high-energy physics data. ROOT provides an integrated I/O, an efficient hierarchical object stored with a complete set of object containers, and a C++ interpreter. Additionally, the ALICE offline framework, AliRoot, is constructed on top of ROOT and offers a comprehensive range of features required for event generation, detector simulation, event reconstruction, data acquisition, and data analysis.

5.2 Track Reconstruction

This analysis studies charged particle multiplicity distributions and multiplicity-dependent transverse momentum spectra for Pb-Pb and Xe-Xe collisions at $\sqrt{s_{NN}} = 5.02$ TeV, $\sqrt{s_{NN}} = 5.44$ TeV collision energies, respectively. The TPC detector is responsible for track reconstruction and particle identification, while the ITS is used to improve the resolution of spatial and momentum measurements, as mentioned in Section 3.2. This helps to eliminate the background from secondary tracks, which may arise from weak decays, conversions, secondary hadronic interactions in the detector material, and pile-up. Pileup events occur when multiple interactions take place within the same bunch crossing. The TPC data collected during the 2018 $\mathrm{Pb-Pb}$ run has pileup. The process of reconstructing charged tracks using the ALICE software involves several stages. It commences by identifying the primary vertex through clusters detected in the two SPD layers. Subsequently, the clusters detected in the central barrel are integrated to form tracks that account for the curvature caused by the magnetic field and energy loss using a helix approximation. After this, the Kalman filtering technique is utilized to fit these spatial points and generate track candidates for reconstructing the kinematics of particles. These spatial points are created by the clusters of charged particles in the TPC tracking device. The process of finding and fitting tracks starts from the outermost pad rows of the TPC, where the tracks are widely spaced apart. The fitting process then progressively moves inward towards the ITS, where the tracks are closer together. Next, the track candidates are assigned to different clusters using the Kalman filter in the ITS data to improve the estimation of track parameters such as momentum. After this assignment, the ITS stand-alone tracking procedure is carried out using the remaining clusters to recover any tracks that might have been lost in the TPC due to factors like crossing a dead zone, decays, or the momentum cut-off. Once all the ITS clusters are added to the tracks, the procedure is restarted from the inner ITS layer to the outer TPC boundary. In this step, any improperly assigned clusters are eliminated to enhance the track quality. The process then extrapolates to the Time-of-Flight (TOF), Transition Radiation Detector (TRD), Particle Identification (HMPID), and Photon Spectrometer (PHOS) detectors to obtain information that can be used to identify the particle species. In the final stage, the filter is once again reversed for a final refit of the track back towards the primary vertex to calculate the best track parameters at the vertex. Secondary tracks can be utilized to reconstruct decay vertices. These are the tracks that did not pass the final refit toward the primary vertex.

5.3 Event and Track Selection

The data analyzed in this thesis was collected during the Run 2 period at the LHC by the ALICE detector, which comprises various detectors as explained in the previous chapter. The analysis specifically utilizes tracks obtained from the TPC and ITS detectors. The data collected by the ALICE detectors is generally stored in the ALICE Grid in the form of Event Summary Data (ESD), which includes all the information from the raw data, such as primary vertex, tracking, secondary vertices, etc. However, since ESDs contain a vast amount of information, they occupy a considerable amount of memory. If all users from the ALICE collaboration were to utilize ESDs for their analysis, it would result in an enormous consumption of computer resources and time. To mitigate this issue, the concept of Analysis Object Data (AOD) was introduced in ALICE, which contains only relevant and lighter analysis-related information of an ESD, making it more manageable in terms of memory usage. During data taking at the LHC, the ALICE detectors capture information about the particles created during collisions that occur in a single beam crossing, which is referred to as an event. Often, one collision is more prominent in the detector than the others within an event. The uninterrupted recording of events is referred to as a run, and multiple runs are grouped together into periods that correspond to the duration of the LHC's operation. Additionally, the ALICE Data Preparation Group has generated MC data for each period, which includes ESDs and AODs.

The datasets used in this analysis are shown in Table 1. Heavy-ion events are selected within a primary vertex z range of $(-10 < V_z < 10)$ cm, which maximizes the acceptance of the TPC and ITS detectors. The event trigger selection is the minimum bias V0 trigger both for Xe-Xe and Pb-Pb collisions. One of the potential event backgrounds comes from multiple collision overlaps or pileups. Generally, there are two categories of pileup: Same-bunch-crossing pileup and Out-of bunch pileup [83]. Same-bunch-crossing pileup happens when two (or more) collisions occur in the same bunch-crossing, and it will be seen by all the detectors. In drift detectors (TPC and SDD), the estimation of track parameters is correct, the reconstructed points are in the "correct" spatial position, and the efficiency of prolongation from TPC to ITS is the same for the "main" and for the piled-up collision(s). This type of pileup can be removed at the event selection level with cuts based on multiple reconstructed vertices. Out-of-bunch pileup happens when one (or more) collisions occur in bunch crossings different from the one which triggered the acquisition. Depending on the readout time of the detectors, they get affected differently. Generally, readout times are relevant for the sensitivity of a given detector to out-of-bunch pileups. In drift detectors (TPC and SDD), the reconstructed points are spatially shifted along the drift direction (i.e., z for TPC).

Table 1: Datasets used in this dissertation

System	Type	$\sqrt{s_{\mathrm{NN}}}$ TeV	Period (or tag)
Xe-Xe	Raw	5.44	LHC17n-pass1
Xe-Xe	MC	5.44	LHC17j2-2 (HIJING)
Pb-Pb	Raw	5.02	LHC18r-pass3-AOD252
Pb-Pb	MC	5.02	LHC20e3a-AOD252 (HIJING)

Datasets used from Run 2 raw and Monte Carlo data for this analysis both for Xe-Xe and Pb-Pb.

This type of pileup can also be removed at the event selection level with cuts based on multiple reconstructed vertices, which work for collisions that occurred within the SPD readout time, and cuts based on correlations between the number of tracks/tracklets/amplitudes in different detectors, which can be used to remove events with out-of-bunch pileup outside the SPD readout time. In many of the Run 2 samples, a large fraction of the recorded events has more than one collision in the TPC readout time. Hence, tagging and removal of events with pileup, although possible, would result in a dramatic loss of statistics. Cleanup should therefore be based on track selection cuts, i.e., removing the tracks from the pileup collisions and keeping only the ones from the collision that fired the trigger. The Monte Carlo productions of the Run-2 data samples include the simulation of pileup to better match the TPC performance observed in the data. The pileup is simulated via the class AliGenPileup, which generates a number of collisions based on the average number of collisions per bunch crossing and the BC mask. Same bunch and out-of-bunch pileups are simulated, with the proper assignment of collision time based on the bunch crossing in which the collision occurs. To correctly treat the Monte Carlo information at the analysis level without getting a bias on the efficiencies, particles from out-of-bunch (OOB) pileup should be removed at generator level analysis. Same bunch crossing is very rare in Pb-Pb 2018 and is negligible for most analyses. ALICE employs a variety of techniques. One such technique is the use of high-speed readout electronics, which can quickly identify and reject signals that are not associated with the primary collision. Another technique is to use sophisticated event reconstruction algorithms that can separate the signals produced by the primary interaction from those produced by out-of-bunch pileups. Additionally, ALICE employs a trigger system that selects only the most interesting collisions based on certain criteria, such as the energy or type of particles produced in the collision. This helps to reduce the amount of data that must be processed, which in turn reduces the impact of the out-of-bunch pileup. Overall, mitigating the effects of out-of-bunch pileups is an important aspect of the data analysis process for the ALICE experiment and requires a combination of advanced technology and sophisticated algorithms.

After applying all event selections, including the standard ALICE method for pile-up rejection, totals of ~ 1.3 million Xe-Xe and ~ 23 million Pb-Pb events are used for this analysis. As this thesis analyzes soft probes of the QGP, charged particles were chosen for analysis within a specific range of transverse momentum, namely between 0.2 and 5 GeV/c, and pseudorapidity, specifically $|\eta| < 0.8$. It should be noted that the ALICE detector's ability to track particles significantly diminishes when the transverse momentum drops below 200MeV/c due to the magnetic field. Thus, such low-p_{T} tracks are not registered in the TPC. On the other hand, the upper limit of p_{T} was capped at 5 GeV/c in order to minimize any non-flow correlations that may arise from high energy jets. The chosen range of pseudorapidity was primarily based on the uniform acceptance of the TPC in this region. To be included in the analysis, the tracks needed to meet certain criteria. Specifically, they were required to have a minimum of 70 reconstructed space points out of a maximum of 159 in the TPC, as well as to have registered a hit in at least two of the six ITS layers. Tracks with a lower number of space points may be the result of split tracks, where one charged particle is mistakenly identified as two separate tracks.

6 Results

Figure 35 shows the reconstructed multiplicity distributions from Xe-Xe and Pb-Pb collisions. The term multiplicity refers to the event-wise number of charged tracks within η and p_{T} ranges of the track selections and is denoted by $N_{\mathrm{ch}}(|\eta < 0.8|)$. The distributions are normalized as probability density functions, such that they integrate to 1 over the full N_{ch} range. Figure 36 shows the mean transverse momentum $< p_{\mathrm{T}} >$ of charged tracks as a function of the multiplicity from Xe-Xe and Pb-Pb collisions. In Xe-Xe collisions, the $< p_{\mathrm{T}} >$ continuously rises after $N_{\mathrm{ch}} \sim 1400$, which corresponds to the ultra-central region of 0-1 percent centrality. For Pb-Pb, the continuous rise occurs after $N_{\mathrm{ch}} \sim 2300$, which also corresponds to 0-1 percent centrality. The rises in Xe-Xe and Pb-Pb imply Equation (28) can be used to extract the speed of sound squared from both systems. The procedure is referred to as **Method One**. In Figure 37, the natural logs of $< p_{\mathrm{T}} >$ and N_{ch} are shown. As the speed of sound squared is the derivative of this measurement, a first-order polynomial is fitted to the data, with a gradient and constants as free parameters. The fit quality is reasonable with the χ^2/DOF being below 2 in each case. The speed of sound squared values from the gradients for Xe-Xe and Pb-Pb are also shown in Figure 50.

Figures 38 and 39 investigate using Equation (40) to obtain the speed of sound squared, which is referred to as **Method Two**. The S parameters are obtained using the previous equations via fits to multiplicity distributions. The fit quality for the $< p_{\mathrm{T}} >$ vs. N_{ch} data is also reasonable, with similar χ^2/DOF values as method one. Table 2 summarizes the squared values of the speed of sound from both methods in each collision system. Subsequent sub-sections will discuss methods employed for correcting the data for reconstruction efficiency, which will be followed by the presentation of results pertaining to the squared speed of sound, derived from the corrected data.

Table 2: Speed of sound values before corrections

System	$\sqrt{s_{\mathrm{NN}}}$[TeV]	Method One	Method Two
Xe-Xe	5.44	$c_s^2 = 0.071 \pm 0.008$	$c_s^2 = 0.085 \pm 0.0072$
Pb-Pb	5.02	$c_s^2 = 0.085 \pm 0.002$	$c_s^2 = 0.095 \pm 0.0018$

The values of the speed of sound squared for every collision system and method utilized before the corrections.

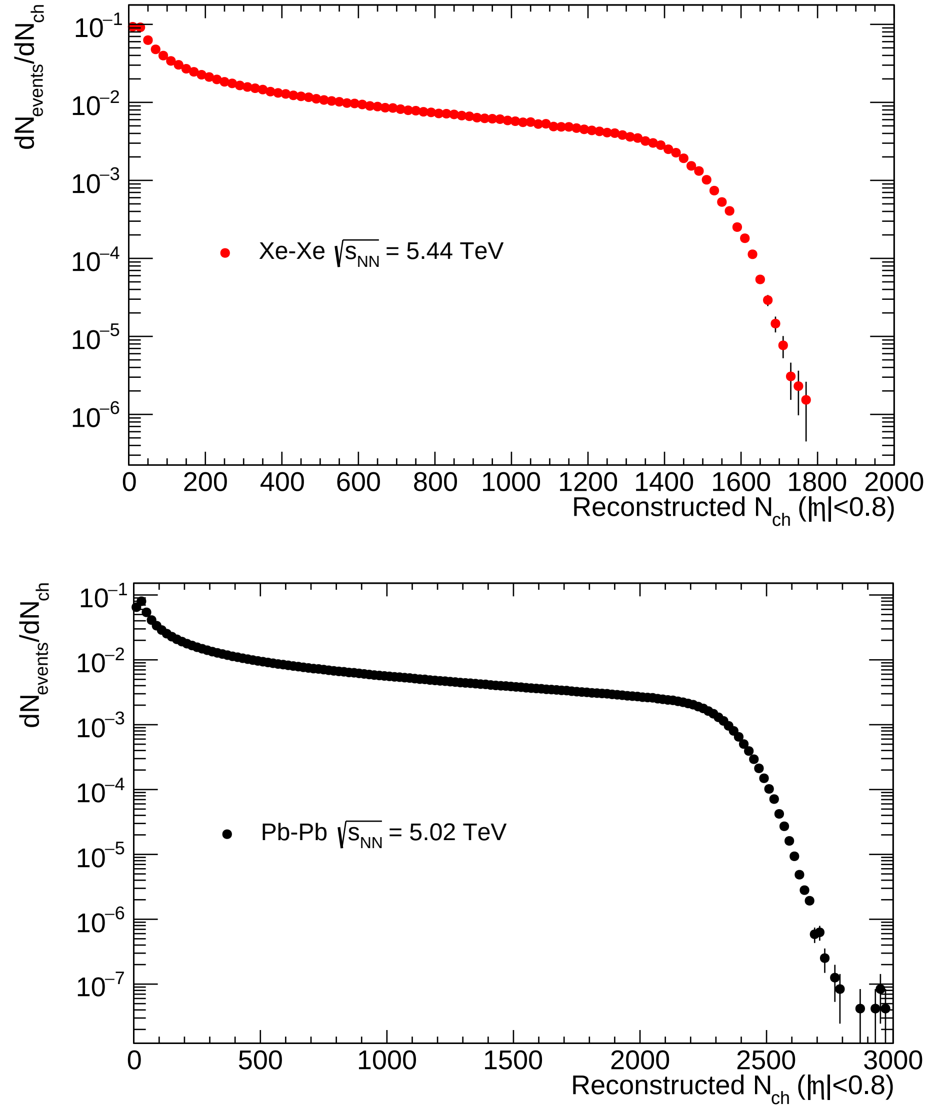

Figure 35: Reconstructed multiplicity distributions from heavy-ion collisions in ALICE. The uncertainties shown are statistical.

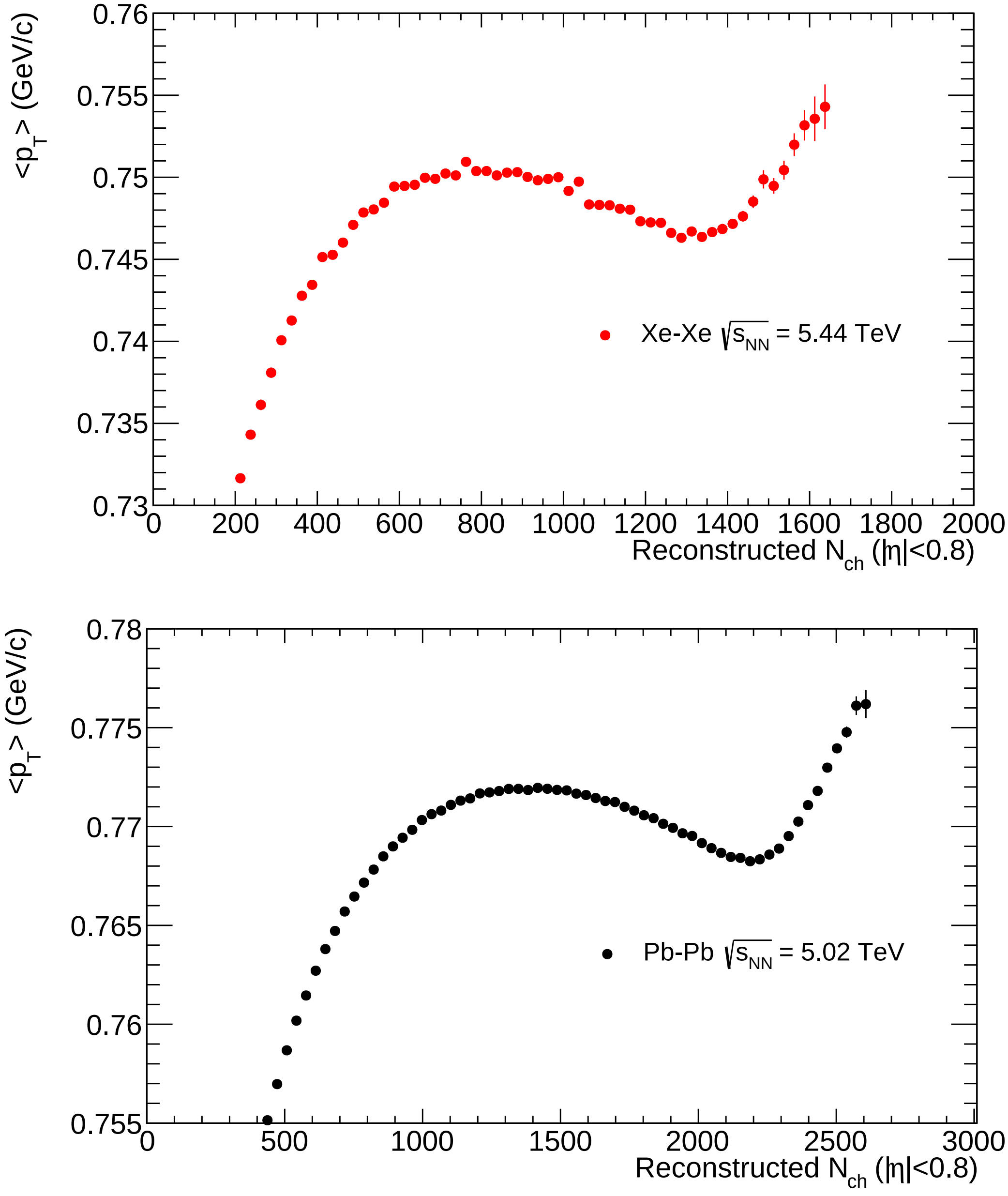

Figure 36: Averaged transverse momentum versus Multiplicity distributions from heavy-ion collisions. The uncertainties shown are statistical.

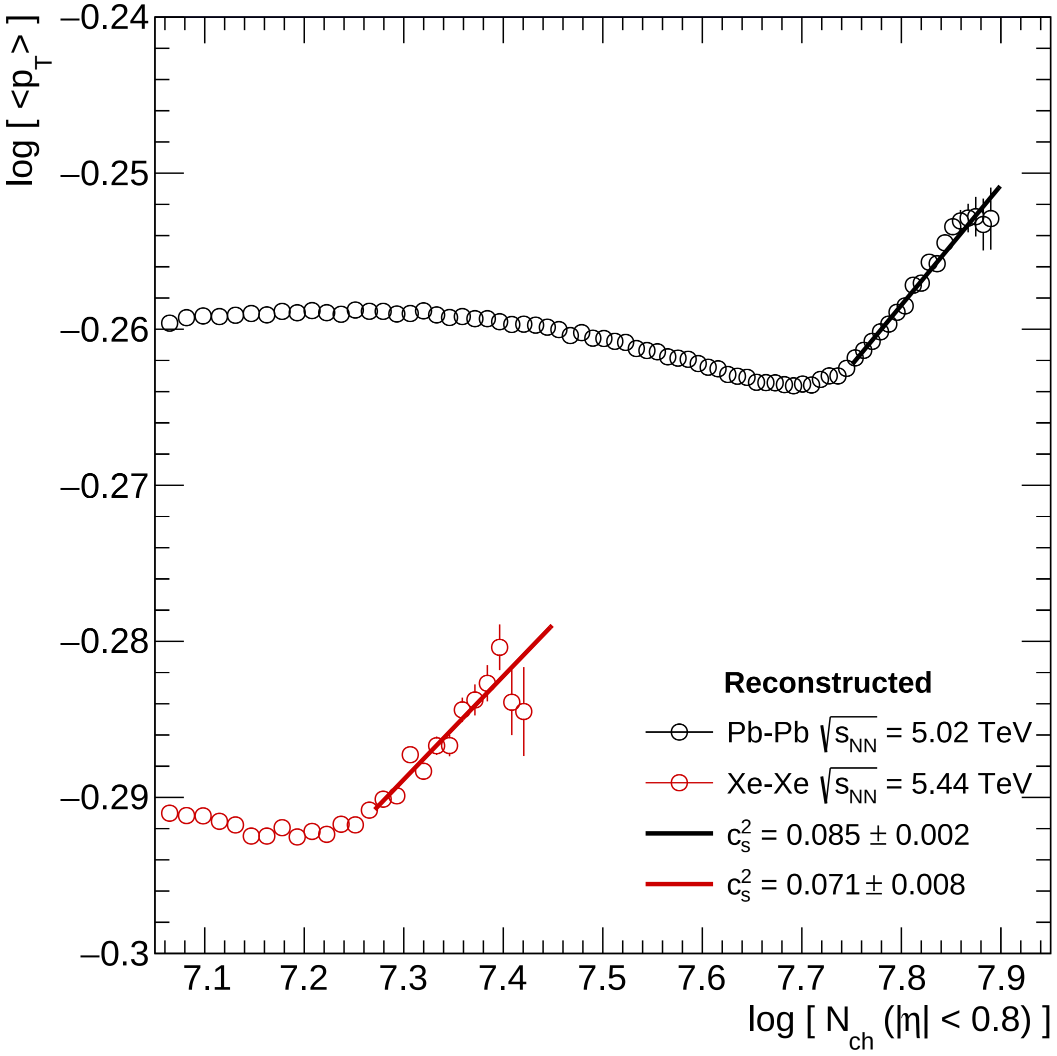

Figure 37: Fit results on data obtained from heavy-ion collisions before corrections and c_s^2 calculations using method one. The uncertainties shown for the data are statistical.

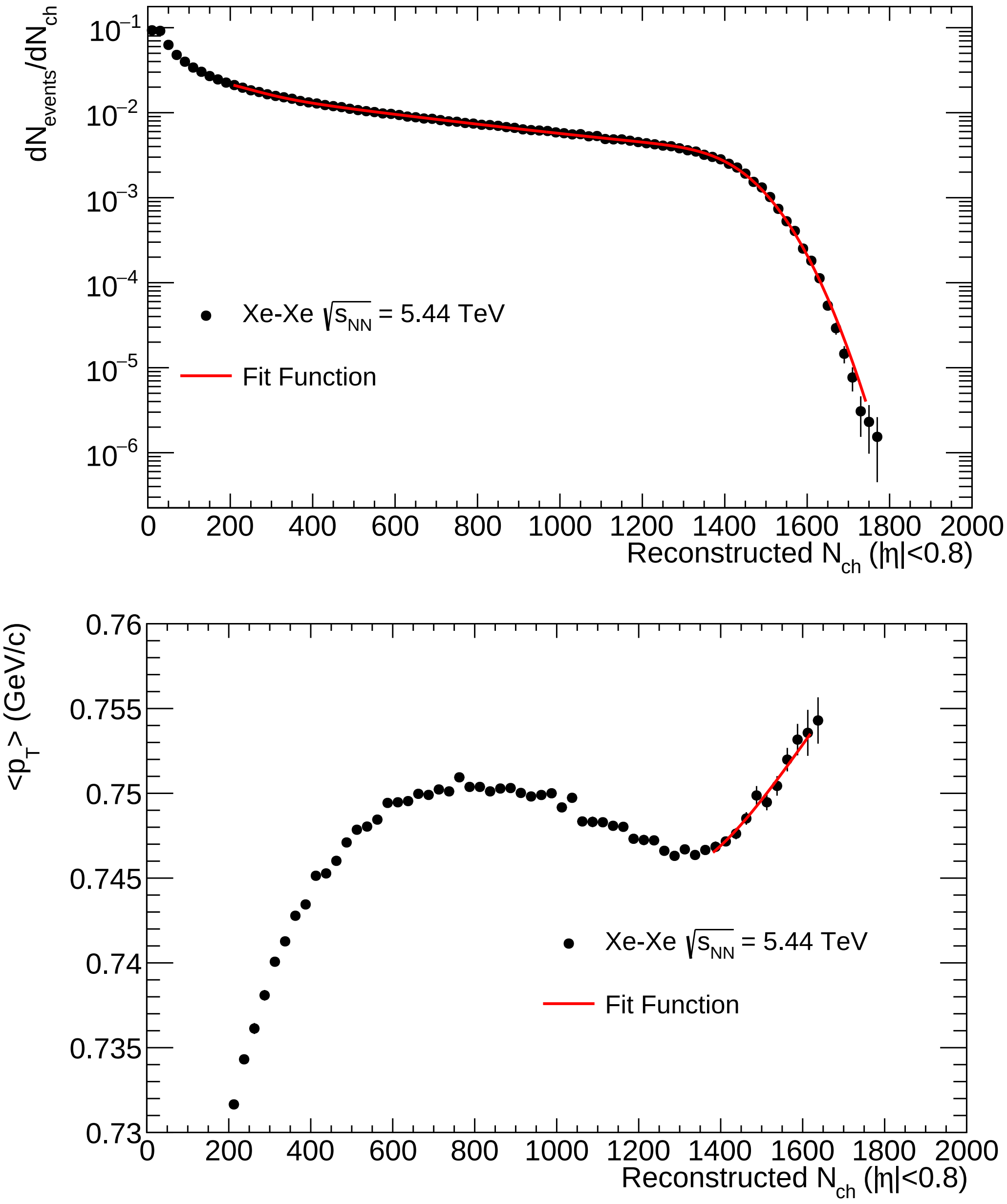

Figure 38: Fit results on data obtained from Xe-Xe collisions before corrections and c_s^2 calculations using method two. The uncertainties shown for the data are statistical.

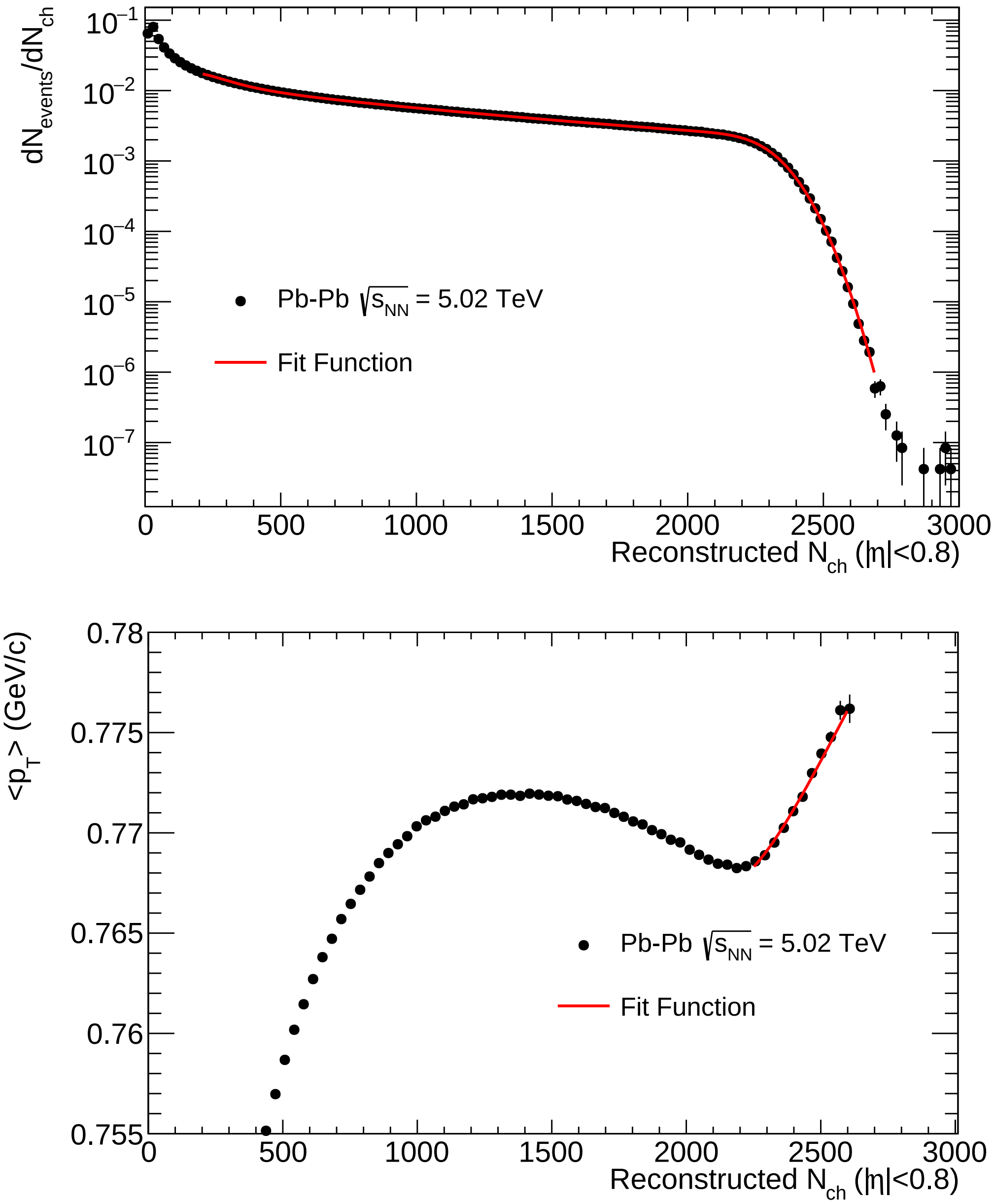

Figure 39: Fit results on data obtained from Pb-Pb collisions before corrections and c_s^2 calculations using method two. The uncertainties shown for the data are statistical.

6.1 Data Corrections

To obtain the most accurate values of the speed of sound, it is necessary to correct the correlation between primary charged particle p_{T} spectra and their corresponding event multiplicities N_{ch}. The corrections for efficiency are obtained using Monte Carlo simulations based on a realistic GEANT model of the ALICE detector and the experimental conditions present during data-taking. These simulations provide information about efficiency, secondary contamination, and smearing of N_{ch} and p_{T}. However, it has been found in previous measurements that the current state-of-the-art MC event generators do not perfectly reproduce the relative particle abundances. This means that a purely MC-based correction for efficiency and feed-down contamination of inclusive charged particles would depend on the accuracy of the relative hadron abundances produced by the respective underlying event generator. To take this effect into account, a data-driven approach is used to re-weight the particle abundances from the event generator. This particle-composition correction utilizes several ALICE measurements of identified $(\pi, \mathrm{K}, \mathrm{p}, \Lambda)$ particle p_{T} spectra as a function of multiplicity for a range of collision systems as input. These data-driven adjustments for the generator bias result in a more accurate description of the detector performance and are applied prior to the unfolding corrections.

In the experiment, the measured transverse momentum $p_{\mathrm{T}}^{\mathrm{meas}}$ spectra are obtained as a function of the number of measured tracks $N_{\mathrm{ch}}^{\mathrm{meas}}$. The measured multiplicity $N_{\mathrm{ch}}^{\mathrm{meas}}$ contains a fraction of the true primary charged-particle multiplicity $N_{\mathrm{ch}}^{\mathrm{true}}$ that is not lost due to acceptance, efficiency, or track selection, as well as additional tracks from secondary particles or particles smeared into the kinematic acceptance of the measurement due to detector resolution.

Due to event-by-event fluctuations of the detector efficiency and the contamination of the track sample, there is no unique correlation between $N_{\mathrm{ch}}^{\mathrm{true}}$ and $N_{\mathrm{ch}}^{\mathrm{meas}}$. Events with a true multiplicity can be measured with different $N_{\mathrm{ch}}^{\mathrm{meas}}$ and therefore contribute to various multiplicity dependent measured p_{T} spectra. Consequently, each of those spectra contains particles originating from events with many different true multiplicities. This means that the physical quantity characterizing the final state of a collision (p_{T} spectra vs. $N_{\mathrm{ch}}^{\mathrm{true}}$) cannot be directly observed and can only be extracted by deconvoluting the measured data.

The procedure for unfolding the spectra of charged particle tracks measured as a function of $p_{\mathrm{T}}^{\mathrm{meas}}$ and $N_{\mathrm{ch}}^{\mathrm{meas}}$, to yield the primary charged-particle p_{T} spectra as functions of their primary charged-particle multiplicity N_{ch}, is based on an iterative deconvolution method. This method is illustrated in the next section for the simple use case of unfolding event multiplicity distributions.

6.2 Unfolding Procedure

As mentioned before, due to the finite resolution of particle detectors, any measurement conducted in experimental high-energy physics is contaminated by smearing. We parametrize the measurement effects using a response matrix, as shown in Figures 40 and 41, that maps the (binned) true distribution onto the measured one. One-dimensional iterative Bayesian unfolding method by G. D' Agostini [5] has been used to unfold the measured multiplicity distribution. The key idea in Bayesian unfolding is to use Bayes' theorem, which is a way of unfolding experimental data to get the best estimates of the true distributions. This study examines the correlation between the N_{meas} with their corresponding true multiplicities N_{ch}. From the experiment, the transverse momentum spectra are obtained as functions of the number of measured tracks N_{meas}. This method has already been done by some other groups for pp, p–Pb, and Pb–Pb collisions [77, 78].

For Bayesian unfolding, one needs to have the smearing matrix S, which contains information about the finite resolution and acceptance of the detectors. It will give access to the conditional probability of an event with true multiplicity that has been considered as one with measured multiplicity. By having the smearing matrix, one can formulate the relationship between true multiplicity distribution and measured one with a mathematical equation:

$$F(N_{\mathrm{ch}}^{\mathrm{meas}}) = \sum_{\mathrm{true}} S_{(\mathrm{meas},\mathrm{true})} \cdot F(N_{\mathrm{ch}}^{\mathrm{true}}) \tag{41}$$

in which $F(N_{\text{ch}}^{\text{meas}})$ and $F(N_{\text{ch}}^{\text{true}})$ represent the measured and true multiplicity distributions, respectively. This equation can not be solved easily by just inverting the response matrix since it might have multiple solutions or none at all. The method proposed in G. D' Agostini [5] paper obtains the true distribution by Bayes theorem. Considering that the probabilities of observing a true $N_{\text{ch}}^{\text{true}}$ and a measured $N_{\text{ch}}^{\text{meas}}$ multiplicity are given by $P(N_{\text{ch}}^{\text{true}})$ and $P(N_{\text{ch}}^{\text{meas}})$, respectively, the conditional probability of observing $N_{\text{ch}}^{\text{true}}$ and $N_{\text{ch}}^{\text{meas}}$ at the same time is given by the joint probability $P(N_{\text{ch}}^{\text{true}} \cap N_{\text{ch}}^{\text{meas}})$. The conditional probabilities $P(N_{\text{ch}}^{\text{true}} \mid N_{\text{ch}}^{\text{meas}})$ and $P(N_{\text{ch}}^{\text{meas}} \mid N_{\text{ch}}^{\text{true}})$ are connected with $P(N_{\text{ch}}^{\text{true}} \cap N_{\text{ch}}^{\text{meas}})$, according to the following equations:

$$P(N_{\text{ch}}^{\text{true}} \mid N_{\text{ch}}^{\text{meas}}) = \frac{P(N_{\text{ch}}^{\text{true}} \cap N_{\text{ch}}^{\text{meas}})}{P(N_{\text{ch}}^{\text{meas}})} \tag{42}$$

$$P(N_{\text{ch}}^{\text{meas}} \mid N_{\text{ch}}^{\text{true}}) = \frac{P(N_{\text{ch}}^{\text{meas}} \cap N_{\text{ch}}^{\text{true}})}{P(N_{\text{ch}}^{\text{true}})}. \tag{43}$$

Using the above equations, Bayes' theorem can be written as:

$$P(N_{\text{ch}}^{\text{true}} \mid N_{\text{ch}}^{\text{meas}}) = \frac{P(N_{\text{ch}}^{\text{meas}} \mid N_{\text{ch}}^{\text{true}})P(N_{\text{ch}}^{\text{true}})}{P(N_{\text{ch}}^{\text{meas}})}, \tag{44}$$

which gives the probability of true multiplicity, given that the measured one is accessible by experimental data. The total probability of measuring an event with the true multiplicity can be written as:

$$P(N_{\text{ch}}^{\text{meas}}) = \sum_{\text{true}} P(N_{\text{ch}}^{\text{meas}} \cap N_{\text{ch}}^{\text{true}}) = \sum_{\text{true}} P(N_{\text{ch}}^{\text{meas}} \mid N_{\text{ch}}^{\text{true}})P(N_{\text{ch}}^{\text{true}}). \tag{45}$$

Now the final Bayesian Theorem can be rewritten as

$$P(N_{\text{ch}}^{\text{true}} \mid N_{\text{ch}}^{\text{meas}}) = \frac{P(N_{\text{ch}}^{\text{meas}} \mid N_{\text{ch}}^{\text{true}})P(N_{\text{ch}}^{\text{true}})}{\sum_{\text{true}} P(N_{\text{ch}}^{\text{meas}} \mid N_{\text{ch}}^{\text{true}})P(N_{\text{ch}}^{\text{true}})} \tag{46}$$

The left side of the above equation gives us the so-called Unfolding Matrix, $U_{(true,meas)}$. By having this matrix, one can obtain the unfolded distribution:

$$F(N_{\mathrm{ch}}^{\mathrm{true}}) = \sum_{\mathrm{meas}} U_{(\mathrm{true},\mathrm{meas})} \cdot F(N_{\mathrm{ch}}^{\mathrm{meas}}) \tag{47}$$

The unfolding procedure is iterative, and after some iterations, the unfolding distribution gets close to the true distribution, but the effects of statistical uncertainties appear in the matrix; thus, more iterations will not result in more accurate results. Starting with an initial assumption (prior) for the desired multiplicity distribution, (in this analysis, it is taken from the MC simulation), unfolding weights (posterior probabilities) are obtained by combining the prior with the detector response and the measured track multiplicity distribution according to Bayesian theorem. By again applying these posterior probabilities to the measured track multiplicity distribution, an updated and more accurate guess for the prior is calculated. The decision about the optimal number of iterations is based on χ^2/DOF of the true and unfolded distributions. The number of degrees of freedom is the number of data points in the respective distribution.

Multiple variables can affect the measurement of the charged particle multiplicity distributions. In experimental measurements, some collisions within $|V_z| < 10$ cm with respect to the nominal interaction vertex might not be detected by the minimum-bias trigger, or they might not be considered in the next level event selections. Depending on the vertex-position resolution of the experiment, an event might be reconstructed outside of $|V_{\mathrm{z}}^{\mathrm{meas}}| < 10$ cm and will be rejected as a result of analysis cuts. There is also another scenario in which the measured, and selected events might consist of collisions that do contain any primary charged particles that are produced in the kinematic ranges of interest (i.e., events with $N_{\mathrm{ch}} = 0$) or collisions that do have a true vertex position but are located outside $|V_{\mathrm{z}}| < 10$ cm. Besides, as mentioned before, the measured multiplicity $N_{\mathrm{ch}}^{\mathrm{meas}}$ itself is affected by track selection, tracking efficiencies, contamination with secondaries and particles smeared into the kinematic acceptance, resulting in correlations between the true number of charged particles $N_{\mathrm{ch}}^{\mathrm{true}}$ and the measured track multiplicity $N_{\mathrm{ch}}^{\mathrm{meas}}$. Using MC simulations, the measured track multiplicity distribution can be corrected for the efficiency, contamination, and smearing effects by means of the iterative unfolding procedure.

6.3 Response Matrix

As mentioned before, in Bayesian unfolding, the response matrix is a key component of the method. It represents the probability of detecting a particle with a certain set of properties at the detector level given that it was produced with a certain set of properties at the particle level. It characterizes the detector's response to the particles, which can be affected by various factors such as detector efficiency, resolution, and acceptance. The response matrix is constructed using Monte Carlo simulations, which simulate the interactions of particles with the detector and produce samples of the particle-level and detector-level distributions. For each particle-level bin, the corresponding detector-level bin is filled with the probability that a particle produced in that bin would be detected in the corresponding detector-level bin. The response matrix is thus a square matrix with dimensions equal to the number of bins in both the particle-level and detector-level distributions. The response matrix can be used to predict the detector-level distribution for a given particle-level distribution using matrix multiplication. Specifically, the predicted detector-level distribution is obtained by multiplying the response matrix by the true particle-level distribution. This predicted distribution can then be compared with the observed detector-level distribution to obtain the likelihood function in the Bayesian unfolding procedure. Figures 40 and 41 are response matrices for Xe-Xe and Pb-Pb collisions, respectively.

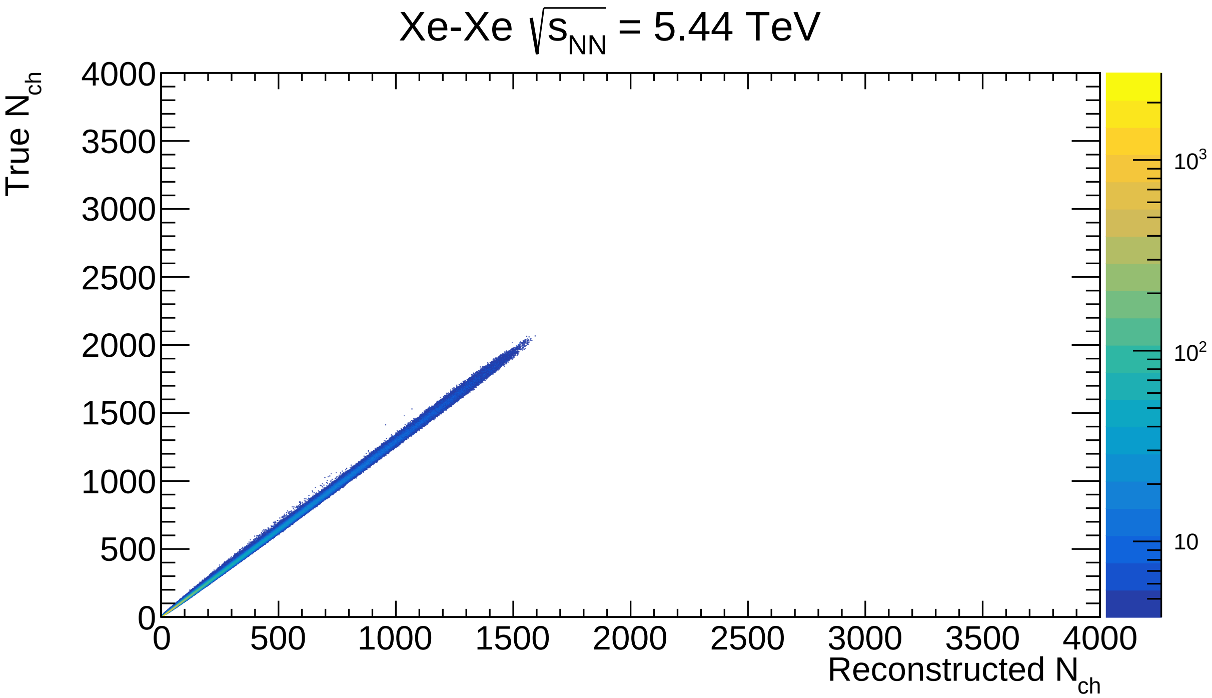

Figure 40: Response matrix of measured multiplicity, $N_{\rm ch}^{\rm meas}$, and true multiplicity, $N_{\rm ch}^{\rm true}$ in Xe-Xe collisions.

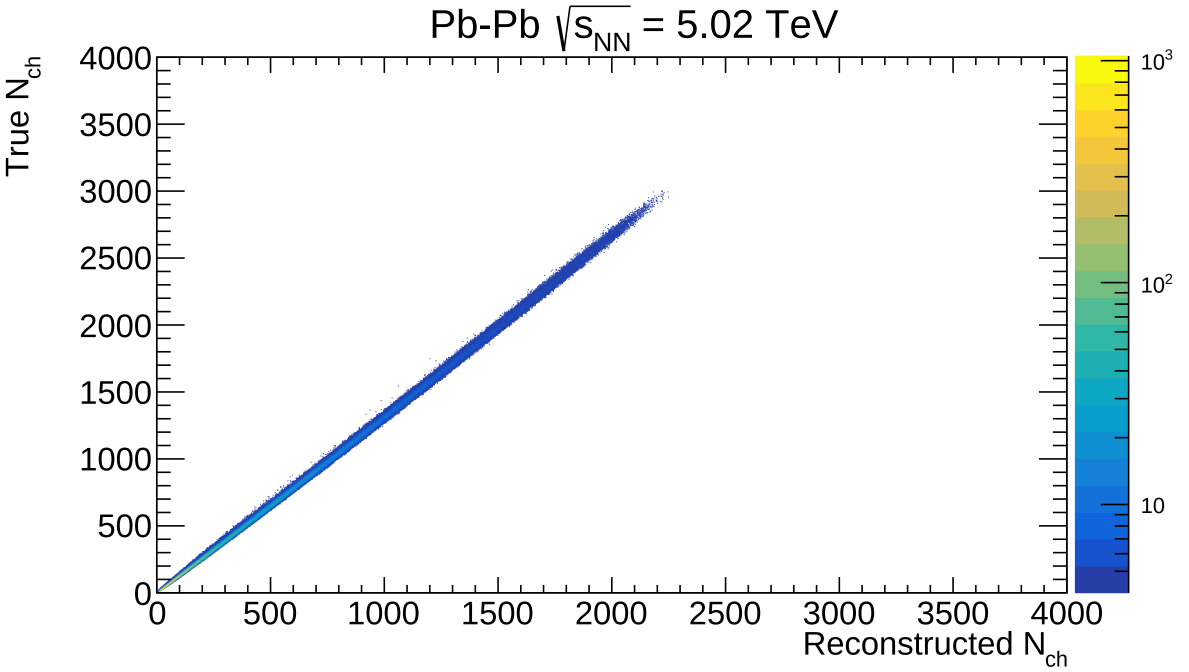

Figure 41: Response matrix of measured multiplicity, $N_{\rm ch}^{\rm meas}$, and true multiplicity, $N_{\rm ch}^{\rm true}$ in Pb-Pb collisions.

6.3.1 Rebuilding Response Matrix

The simulated response matrix is affected by the limited statistics for high multiplicities. Since this analysis depends on ultra-central collisions and high multiplicities, one can rebuild a simulated response matrix to extend higher multiplicities using the binomial probability distribution. The binomial distribution is a discrete probability distribution that describes the number of successes in a fixed number of independent trials, where each trial has the same probability of success. Rebuilding the response matrix using a binomial distribution is in cases where the detector response can be described such as the probability of a particle being detected in a given detector bin. In this context, the binomial distribution is used to describe the probability of a particle being detected in a given detector bin given its properties at the particle level since for each generated multiplicity bin, there's a corresponding reconstructed probability distribution that can be extracted from the response matrix. Then the Binomial distribution is obtained as a function of the generated multiplicity using:

$$f\left(N_{\mathrm{ch}}^{\mathrm{meas}}, N_{\mathrm{ch}}^{\mathrm{true}}, \varepsilon\right) = \left(\begin{array}{c} N_{\mathrm{ch}}^{\mathrm{true}} \\ \\ N_{\mathrm{ch}}^{\mathrm{meas}} \end{array}\right) \varepsilon^{N_{\mathrm{ch}}^{\mathrm{meas}}} (1-\varepsilon)^{N_{\mathrm{ch}}^{\mathrm{true}} - N_{\mathrm{ch}}^{\mathrm{meas}}}, \tag{48}$$

where $N_{\mathrm{ch}}^{\mathrm{true}}$, $N_{\mathrm{ch}}^{\mathrm{meas}}$ and ε are generated multiplicity distribution, reconstructed multiplicity distribution, and efficiency, respectively. The efficiency ε can be directly obtained from the data in Figures 40 and 41, by determining $< N_{\mathrm{ch}}^{\mathrm{meas}} > / N_{\mathrm{ch}}^{\mathrm{true}}$. The values determined for Xe-Xe and Pb-Pb were found to be 0.766 and 0.745 respectively, and independent of $N_{\mathrm{ch}}^{\mathrm{true}}$. Figure 42 shows the rebuilt response matrices, using a sampling of Equation (48). For a fixed $N_{\mathrm{ch}}^{\mathrm{true}}$, the widths of the distributions were compared with widths in Figures 40 and 41, and found to be consistent. This demonstrates the distribution of the response matrix is dominated by binomial efficiency losses, justifying the assumption used for the rebuilt matrix.

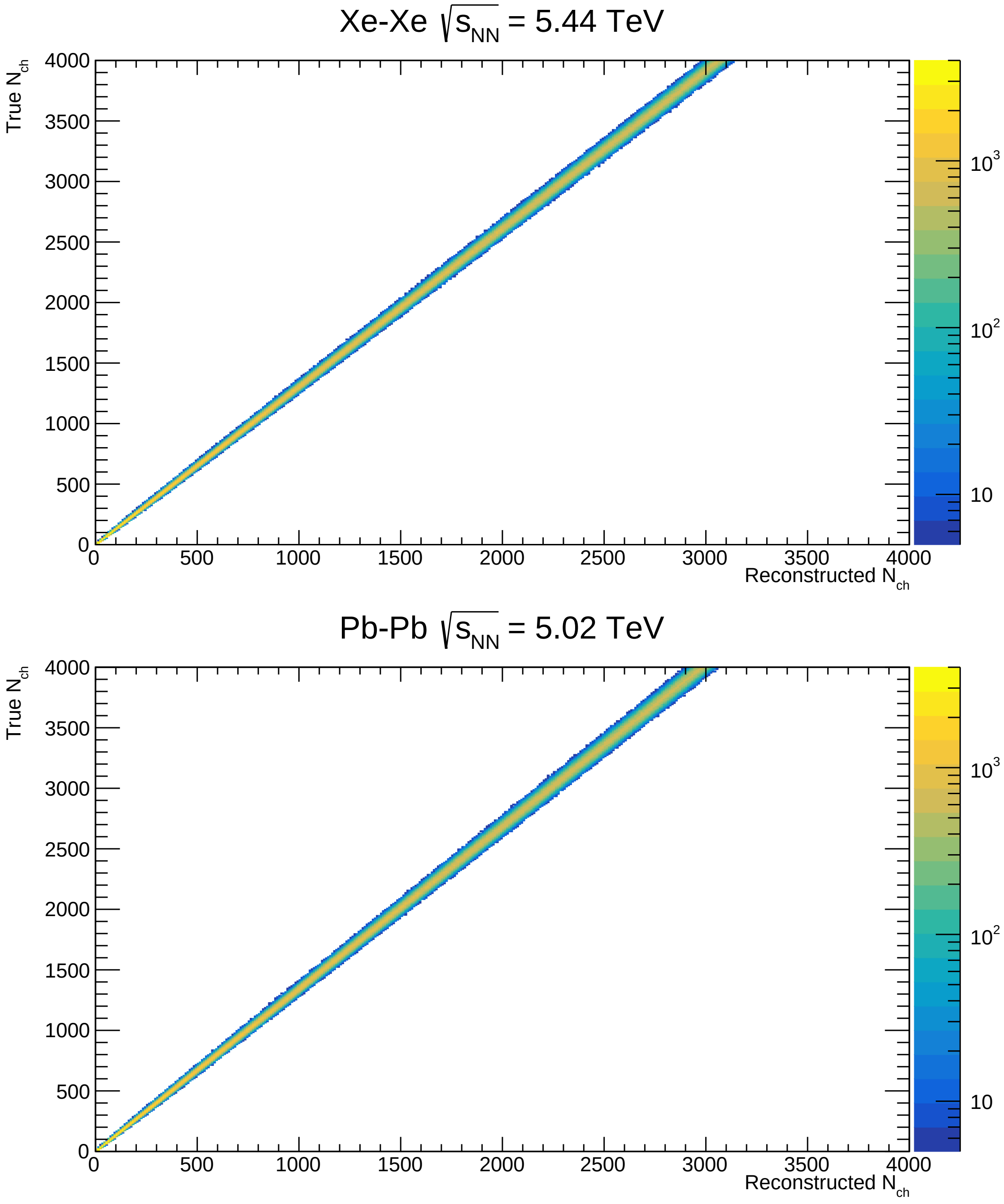

Figure 42: New response matrices after the rebuilding procedure for Xe-Xe and Pb-Pb collisions.

6.4 Closure Test

In order to validate the accuracy of the unfolding method, the previous Monte Carlo simulations can be used. In this test, the true multiplicity distribution, also known as generated multiplicity

$(N_{\mathrm{ch}}^{\mathrm{true}})_{MC}$ of the simulated collisions is known, and it can be compared to the unfolded multiplicity distribution $N_{\mathrm{ch}}^{\mathrm{unf}}$ obtained by applying the unfolding method to the measured multiplicity distribution also known as Reconstructed multiplicity $(N_{\mathrm{ch}}^{\mathrm{meas}})_{MC}$. By performing this closure test, one can ensure that the unfolding method is able to correct detector effects in a reliable and accurate manner and that it can be applied to real data to obtain corrected distributions. Monte Carlo simulations are an essential tool for performing such tests, as they allow one to control the input distributions and generate large enough samples to obtain statistically meaningful results. Figure 43 shows such a closure test for HIJING simulations of Xe-Xe and Pb-Pb collisions. The unfolding uses the Bayesian method, with the number of iterations being 4 for each system. It is clear the closure test is successful. The unfolded distributions fully overlap with the generated distributions, and this is particularly clear for the ultra-central collisions i.e. high values of N_{ch} relevant for this analysis.

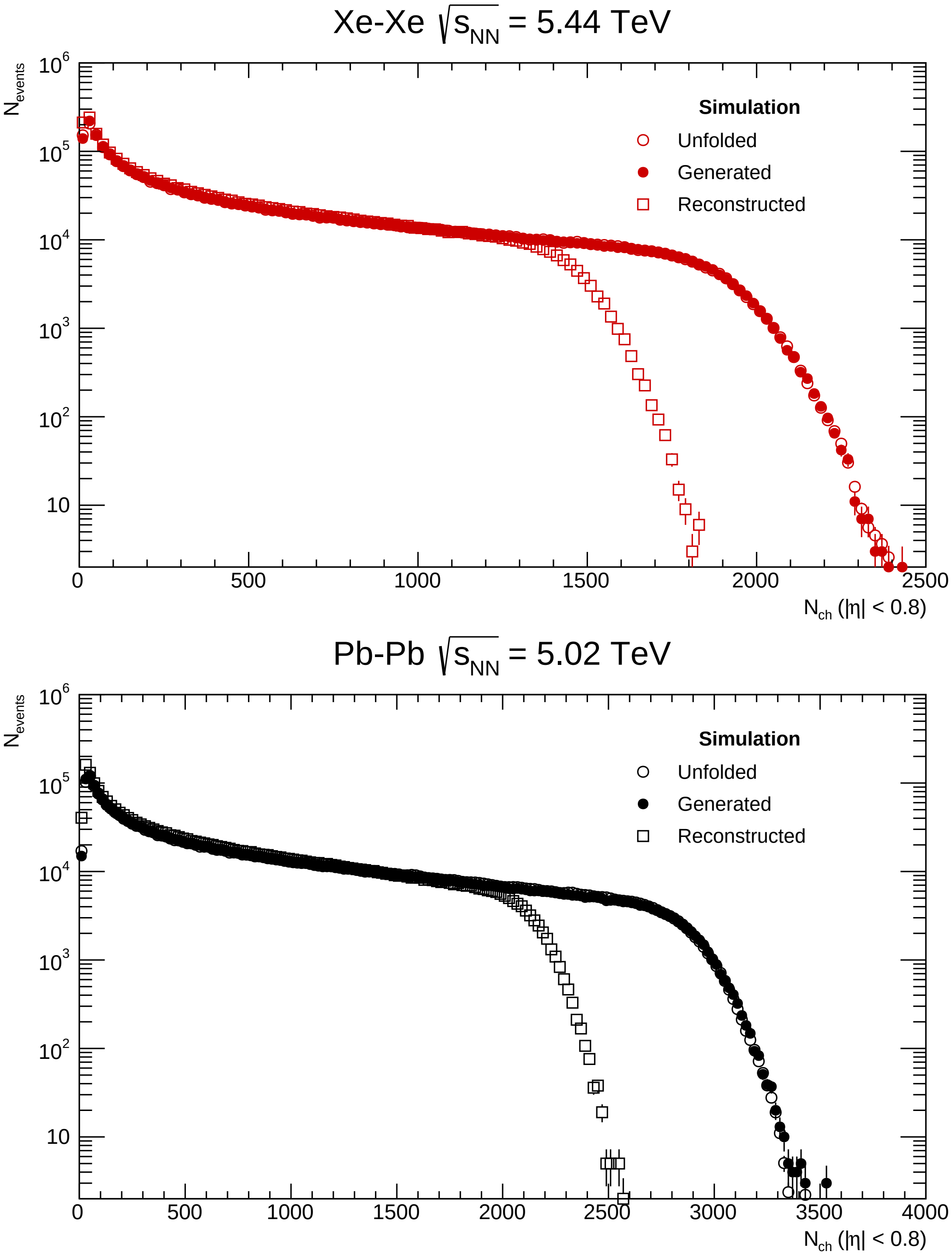

Figure 43: Closure test for unfolding the reconstructed multiplicity distributions from the HIJING event generator using the generated multiplicity distribution as a true distribution in the Xe-Xe and Pb-Pb collisions.

6.5 Efficiency Corrections

In heavy ion collision experiments, the collected dataset has limited statistics. In addition, the detectors involved in the data collection have limited efficiency. That is why one needs to have a complete idea of detector efficiencies and how to do the correction for the detector effects. This is addressed through the MC study. In ALICE, various event generators are utilized for Monte Carlo (MC) studies, depending on the physics requirements. This analysis employed HIJING [8]. events for the MC study, which is mentioned before. This correction is obtained from the MC simulation tracking efficiency for primary charged particles. The tracking efficiency described here is determined by comparing the number of reconstructed primary charged particles that depend on the generated transverse momentum (p_{T}) to the number of generated primary charged particles that also depend on the generated p_{T}, expressed as a ratio:

$$\varepsilon_{\mathrm{prim}}^{\mathrm{MC}}\ (p_{\mathrm{T}}) = \frac{Y_{\mathrm{prim,rec}}^{\mathrm{MC}}\,(p_{\mathrm{T}})}{Y_{\mathrm{prim,gen}}^{\mathrm{MC}}\,(p_{\mathrm{T}})}. \tag{49}$$

One way to correct the detector effects is to apply this correction factor to the measured data, which is obtained from Monte Carlo (MC) simulations. This correction factor accounts for the difference between the reconstructed and generated quantities due to detector inefficiencies. To obtain the correction factor, one needs to simulate the same physics process that was measured in the detector using MC simulations. The generated events are passed through a simulation of the detector response, which takes into account the detector resolution, efficiency, and acceptance. The simulated data are then processed using the same analysis chain as the real data. Once the simulated data are processed, one can compare the number of reconstructed particles to the number of generated particles as a function of some kinematic variables such as transverse momentum (p_{T}) and rapidity (y). The ratio of reconstructed to generated particles, which is the correction factor, is then extracted as a function of these kinematic variables (see Figure 44).

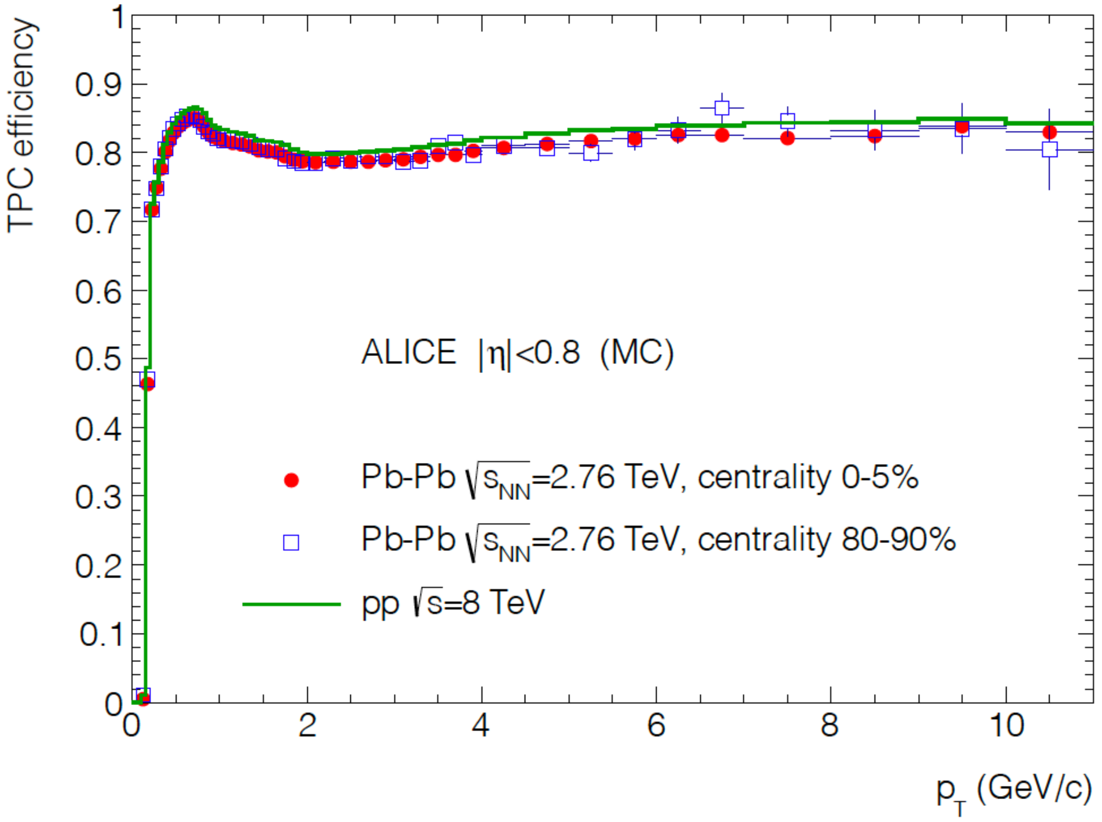

Figure 44: Track finding efficiency for primary particles in Pb–Pb collisions (Monte Carlo simulation) [87].

The corrected distribution of some variable X can then be obtained by multiplying the measured distribution by the correction factor. Overall, tracking efficiency is a crucial factor in the accurate reconstruction of charged particle tracks in the TPC detector. It is affected by various factors such as detector resolution, gas properties, magnetic field strength, and the algorithms used for track reconstruction. The MC simulations help in understanding these factors and correcting them to improve tracking efficiency. Figure 45 shows the track finding efficiency obtained for both Xe-Xe and Pb-Pb collisions.

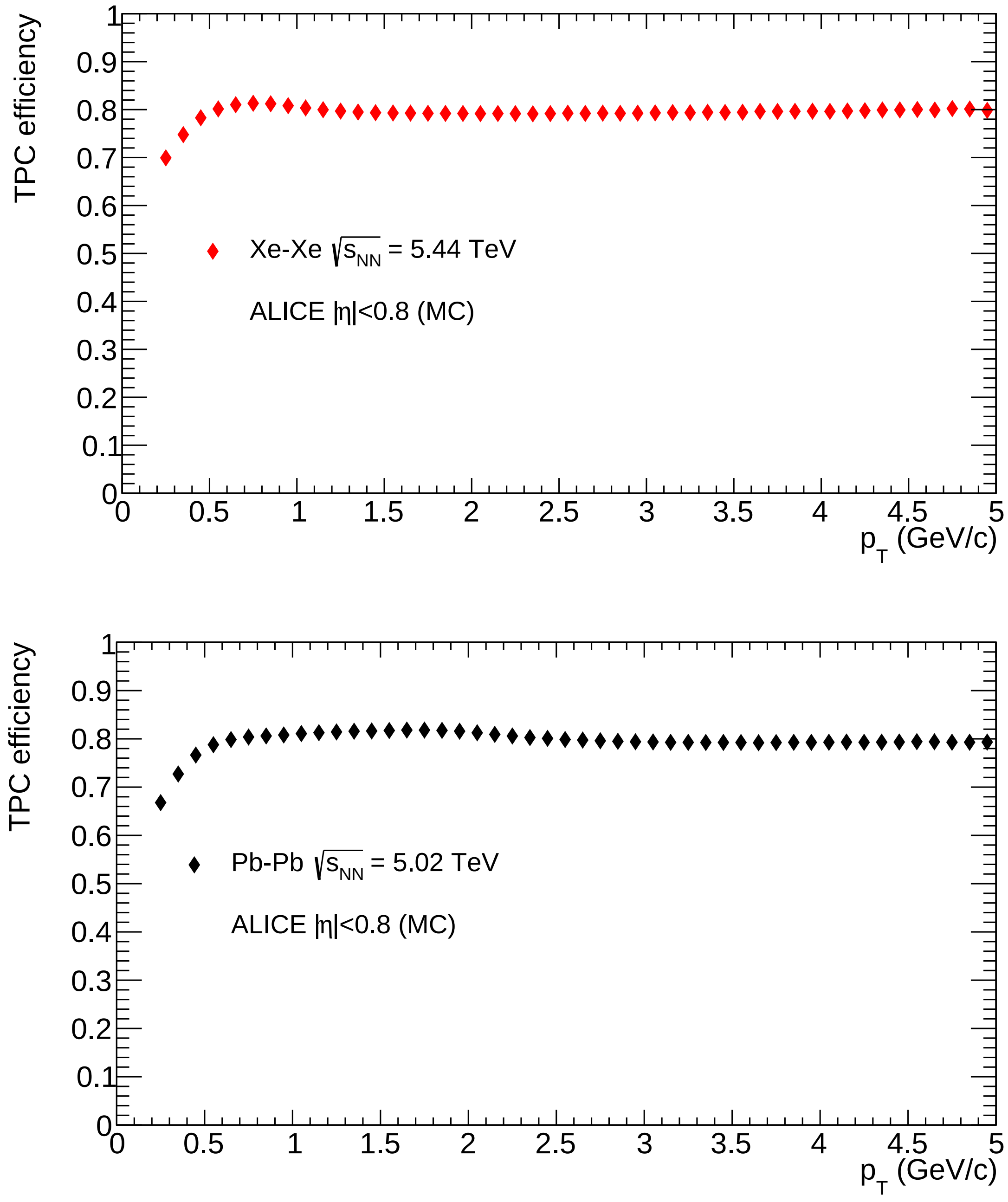

Figure 45: Track finding efficiency in TPC for primary particles in Xe-Xe (upper panel) and Pb–Pb (lower panel) collisions by Monte Carlo simulation.

6.6 Fully Corrected Results

Following the reconstruction of the response matrix, the unfolding procedure was verified using a closure test, which involved employing Monte Carlo reconstructed and generated multiplicity distributions. Since the closure test yielded satisfactory results, the unfolding procedure can be applied to data, using the same number of iterations (4). The outcome of the unfolding process on the multiplicity distributions for both Xe-Xe and Pb-Pb collisions is shown in Figures 46 and 47, respectively. Figures 48 and 49 show the unfolded multiplicity distributions again, and corrected measurements of $< p_{\mathrm{T}} >$ vs. N_{ch}. In order to determine the corrected value of N_{ch} for a given reconstructed value N_{ch}, the unfolded multiplicity distributions are refolded, and $< N_{\mathrm{ch}}^{\mathrm{true}} >$ is obtained for the appropriate $N_{\mathrm{ch}}^{\mathrm{meas}}$ range. The transverse momentum spectrum within the $N_{\mathrm{ch}}^{\mathrm{meas}}$ range is then corrected for p_{T}-dependent efficiency, in order to obtain a corrected value of $< p_{\mathrm{T}} >$. All of these distributions are then fitted using method two, in order to obtain the speed of sound squared. Figure 50 shows the natural logs of corrected values $< p_{\mathrm{T}} >$ and N_{ch}, and these are fitted using method one.

Table 3: Speed of sound values after corrections

System	$\sqrt{s_{\mathrm{NN}}}$[TeV]	Method One	Method Two
Xe-Xe	5.44	$c_s^2 = 0.066 \pm 0.007$	$c_s^2 = 0.096 \pm 0.0011$
Pb-Pb	5.02	$c_s^2 = 0.077 \pm 0.002$	$c_s^2 = 0.10 \pm 0.0024$

Values of the speed of sound squared for every collision system and method utilized after the corrections.

Table 3 shows obtained values of the speed of sound squared using the corrected data. While there are differences with respect to the uncorrected values in table 2, there are no systematic shifts i.e. sometimes they are higher for a given system and method, and sometimes they are lower. This demonstrates the impact of the corrections is rather minimal for the speed of sound extraction, demonstrating it is rather robust with respect to the detector effects. Finally, in Figure 51, the extracted speed of sound values is compared with expectations from the theory. They appear consistent with calculations obtained at temperatures close to the QGP/hadron gas phase transition.

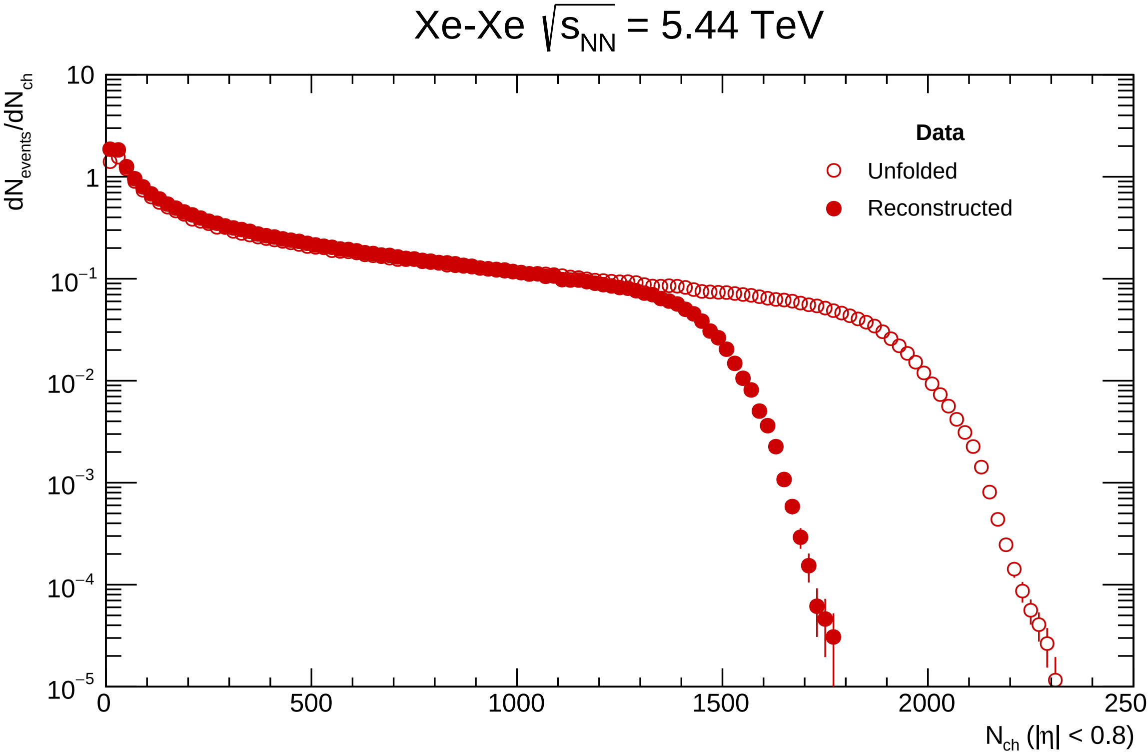

[b]

Figure 46: Result of the unfolding procedure for multiplicity distributions in the Xe-Xe collision.

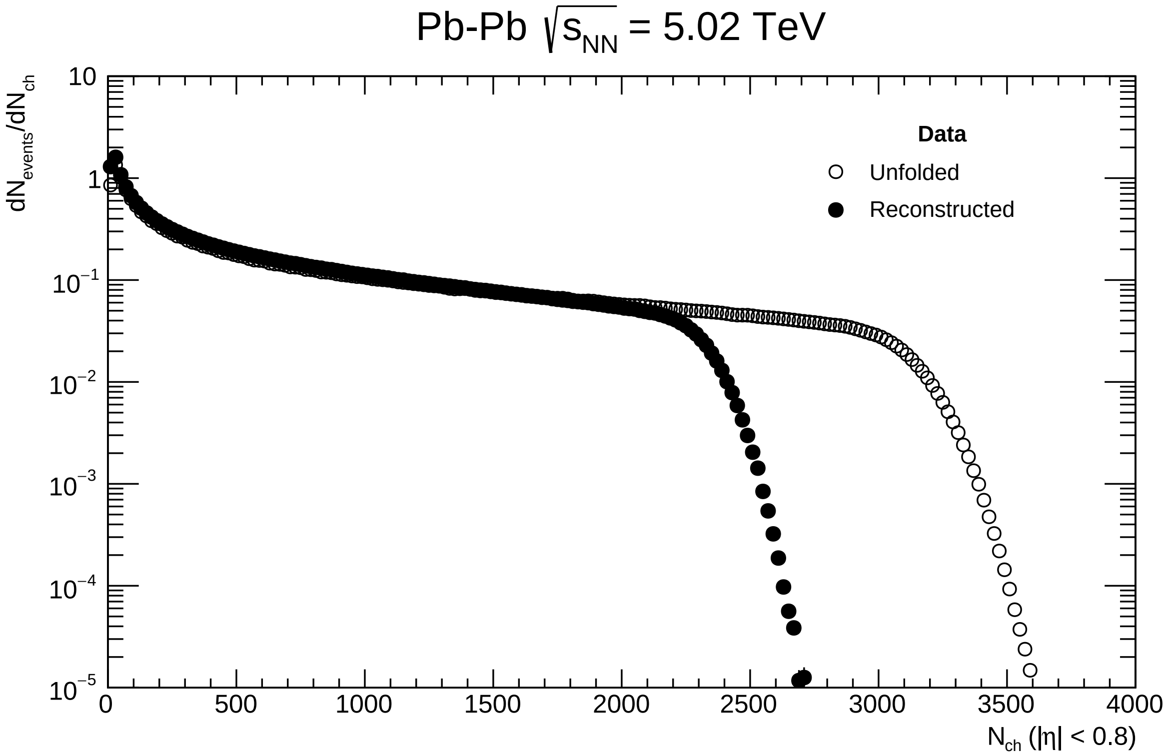

Figure 47: Result of the unfolding procedure for multiplicity distributions in the Pb-Pb collision.

7 Summary and Outlook

The purpose of the ALICE experiment is to study the properties of quark-gluon plasma (QGP), a state of matter that is believed to have existed just after the Big Bang. By colliding heavy ions at high energies, ALICE can recreate the conditions that existed just after the Big Bang and study the properties of the QGP. One way to deepen our knowledge about the early universe is to study the thermodynamic properties of the QGP. By analyzing the thermodynamic properties of the QGP, one can investigate QGP behavior and gain insights into the underlying physics that governs its properties. One key property that can be studied through thermodynamics is the equation of the state of the QGP. This equation relates the pressure, temperature, and energy density of the plasma, and provides important information about the nature of the interactions between the

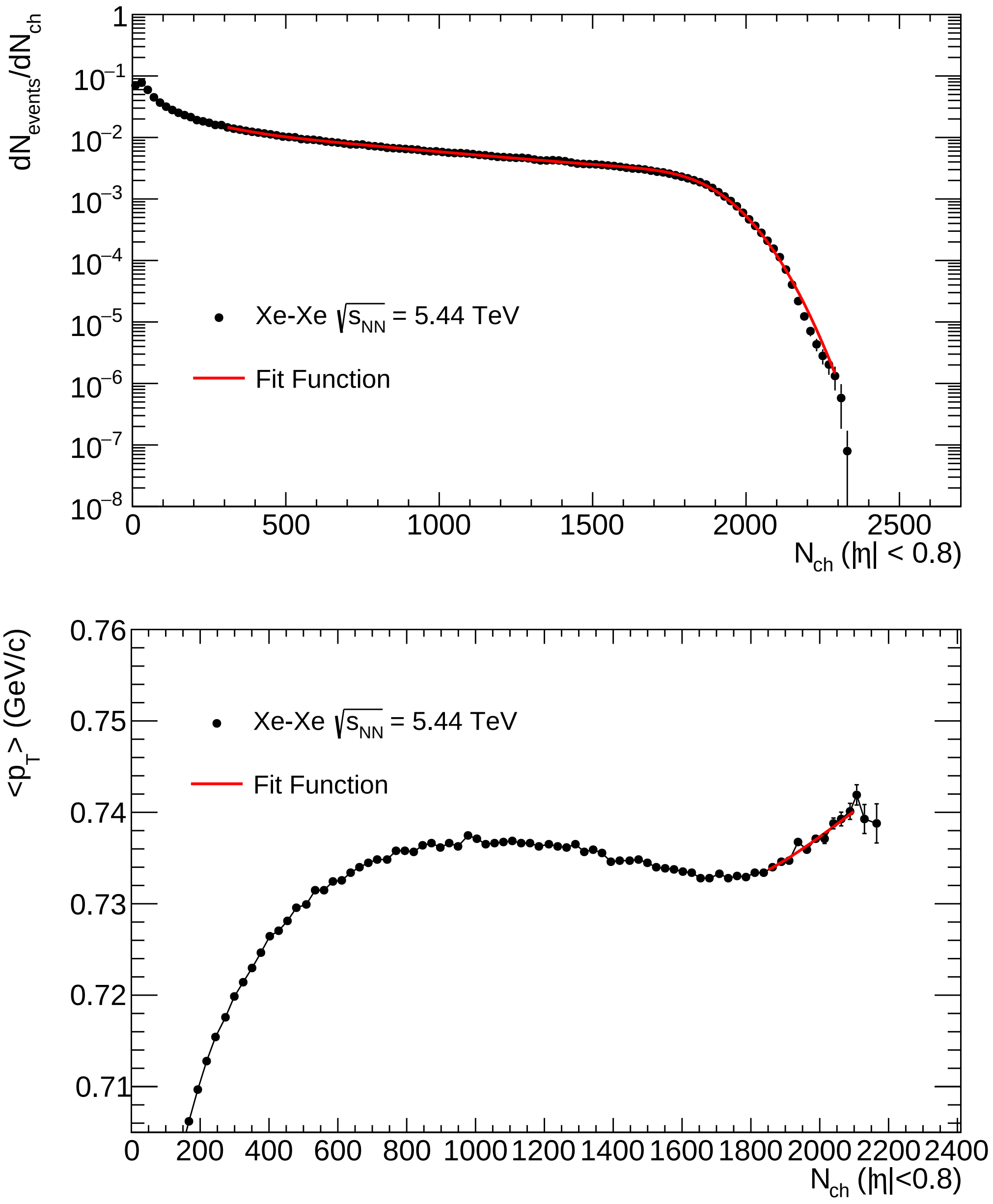

Figure 48: Fit results on data obtained from Xe-Xe collisions after corrections and c_s^2 calculations using method two.

particles that make up the plasma. By investigating the equation of state of the QGP, one can test theoretical models of the strong nuclear force, such as Lattice QCD. The speed of sound is one important thermodynamic property of the quark-gluon plasma (QGP) that can be studied through experiments at the Large Hadron Collider (LHC) and other facilities. The speed of sound

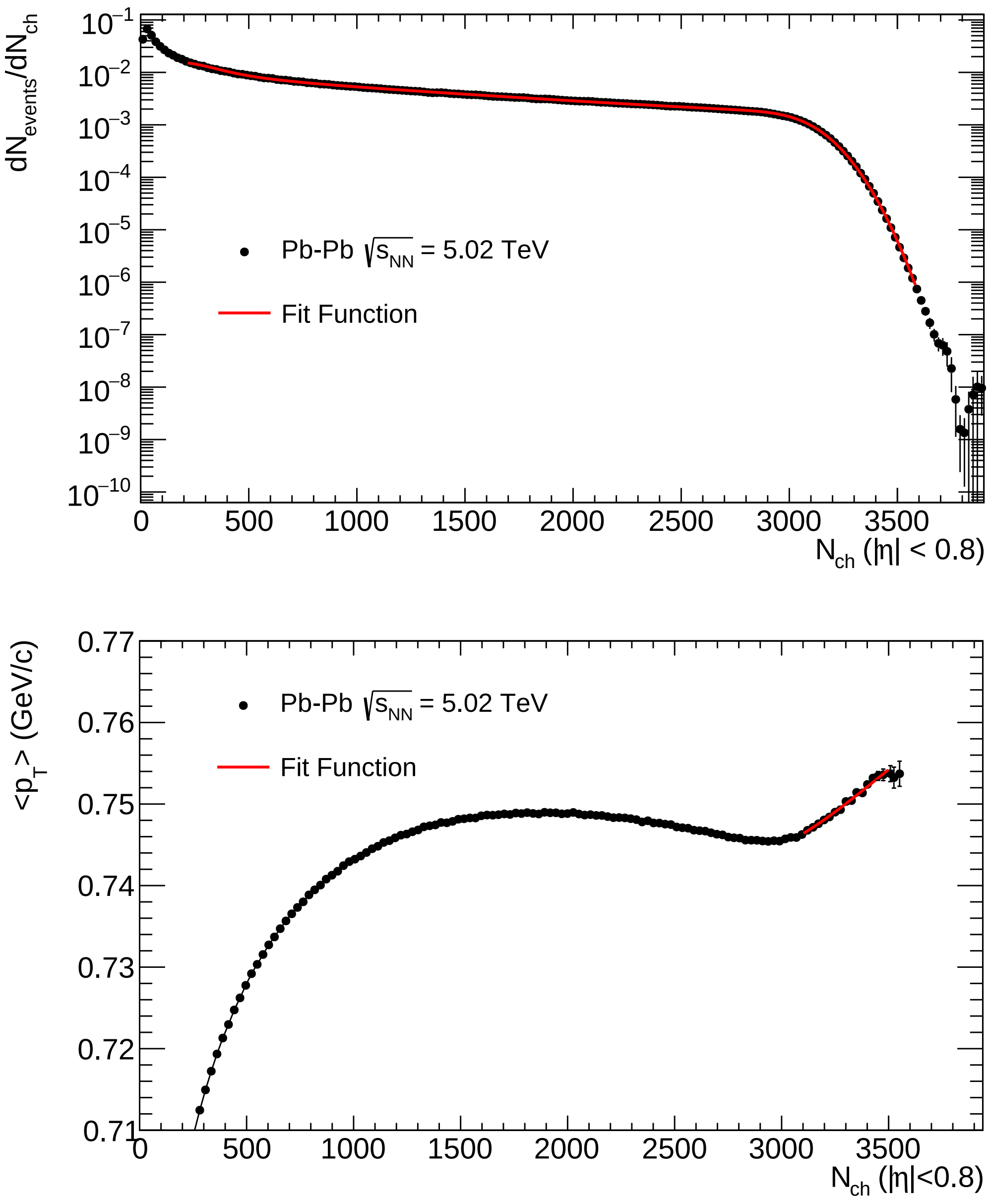

Figure 49: Fit results on data obtained from Pb-Pb collisions after corrections and c_s^2 calculations using method two.

is a measure of how quickly sound waves can travel through a material, and it depends on the thermodynamic properties of the material, such as its temperature, pressure, and density. In the case of the QGP, the speed of sound is an important indicator of the compressibility of the plasma, which is related to the strength of the interactions between the particles that make up the plasma.

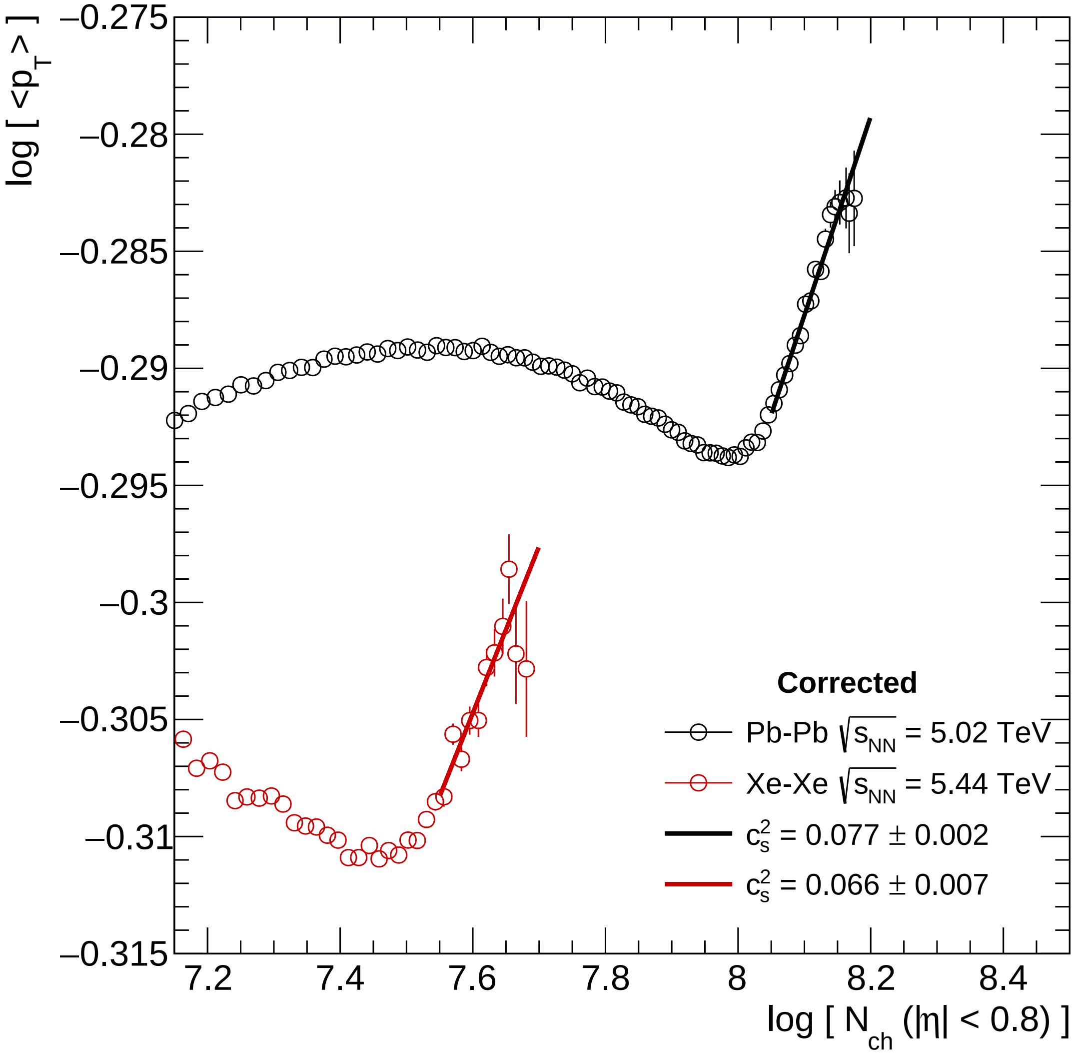

Figure 50: Fit results on data obtained from heavy-ion collisions after corrections and c_s^2 calculations using method one.

This dissertation has investigated and analyzed the collision data obtained from Pb-Pb collisions at $\sqrt{s_{NN}} = 5.02$ TeV and Xe-Xe collisions at $\sqrt{s_{NN}} = 5.44$ TeV from the LHC running period 2 to investigate measurements of the speed of sound at LHC. This dissertation used all the charged particles measured by the ALICE detector for the kinematic ranges in pseudo-rapidity of $|\eta| < 0.8$ and in the transverse momentum range of 0.2 GeV/c $< p_T <$ 5 GeV/c. The values of the speed of sound obtained from Xe-Xe and Pb-Pb collisions, and shown in Figure 51, are consistent with

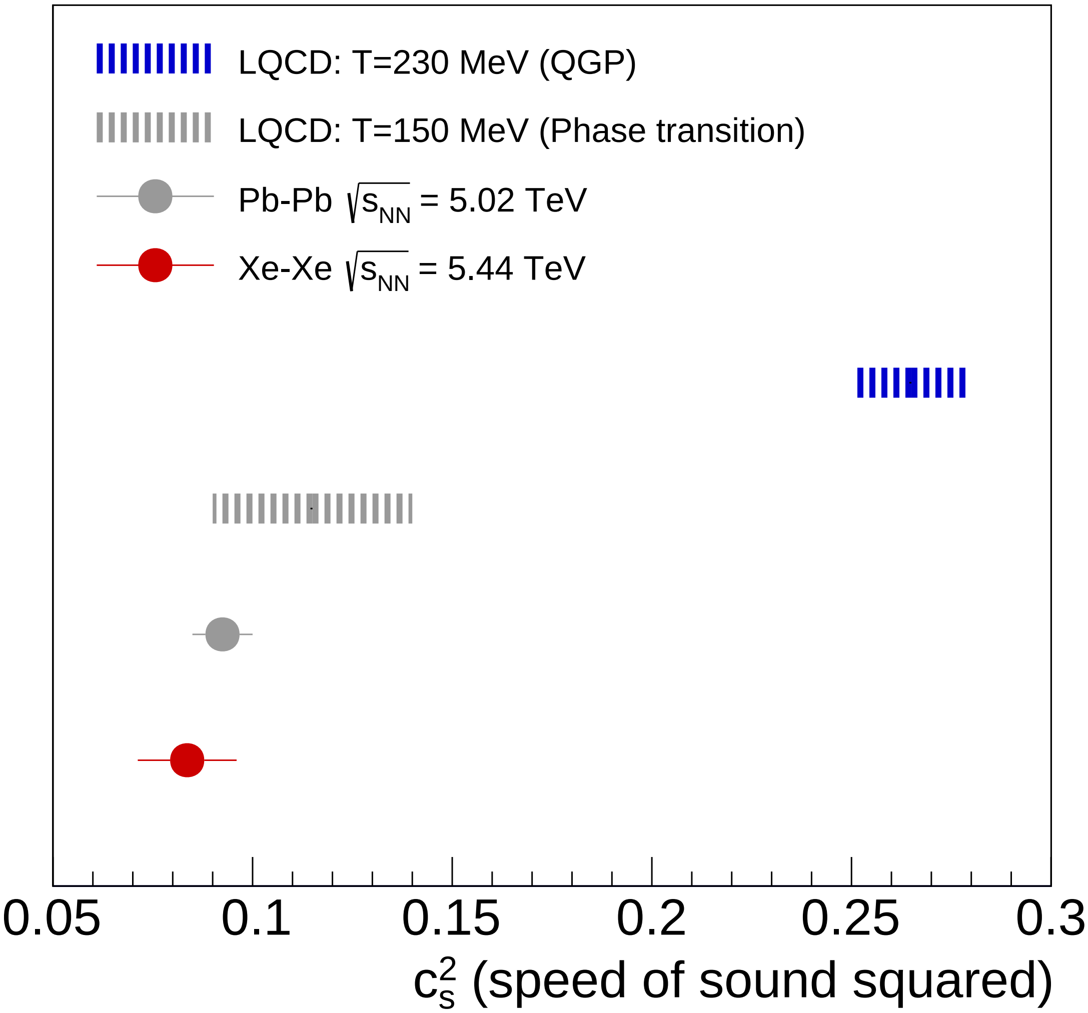

Figure 51: Results of Lattice Quantum Chromodynamics (LQCD) computations [70] for c_s^2 at different temperatures compared with the speed of sound squared (c_s^2) extracted from Xe-Xe and Pb-Pb collisions. The uncertainties associated with c_s^2 from data are determined from the differences between methods one and two.

Lattice QCD at a temperature around the phase transition. This implies the methods investigated are perhaps extracting the speed of the sound in the final hadronic state, as opposed to the QGP phase, where the speed of sound is larger. This is arguably expected, as the ALICE detector measures hadrons from the final state. A higher value in the QGP phase is expected, as the QGP is a strongly interacting liquid, which is less compressible than the gas in the hadronic phase. Future measurements of $\langle p_T \rangle$ vs. the number of charged particles in ultra-central heavy-ion collisions could pursue electromagnetic probes, such as photons and/or leptons. These are produced in the QGP phase but don't interact with the strongly coupled matter, therefore offering a more direct probe of the thermodynamic properties of the QGP.

A Appendix

A.1 Jets in Heavy Ion Collisions

In heavy ion collisions, when a quark or gluon undergoes hadronization, it produces a narrow cone of particles called a jet. Quarks cannot exist in free form due to QCD confinement and therefore fragment into hadrons to become jets that can be measured and studied to determine the properties of the original quark. Jets are significant in relativistic heavy ion physics as they provide insight into the QCD matter created in the collision and indicate its phase. When the QCD matter transitions into quark-gluon plasma, the energy loss in the medium grows significantly, which effectively suppresses the outgoing jet. When high-energy hadrons collide, one of four types of scattering reactions can occur: elastic, diffractive, soft-inelastic, and hard. Elastic collisions are interactions where the particles involved have the same type and energy both before and after the collision. During the collision of high-energy hadrons, diffractive processes may occur that involve the exchange of quantum numbers of the vacuum only. Inelastic diffractive processes are similar, except that one or both of the incident hadrons break apart. Soft-inelastic collisions also cause the breakup of the incident hadrons but at relatively low momentum transfers. These collisions are best described by exchanges of virtual hadrons and make up the largest part of the total cross-section. Hard collisions are particularly interesting as they involve direct interaction between partons within the hadrons (such as a proton or anti-proton). During these collisions, the incident hadrons break apart, and many new particles are created. The outgoing partons from the hard sub-process fragment into jets of particles. The remaining particles in the event are mostly soft particles that arise due to the breakup of the remnants of the incident hadrons and together form the underlying event. The hard-scattering component of the event consists of the outgoing two jets, including Initial State Radiation (ISR) and Final State Radiation (FSR). Hard probes are generated during the early stage of a collision in the primary, short-distance, partonic scattering with large virtuality (Q^2). Due to the uncertainty principle, their production occurs on temporal and spatial scales ($\Delta\tau \sim 1/Q$ and $\Delta r \sim 1/Q$), which are small enough to remain unaffected by the properties of the medium, i.e., the final-state effects. Therefore, they can directly probe the partonic phase of the reaction. Their production cross-section can be reliably calculated with perturbative QCD (pQCD) or via the Color Glass Condensate (CGC) framework, as the large virtuality allows for such calculations. Since QCD is asymptotically free, the running coupling constant can be used to calculate the strength of the interaction.

$$\alpha_S\left(Q^2\right) = \frac{1}{bL}\left(1 - \frac{b'}{b}\frac{\ln L}{L}\right) \qquad \text{where} \qquad L = \ln\frac{Q^2}{\Lambda^2}. \tag{50}$$

For large values of $Q^2 \gg \Lambda \simeq \Lambda^4_{QCD}$, the QCD running coupling constant becomes small, as a result of which the higher-order terms in an expansion of the cross-section in powers of α_S can be neglected. Hard collisions involve large momentum transfers, Q, and allow the probing of the hadron structure at short distances. Due to asymptotic freedom, the QCD running coupling constant becomes small at this scale (with $\alpha_S \leq 0.3$), making perturbative methods applicable. Consequently, measuring inclusive jet and dijet cross sections, as well as various other jet properties, can be used to test the predictions of pQCD, improve knowledge of α_S and Parton Distribution Functions at large x, and look for quark compositeness.

A.1.1 Jet Kinematics

In a colliding system, the interacting partons are typically not in the center-of-mass frame because the momentum fraction carried by each parton varies from event to event. As a result, the center-of-mass system of the partons is randomly boosted along the direction of the colliding hadrons. Longitudinally boost-invariant variables are used to conveniently describe jets in such a scenario:

$$\text{mass} \qquad m = \sqrt{E^2 - p_x^2 - p_y^2 - p_z^2}, \tag{51}$$

transverse momentum $p_T = \sqrt{p_x^2 + p_y^2}$, azimuthal angle $\phi = \arctan\left(p_y/p_x\right)$, rapidity $y =$

$\operatorname{arctanh}(p_z/E) = \frac{1}{2}\ln\left(\frac{E+p_z}{E-p_z}\right)$.

In the high energy limit, when $p \gg m$, the directly measured quantities conveniently are: energy (E) or transverse energy ($E_T = E\sin\theta \simeq p_T$), the azimuth ($\phi$) and the pseudo-rapidity

$$\eta = -\ln(\tan\theta/2) \tag{52}$$

$$\text{where the polar angle is given by } \theta = \arctan\left(p_T/p_z\right). \tag{53}$$

Bibliography

[1] D. Griffiths, “Introduction to elementary particles”, John Wiley & Sons, 49-52, 2008.

[2] F. Berman et al., “Application-level scheduling on distributed heterogeneous networks”, proceedings of supercomputing, 1996, https://doi.org/10.1145/369028.369109.

[3] Mesut Arslandok (for the ALICE Collaboration), “Event-by-Event identified particle ratio fluctuations in Pb-Pb collisions with ALICE using the identity method”, arXiv:1512.03372 [hep-ex].

[4] https://www.quantumdiaries.org/2014/03/14/the-standard-model-a-beautiful-but-flawed-theory.

[5] G. D’Agostini, “A multidimensional unfolding method based on Bayes’ theorem”, nuclear instruments and methods in Physics research A 362 (1995) 487-498 nuclear.

[6] J. Scott Moreland et al., “Alternative ansatz to wounded nucleon and binary collision scaling in high-energy nuclear collisions”, physical review C 92, 011901(R) (2015)

[7] R. Brun et al., “GEANT: Detector description and simulation tool”, CERN-W5013 (1994).

[8] Wang et al., “Hijing: A Monte Carlo model for multiple jet production in pp, pA, and AA collisions”, Phys. Rev. D 1991, 44, 3501.

[9] M. Gyulassy, In proceedings of eighth balaton conference on nuclear physics, edited by Z. Fodor (KFKI, Budapest, 1987); CERN Report No. CERN-TH-4794/87, 1987.

[10] ALICE Collaboration, “Definition of the ALICE coordinate system and basic rules for subdetector components numbering”, ALICE-INT-2003-038 (2003).

[11] S. R. Coleman et al., “High-energy tests of Lorentz invariance”, Phys. Rev. D59 (1999) 116008, arXiv:hep-ph/9812418 [hep-ph].

[12] C. Adler et al. [STAR Collaboration], Phys. Rev. Lett. 89, 202301 (2002) doi:10.1103/PhysRevLett.89.202301 [nucl-ex/0206011].

[13] B. I. Abelev et al. [STAR Collaboration], Phys. Rev. Lett. 98, 192301 (2007) Erratum: [Phys. Rev. Lett. 106, 159902 (2011)] doi:10.1103/PhysRevLett.106.159902, 10.1103/PhysRevLett.98.192301 [nucl-ex/0607012].

[14] G. Aad et al. [ATLAS Collaboration], Phys. Rev. Lett. 105, 252303 (2010) doi:10.1103/PhysRevLett.105.252303 [arXiv:1011.6182 [hep-ex]].

[15] K. H. Ackermann et al. [STAR Collaboration], Phys. Rev. Lett. 86, 402 (2001) doi:10.1103/PhysRevLett.86.402 [nucl-ex/0009011].

[16] K. Aamodt et al. [ALICE Collabora- tion], Phys. Rev. Lett. 105, 252302 (2010) doi:10.1103/PhysRevLett.105.252302 [arXiv:1011.3914 [nucl-ex]].

[17] J. Y. Ollitrault, Phys. Rev. D 46, 229 (1992) doi:10.1103/PhysRevD.46.229

[18] W. Broniowski et al., Phys. Rev. C 65, 024905 (2002) doi:10.1103/PhysRevC.65.024905 [nucl-th/0110020].

[19] B. B. Back et al. [PHOBOS Collaboration], Phys. Rev. Lett. 85, 3100 (2000) doi:10.1103/PhysRevLett.85.3100 [hep-ex/0007036].

[20] C. Adler et al. [STAR Collaboration], Phys. Rev. Lett. 87, 112303 (2001) doi:10.1103/PhysRevLett.87.112303 [nucl-ex/0106004].

[21] S. Adler et al. [PHENIX Collaboration], Phys. Rev. C 71, 034908 (2005) Erratum: [Phys. Rev. C 71, 049901 (2005)] doi:10.1103/PhysRevC.71.049901, 10.1103/Phys- RevC.71.034908 [nucl-ex/0409015].

[22] B. Abelev et al. [ALICE Collaboration], Phys. Rev. C 88, no. 4, 044909 (2013) doi:10.1103/PhysRevC.88.044909 [arXiv:1301.4361 [nucl-ex]].

[23] S. Chatrchyan et al. [CMS Collaboration], JHEP 1108, 141 (2011) doi:10.1007/JHEP08(2011)141 [arXiv:1107.4800 [nucl-ex]].

[24] G. Aad et al. [ATLAS Collaboration], Phys. Lett. B 707, 330 (2012) doi:10.1016/j.physletb.2011.12.056 [arXiv:1108.6018 [hep-ex]].

[25] M. Gyulassy et al., Phys. Rev. D 44, 3501 (1991) doi:10.1103/PhysRevD.44.3501

[26] M. L. Miller et al., Rev. Nucl. Part. Sci. 57, 205 (2007) doi:10.1146/annurev.nucl.57.090506.123020 [nucl- ex/0701025].

[27] L. Adamczyk et al. [STAR Collaboration], Phys. Rev. Lett. 115, no. 22, 222301 (2015).

[28] S. Chatrchyan et al. [CMS Collaboration], Phys. Lett. B 710, 256 (2012) doi:10.1016/j.physletb.2012.02.077 [arXiv:1201.3093 [nucl-ex]].

[29] M. L. Miller et al., "Glauber modeling in high energy nuclear collisions," Ann. Rev. Nucl. Part. Sci. 57, 205 (2007) [arXiv:nucl-ex/0701025].

[30] UA5 Collaboration, G. J. Alner et al., "Scaling of Pseudorapidity Distributions at c.m. Energies Up to 0.9-TeV", Z. Phys. C33 (1986) 1–6.

[31] F. Wilczek, "Quantum field theory", Rev. Mod. Phys. 71 (1999), arXiv:hep-th/9803075.

[32] C. Ratti, "Lattice QCD and heavy ion collisions: a review of recent progress", arXiv:1804.07810 [hep-lat].

[33] R. Hagedorn, "Statistical thermodynamics of strong interactions at high-energies", Nuovo Cim. Suppl., 3 (1965) 147–186.

[34] J. C. Collins et al., "Superdense matter: Neutrons or asymptotically free quarks?", Phys. Rev. Lett. 34 (1975) 1353.

[35] A STAR white paper, "Studying the Phase Diagram of QCD Matter at RHIC", 01 June 2014.

[36] M. C. Abreu, et al., “Observation of a threshold effect in the anomalous J/ψ suppression”, Phys. Lett. B45 (1999) 456-466.

[37] E. Andersen, et al., “Strangeness enhancement at mid-rapidity in Pb Pb collisions at 158-A-GeV/c”, Phys. Lett. B449 (1999) 401-406.

[38] K. Adcox, et al., “Suppression of hadrons with large transverse momentum in central Au+Au collisions at $\sqrt{sNN} = 130-GeV$ ”, Phys. Rev. Lett. 88 (2002) 022301, arXiv:0109003 [nucl-ex].

[39] K. H. Ackermann, et al., “Elliptic flow in Au + Au collisions at $\sqrt{sNN} = 130$GeV”, Phys.Rev. Lett. 86 (2001) 402-407, arXiv:0009011 [nucl-ex].

[40] B. B. Back et al., “The PHOBOS perspective on discoveries at RHIC”, Nucl. Phys. A757(2005) 28-101, arXiv:0410022 [nucl-ex].

[41] I. Arsene et al., “Quark gluon plasma and color glass condensate at RHIC”, arXiv:0410020 [nucl-ex].

[42] K. Adcox et al., “Formation of dense partonic matter in relativistic nucleus-nucleus collisions at RHIC: Experimental evaluation by the PHENIX collaboration”, Nucl. Phys. A757 (2005) 184-283, arXiv:0410003 [nucl-ex].

[43] ALICE Collaboration, “The ALICE experiment – A journey through QCD”, arXiv:2211.04384 [nucl-ex].

[44] Wilson, K., “Confinement of quarks”, Phys. Rev. D10 (1974) 2445-2459.

[45] C. Allton et al., “The QCD thermal phase transition in the presence of a small chemical potential”, Phys. Rev. D66 (2002) 074507, arXiv:0204010 [hep-lat].

[46] ALICE Collaboration, F. Carminati et al., “ALICE: Physics performance report, volume I, J.” ,Phys. G 30, 1517 (2004), doi:10.1088/0954-3899/30/11/001.

[47] ALICE Collaboration, B. Alessandro et al., “ALICE: Physics performance report, volume II, J.” , Phys. G 32, 1295 (2006), doi:10.1088/0954-3899/32/10/001.

[48] ALICE Collaboration, K. Aamodt, et al., “The ALICE experiment at the CERN LHC, JINST 3,”, S08002 (2008), doi:10.1088/1748-0221/3/08/S08002.

[49] https://home.cern/science/experiments/alice.

[50] https://cds.cern.ch/record/2789548/plots.

[51] E. V. Shuryak, Zh. Eksp. Teor. Fiz. 74 (1978) 408.

[52] Shuryak et al., “Structure of Strongly Coupled Quark-Gluon Plasma”, DOI: 10.1007/978-3-642-01539-7-19.

[53] S. Borsanyi et al., “QCD Crossover at Finite Chemical Potential from Lattice Simulations”, Phys. Rev. Lett. 125 no. 5, (2020), arXiv:2002.02821 [hep-lat].

[54] A. Andronic et al., “Hadron production in central nucleus-nucleus collisions at chemical freeze-out”, Nucl. Phys. A 772 (2006), arXiv:nucl-th/0511071.

[55] J. Cleymans et al., “Comparison of chemical freeze-out criteria in heavy-ion collisions”, Phys. Rev. C 73 (2006), arXiv:hep-ph/0511094.

[56] M. P losko´n, “Heavy-ion collisions - hot QCD in a lab”, Phys. Rev. C 73 (2006), arXiv:1808.01411v1, 2018.

[57] B. Muller et al., Annu. Rev. Nucl. Part. Sci. 62, 361 (2012).

[58] B. Schenke et al., Phys. Rev. Lett. 108, 252301 (2012).

[59] W. van der Schee et al., Phys. Rev. Lett. 111, 222302 (2013).

[60] https://twiki.cern.ch/twiki/bin/viewauth/ALICE/AnalysisTrains.

[61] Markus Zimmermann (for the ALICE Collaboration) 2015 J. Phys.: Conf. Ser. 608 012019.

[62] J. Y. Ollitrault, “Relativistic hydrodynamics for heavy-ion collisions”, Eur. J. Phys. 29, 275 (2008), doi:10.1088/0143-0807/29/2/010 [arXiv:0708.2433 [nucl-th]].

[63] ALICE Collaboration, “The ALICE experiment - A journey through QCD”, doi.org/10.48550/arXiv.2211.04384 [arXiv:2211.04384 [nucl-ex]].

[64] ALICE collaboration, “Performance of the ALICE Experiment at the CERN LHC”, Int. J. Mod. Phys. A 29 (2014) 1430044 [arXiv:1402.4476].

[65] ALICE Collaboration, K. Aamodt et al., The ALICE experiment at the CERN LHC, JINST, 3, S08002 (2008).

[66] ALICE Collaboration, K. Aamodt, et al., “The ALICE experiment as the CERN LHC”, JINST, 3, S08002 (2008).

[67] The ALICE collaboration, “Performance of the ALICE VZERO system”, JINST 8 P10016, 2013.

[68] G. P. Lepage, “Lattice QCD For Novices”, arXiv:0506036v1 [hep-lat], 2005.

[69] T. Preis et al., “GPU accelerated Monte Carlo simulation of the 2D and 3D Ising model”, Journal of Computational Physics, 228(12), 4468-4477 (2009).

[70] Szabolcs Borsanyi et al., “The QCD equation of state with dynamical quarks”, JHEP 1011:077,2010, arXiv:1007.2580 [hep-lat].

[71] F. Gardim et al., “Measuring the speed of sound of the quark-gluon plasma in ultra central nucleus-nucleus collisions”, arXiv:1909.11609v1 [nucl-th] 25 Sep 2019.

[72] S. Das et al., “Relating centrality to impact parameter in nucleus-nucleus collisions”, arXiv:1708.00081v2 [nucl-th] 22 Jan 2018.

[73] F. Gardim et al., “Thermodynamics of hot strong-interaction matter from ultrarelativistic nuclear collisions”, Nature Physics 16, 615-619 (2020) [https://doi.org/10.1038/s41567-020-0846-4]

[74] ALICE Collaboration, “Transverse momentum spectra and nuclear modification factors of charged particles in Xe-Xe collisions at $\sqrt{s_{\rm NN}} = 5.44$TeV”, arXiv:1805.04399

[75] ALICE Collaboration, C. Zampolli, “Particle identification with the ALICE detector at the LHC”, in Proceedings, PLHC2012: Physics at the LHC 2012 (PLHC2012): Vancouver, BC, Canada, June 4-9, 2012. 2012. arXiv:1209.5637 [hep-ex].

[76] ALICE Collaboration, B Abelev et al., “Technical design report for the upgrade of the ALICE Inner Tracking System (ITS)”, 2014 J. Phys. G: Nucl. Part. Phys. 41 087002.

[77] ALICE Collaboration, “Analysis Note: Charged-particle production as a function of multiplicity in the transverse region for $pp, p-Pb$ and $Pb-Pb$ collisions at $\sqrt{s_{\rm NN}} = 5.02$TeV”, URL: https://alice-notes.web.cern.ch/node/1031.

[78] ALICE Collaboration, “Analysis Note: System size and energy dependence of multiplicity-dependent charged-particle transverse-momentum spectra”, URL: https://alice-notes.web.cern.ch/node/896.

[79] R. Brun et al., “GEANT: Detector description and simulation tool”, CERN-W5013 (1994).

[80] ALICE Collaboration, J. Adam et al., “Enhanced production of multi-strange hadrons in high-multiplicity proton-proton collisions”, Nature Phys. 13 (2017) 535–539, arXiv:1606.07424 [nucl-ex].

[81] ALICE Collaboration, S. Acharya, et al., “Multiplicity dependence of (multi-)strange hadron production in proton-proton collisions at $\sqrt{s} = 13$TeV’”, Eur. Phys. J. C 80 (2020) 167, arXiv: 1908.01861 [nucl-ex].

[82] ALICE Collaboration, S. Acharya, et al., “Transverse momentum spectra and nuclear modification factors of charged particles in Xe-Xe collisions at $\sqrt{s_{\rm NN}} = 5.44$TeV”, Phys. Lett. B788 (2019) $166 - 179$, arXiv: 1805.04399 [nucl-ex].

[83] https://twiki.cern.ch/twiki/bin/viewauth/ALICE/AliDPGtoolsPileup

[84] W. Broniowski et al., Phys. Rev. C 65, 024905 (2002) doi:10.1103/PhysRevC.65.024905 [nucl-th/0110020].

[85] S. Bethke et al., “Quantum Chromodynamics (QC)”, (particle data group), Chin. Phys. C38 (2014) 090001.

[86] A. Bazavov, et al., “Equation of state in (2+1)-flavor QCD”, Phys. Rev. D90 (2014) 094503, arXiv:1407.6387 [hep-lat].

[87] ALICE Collaboration ,arXiv:1402.4476v4 [nucl-ex] 12 Aug 2015.